Development of a reduced order electrochemical and thermal model for Lithium battery with blended cathode

by

Xueyan Li

A dissertation submitted to the Graduate Faculty of
Auburn University
in partial fulfillment of the
requirements for the Degree of
Doctor of Philosophy

Auburn, Alabama
Dec.13 , 2014

Key words: Lithium battery, NMC, LFP, blended cathode, full order model, model order reduction, model validation

Approved by

Song-Yul Choe, Chair, Professor of Mechanical Engineering
Jeffrey Fergus, Professor of Materials Engineering
Roy Knight, Professor of Mechanical Engineering
Amnon Meir, Professor of Mathematics

Abstract

Accurate and fast estimation of state of charge (SOC) and state of health (SOH) during operations plays a pivotal role in prevention of overcharge or undercharge and accurately monitoring the state of cell degradation, which requires a model that can be embedded in the battery management system (BMS). Currently available models are based on either empirical equations or electric equivalent circuit components with voltage sources or a combination of the two. The models are relatively simple, but limited to represent a narrow range of operating behaviors not including the effects of temperature, SOC and degradation. On the other hand, Full Order Models (FOM) are multi-dimensional or multi-scale models based on electrochemical and thermal principles capable of representing the details of cell behavior, but impractical for real time applications, because they require high computational time. Therefore, there is a need for the development of a model with an intermediate performance and real time capability, which is accomplished by reducing the FOM into a Reduced Order Model (ROM).

Two FOMs are developed for $LiMn_xCo_yNi_zO_2$ (NMC)/Carbon batteries and $LiFePO_4$ (LFP)/Carbon batteries separately. After that, the two FOMs are coupled to simulate the behavior of NMC/LFP blended cathode batteries. The reduction of the models is carried out in three parts: the ion concentration in the electrode is reduced using the polynomial approach, the ion concentration in the electrolyte is reduced using the state space method, and potentials and electrochemical kinetics are reduced by linearization. In addition, the energy equation is used to calculate the cell temperature, on which the diffusion coefficient and the Solid Electrolyte Interphase (SEI) resistance are dependent. The computational time step is determined based on the

total computational time and errors at a given SOC range and different current rates. ROM responses are compared with those of the FOM and experimental data at a single cycle and multiple cycles under different operating conditions. The results show that calculation time of the ROM is reduced to approximately one fifteenth of the FOM, while the accuracy can be maintained.

The working mechanism of the cells with blended cathode of NMC and LFP is very complex and hard to understand. In addition, characteristics of the blended cells, particularly the plateau, history and path dependence of LFP materials, make it extremely difficult to estimate the SOC and SOH using classical electric equivalent circuit models. Therefore, a reduced order model based on electrochemical and thermal principles is developed with objectives for real time applications and validated against experimental data collected from a large format pouch type of lithium ion polymer battery. The model for LFP is based on a shrinking core model along with moving boundary and then integrated into NMC model. Responses of the model that include terminal voltage and temperature are compared with those of experiments at CC/CV charging and CC discharging at various operating conditions. In addition, the model is used to analyze effects of mass ratios between two materials on terminal voltage and heat generation rate; and the model is used to estimate the SOC based on Extended Kalman filter.

Acknowledgments

I would like to express my appreciation to my advisor, Dr. Song-Yul Choe, for offering me the research opportunity. With his valuable suggestions and detailed assistance in writing, I can finish all the reports and papers. I would also like to acknowledge committee members Dr. Jeffrey W. Fergus, Dr. Roy W. Knight, and Dr. Amnon J. Meri for their encouragement and insightful comments.

Sincere thanks to my colleagues Kyle D. Malinowski, Meng Xiao, Rujian Fu, Yinyin Zhao, and Victor Agubra for the stimulating discussion. Additional thanks to Kyle Malinowski for discussion in experimental work and Meng Xiao for discussion in modeling.

I would also like to thank my parents, younger brother, and my parents in law. They are always supporting me and encouraging me.

Finally, I dedicate this Ph.D. thesis to my baby, Evelyn Cao. I appreciate your patience and accompany during mommy's Ph.D. study. I would like to thank my husband, Nan Cao, who is always there with me through the good times and the bad.

Table of contents

List of Tables

List of Figures

List of Symbols

A	sandwich area of the cell (cm^2)
a_s	specific surface area of electrode (cm^{-1})
c	ion concentration in solid phase (mol L^{-1})
C_p	heat capacity (J kg^{-1} K^{-1})
D	diffusion coefficient in electrode (cm^2 s^{-1})
d	cell thickness (cm)
E_a	activation energy (kJ·mol^{-1})
F	Faraday constant (96,487 C mol^{-1})
h	convective heat transfer coefficient (W K^{-1})
I	current of the cell (A)
i	current density (A cm^{-2})
i_0	exchange current density of intercalation (A cm^{-2})
j^{Li}	reaction rate of intercalation (A cm^{-3})
L	thickness of the micro cell (cm)
m	mass of a single cell (kg)
OCV	open circuit voltage (V)
Q	capacity of the cell (A h)
Q_{gen}	heat generation rate (W cm^{-3})

Q_{max}	maximum capacity of the cell (A h)
q_{ave}	volume-averaged concentration flux (mol cm^{-4})
q_{rev}	reversible heat generation rate (W cm^{-3})
q_{irr}	irreversible heat generation rate (W cm^{-3})
q_{convec}	heat convection rate (W cm^{-3})
R	resistance (Ω cm^2) or universal gas constant (8.3143 J mol^{-1} K^{-1})
R_s	radius of spherical electrode particle (cm)
r	coordinate along the radius of electrode particle (cm) or location of the interface between α and β phase in LFP particles
SOC	state of charge
T	cell temperature (K)
T_{amb}	ambient temperature (K)
t	time (s)
t^0_+	transference number
U_{equ}	equilibrium potential (V)
U_{eq}^{Θ}	standard equilibrium potential when $c_e = c_{e0}$ (V)
V	voltage (V) or volume of the composite electrode (cm^3)
V_t	terminal voltage of cell (V)
w	weighting factor

x	stoichiometric number of the electrode or coordinate along the thickness of micro cell
Z	impedance (Ω)

Greek symbols

α	transfer coefficient of reaction
δ	thickness (mm)
ε	volume fraction
ϕ	electrical potential (V)
η	overpotential (V)
κ	ionic conductivity (S cm^{-1})
λ	eigenvalue
κ_D	concentration driven diffusion conductivity (A cm^{-1})
ρ	density (g cm^{-3})
σ	conductivity (S cm^{-1})

Subscripts

ave	average
cell	single cell
e	electrolyte phase

max	maximum
n	negative electrode (anode)
p	positive electrode (cathode)
r	radial direction in electrode particle
SEI	solid electrolyte interphase
s	solid phase (active material)
sep	separator
surf	Surface of electrode particle
t	terminal
α	α phase
β	β phase
0%	0% state of charge
100%	100% state of charge
-	negative electrode (anode)
+	positive electrode (cathode)

Superscripts

eff	effective
Li	lithium ion

List of Abbreviation

BMS	Battery Management System
DOD	depth of discharge
ECM	equivalent circuit model
EIS	electrochemical impedance spectroscopy
ETM	electrochemical thermal model
FOM	full order model
LCO	$LiCO_2$
LFP	$LiFePO_4$
LiPB	lithium ion polymer battery
LMO	$LiMn_2O_4$
NCA	$LiNi_xCo_yAl_{1-x-y}O_2$
NMC	$LiNi_xMn_yCo_{1-x-y}O_2$
OCV	open circuit voltage
ODE	ordinary differential equation
PDE	partial differential equation
ROM	reduced order model
SEI	solid electrolyte interphase
SEM	scanning electron microscopy

SOC	state of charge
XPS	X-ray photoelectron spectroscopy
XRD	X-ray Diffraction

Chapter 1 Introduction

1.1 Background

The energy efficiency of future power systems used in grids or in transportations can be substantially improved by storing excess energy and retrieving the energy that would otherwise be dissipated. Particularly, batteries are preferable for use in energy storage because of their high efficiency during charging and discharging processes as well as their high power and energy density. Among different battery technologies, the Li-polymer battery is the most preferred technology for consumer electronics because of its high power density. In order to produce cells for high power applications, active areas for the cells are increased and packaged in a form that can be easily integrated in a vehicle. Depending on the method of packaging, the cells can have a cylindrical, prismatic, or pouch shape. Because of the high current rate and the packaging density, the heat generation rate becomes high, which induces fast cell degradation. Among these different packaging methods, the pouch type is widely employed because of its low manufacturing costs and relatively high heat transfer capability.

Most of the batteries use graphite as anode material, so the biggest factor affecting battery performance is the cathode material. The research into cathode material has become more popular recently, and its development has been well summarized in [1-4]. Commonly adopted cathode materials are summarized as below.

1.1.1 Cathode materials

Conversion efficiency of future power systems used in grids or transportation systems can be substantially improved by storing excess energy and retrieving it that would otherwise be dissipated. Particularly, batteries are preferred as energy storage because of their high efficiency during charging and discharging processes as well as their high power and energy density compared to other alternative storage technologies. Among different battery technologies, the Lithium ion polymer battery (LiPB) is the most preferred technology simply because of its high power density and the high number of cells that are currently being produced for consumer electronics. The same chemistries for electrodes and minimally modified electrolytes can still be used to design cells for high power applications. However, the packaging can be differently. Depending on the method of packaging, batteries can have a cylindrical, prismatic, or pouch shape. Since the current rates are relative high in the applications, heat generated in the cells becomes high, too, which accelerates side reactions and degradations. As a result, a structural design is required, which includes a relatively high heat transfer capability in addition to massive manufacturability. Therefore, the large format pouch cells are widely used for these high power applications.

Anodic materials used for those cells are basically carbon graphite, while different cathode materials are chosen to meet performances of the cells, including a blended chemistry [5]. Several basic cathode materials with extra additives have been made to design either high power or energy cells with safe functionalities and long cycle life considering low manufacturing costs. The major materials with structures are as follows; $LiFePO_4$ (LFP) with one dimensional olivine structure, $LiCO_2$ (LCO), $LiNi_xMn_yCo_{1-x-y}O_2$ (NMC), and $LiNi_xCo_yAl_{1-x-y}O_2$ (NCA) with two dimensional layered structure, and $LiMn_2O_4$ (LMO) with three dimensional spinel structure.

Advantages of the LFP are electrochemical and thermal stability compared to others, therefore the safety can be improved. In addition to a long cycle life, a high discharging/charging rate capability employing nanoparticles can be accomplished. However, the materials show a relatively low capacity (160Ah/kg) along with a low standard voltage of 3.4V vs. Li in addition to the voltage plateau caused by two-phase transition during lithiation and delithiation in LFP particles [6].

The other materials, LCO, NMC, and NCA with 2D layered structures have a high capacity and a high standard voltage, but do not show electrochemical and thermal stability in operations. LCO shows the lowest thermal stability, especially when overcharged with a voltage that is larger than 4.2V. Other components like Al and Mn in NCA and NMC can chemically stabilize the cathode, but problems in cycle life and safety still remain incompletely solved [7, 8].

Conversely, LMO with 3D spinel structure is promising with technical advantages of high voltage, high power, good safety, and low cost. However, the manganese can be dissolved in electrolytes, which reduces cycle life and deteriorates safety, and the dissolution is accelerated by elevated temperature. In addition, the capacity and energy density are relatively low and their typical values are about 100-120 Ah/kg and 380 Wh/kg, respectively [5].

Analysis above shows that there is no single chemistry for cathode that provides all of requirements for electric vehicle applications. Blending different chemistries is a potential solution for designers to get around drawbacks and maximize the advantages, as summarized in Figure 1.

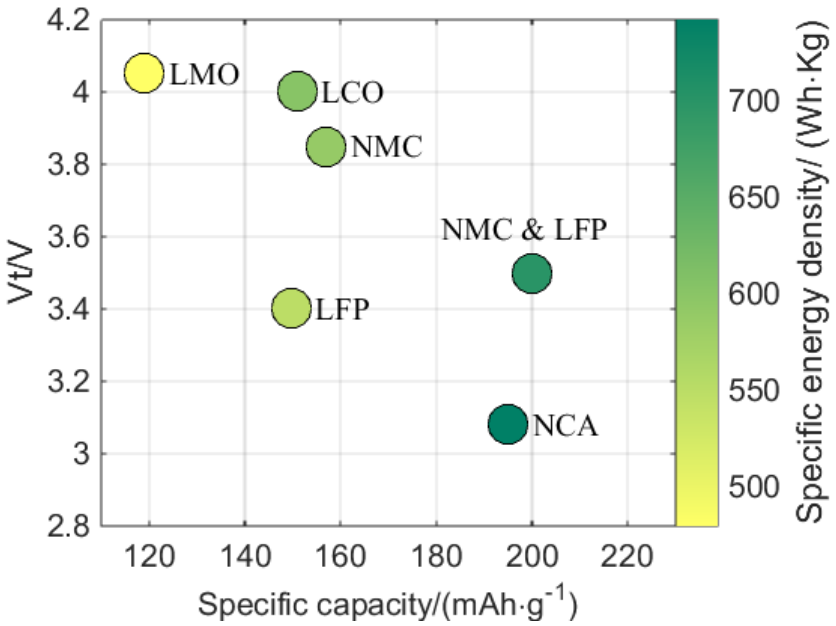

Figure 1. Performance of cathode materials.

1.1.2 Blended cathode

Cathode materials of batteries applied for xEVs should ideally facilitate high capacity, power, energy, rate capability along with good safety, long cycle life at low costs. However none of the single cathode materials can meet all of the requirements above as discussed previously. Blended cathode materials can complement each other and achieve better performance than a single parent cathode material.

As a matter of fact, LMO is one of favorite cathode materials that can provide high power and rate capability along with increased safety. The demerits of the materials can be improved by blending them with the materials capable of providing high capacity or stabilizing them by preventing from Mn dissolutions. A blended cathode material made of LMO and NCAshows improved performances in increased discharge capacity and reduced heat generation in addition to decreased Mn dissolution. An optimal ratio of NCA for the best performance is 33.3% [9]. In

addition, different ratios of LMO and NCA can also achieve improved performances in rate capability, and combined power and energy [10]. Other study shows that blending the LMO with $LiNi_{0.8}Co_{0.2}O_2$ can decrease capacity fade of LMO because of reduced dissolution of Mn into the electrolyte, even at elevated temperatures [11]. The optimal ratio for $LiNi_{0.8}Co_{0.2}O_2$ that completely prevents the dissolution was 15wt%. Structure of cathode materials has been investigated to suppress Mn dissolution and to retain the capacity. The layered oxide cathode such as LCO turned out to be the best performing structure [12]. Contribution of different materials to the cell capacity and structural changes of the mixed LMO and NMC are also investigated using *in situ* X-ray Diffraction (XRD). Based on results for structure changes of each materials during operations, optimal ratio of materials is suggested, which improves the cell capacity [13].

On the other hand, LCO is widely employed as cathode materials for batteries used for portable electronic devices because of high capacity and energy density along with long cycle life. However, poor thermal stability of LCO has raised concerns about safety, especially when being overcharged. This thermal stability can be improved by blending LCO with NMC, whose surfaces are coated with AlF_3. The modified blended cells show not only improved thermal stability, but also high discharge capacity along with good capacity retention rate [14]. Olivine-structured LFP has been used as an additive for cathode, which also improves the thermal stability of LCO. The LCO/LFP/Al double-layered cathode showed the best tolerance against overcharging and improved safety compared to that of LCO [15].

In addition to the requirements for increasing capacity and power density along with high safety, the high rate capability is also an important criteria, which can be achieved using LFP material. LFP as a cathode material has shown a high stability in electrochemical and thermal aspects and a high rate capability, but a low standard potential against Li electrode that is pretty

flat around 3.4V. These drawbacks can be improved by blending it with other materials that have a layered oxide structure.

Two different cathode materials made of LFP/NMC and LFP/LCO are compared each other. The first one has shown superior performance in cycling with high current rates, while the others with layered configuration has shown better in rate capacity because of LCO performance in both good rate capability and high energy density [16]. A different configuration for two materials is proposed, that is made of NMC as the core coated with LFP [17]. The NMC has a high capacity and energy density, but a poor cycle retention at elevated temperature, while LFP has a low energy density but a high thermal stability. The results have shown that the coating using LFP significantly improves cycling performance of NMC at high temperatures without a large initial capacity drop in the first cycle. Furthermore, a blended cathode composed of $xLi_2MnO_3 \cdot (1-x)LiNi_{0.44}Mn_{0.31}Co_{0.25}O_2$ (ANL-NMC, with x=0.5) and LFP is proposed [18], which has increased both energy density and power capability over the entire SOC window because of the low impedance of LFP at low SOC range.

The blended cathodes is a very attractive combination of material that can be used to achieve a better performance than the parent cathode material, with respect to certain operation requirements.

1.2 Motivation and objectives

When a cell is charged or discharged, ions are transported from the cathode electrode through the electrolyte and the separator to the anode and vice versa, while electrons flow through the wires that connect a load to the terminal. Oxidation and reduction processes and charge transport in the cell produce heat that elevates the cell temperature. Safe and reliable operation of cells requires a BMS that protects the cells by controlling charging and discharging currents, based on the SOC,

SOH and heat flux using a coolant flow. The BMS needs a computational model that is capable of being run in real time and used to estimate the state variables of the cells more accurately, so that the cells can be controlled for operation within a safe range.

It is crucial to develop a mathematical model for the lithium ion polymer battery with blended cathode consisting of NMC and LFP. The model is built based on electrochemical and thermal principles, including charge conservation, mass transport, ion diffusion, and heat transfer. Given initial conditions and load profile, the performance of the battery could be simulated with the model. However, since the structure and the ion diffusion mechanisms in NMC and LFP particles are different, two submodels are designed separately for each single cathode cell, and then those two submodels will be combined with each other to simulate the performance of the battery with the blended cathode of NMC and LFP. The blended model takes into account characteristics of each active material, and the interactions between different materials, caused by contact resistance and particle size.

The blended model can be implemented in the BMS to calculate the state of the batteries, such as terminal voltage, SOC, ion concentration, and heat generation; however, the FOM is time consuming to be implemented in the BMS. The reduction of the model is carried out for ion concentrations in both the electrode and the electrolyte, as well as for potentials and kinetics. The reduction of the ion concentration in the electrode is accomplished using the polynomial approach, that of the ion concentration in the electrolyte is done using the state space method, and the reduction of potentials and electrochemical kinetics is carried out by linearization. In addition, the energy equation is used to calculate the cell temperature, on which the diffusion coefficient and the Solid Electrolyte Interphase (SEI) resistance are dependent. The results show that the

calculation time of the ROM is reduced to approximately one fifteenth of the FOM, while the accuracy can be maintained.

1.3 Structure

The basic structure of the dissertation is shown as follows:

1. Introduction.

   This section involves research background, motivations, and objectives.

2. Submodel for cells with NMC cathode

   The electrochemical principles and order reduction methods for NMC cells are introduced in this section. The terminal voltage and SOC of NMC cell during charging/discharging is simulated.

3. Submodel for cells with LFP cathode

   The two-phase transition mechanism and order reduction methods for LFP cells are introduced in this section. The phase change, terminal voltage and SOC of LFP cell during charging/discharging are simulated.

4. Model for cells with blended cathode of NMC and LFP

   This section describes the principles of combination of the NMC and LFP submodel to develop a model for cell with blended cathode. The optimization of parameters of the ROM for a cell with blended cathode will be introduced in this section, based on comparison between model simulation and experiment results at different current rates and different temperatures.

5. Conclusion

Chapter 2 Modeling for NMC

2.1 Review of model with NMC cathode

Review of recent publications shows that the computational models can be classified into two categories, the electrochemical thermal models (ETM) [19], [20], based on electrochemical thermal principles, and the electric equivalent circuit model (ECM) [21], constructed using a voltage source and electric circuit components.

ETM is derived from physical law that includes electrochemical kinetics, mass, charge and energy balance along with potential theory that has a form of coupled partial differential equations (PDEs) [22] [23]. With a finite difference method, the coupled PDEs can be discretized and replaced by ordinary differential equations (ODEs) that can be numerically solved. During the discretization in space and time domain, the discretization steps should be small enough to ensure numerical stability and minimal calculation errors, which results in a high order of the matrices and consequently takes a long computational time. Therefore, the ETM is inappropriate for real time applications. Since the computational time for calculation of the ETM is mostly consumed by solving diffusion process of ions in the solid particles, there have been several attempts by substituting all particles in electrodes with a single particle [24] or reducing the order of the diffusion equation in the particle mathematically [23].

A reduced model for a cell proposed by R. Klein et al. employs the partial differential algebraic equations (PDAE) for electrodes under assumptions that lithium ion concentrations in the

electrolyte are uniformly distributed, and that the mass transfer in the solid only takes place in the radial direction [25]. In addition, ion transport is described using three variables, a volume averaged concentration in the solid particles, a concentration at the surface, and an averaged concentration flux. The model poorly predicts the cell behavior at high current rates where high heat generation is experiencing because of the assumption of constant temperature averaged concentration. V. Subramanian et al. proposed a polynomial approximation for ion concentration in solid electrodes that considers porosity of the electrodes under the assumptions that the temperature, and the diffusion and kinetic parameters are constant [26]. This approach allows for replacement of the original nonlinear partial differential equations with series of ordinary differential equations, so that the calculation time for ion concentrations can be reduced.

C. Speltino et al. proposed two different models for a cell, average model for electrodes (EAM) and state values model (SVM). The former assumes a constant concentration in the electrolyte, while no gradient of ion concentration is present in the electrodes and the spatial dependence of the current governed by the Butler-Volmer equation is negligible. The latter divides all governing equations into submodels in order to derive an analytical transfer function. The EAM shows accurate SOC estimation but is highly sensitive to nonlinearity of model parameters which leads to errors in voltage estimation. The SVM is relatively easy to obtain because of its linear structure, but provides inaccurate SOC estimation during abrupt transients [27].

On the other hand, there have been efforts for improvement of the ECM using OCV [28] and minimization of the errors by employing feedback loops like the Kalman filter [29], linear observer [30], sliding-mode observer [31], fuzzy logic [32], artificial neural network [33] and so on. The results show increased accuracy in prediction of terminal voltages and SOC.

However, all of the models mentioned above have not taken into account the effects of SOC variation as a function of stoichiometry number and temperature on the terminal voltage. In addition, the temperature changes in a cell are not predicted. The temperature effects are investigated by Pals [34] and Guo [35]. However, the heat source terms in the energy equation do not consider the heat generation caused by a gradient of ion concentrations in the electrodes. In fact, there is an internal ionic current flow driven by the gradient of ions that causes extra heat even though the current is interrupted. In addition, effect of the temperature on diffusions of ions is not considered.

We propose a ROM based on electrochemical and thermal principles. Analysis of the first ROM is published [36], which assumed that the cell temperature is constant. In this paper, heat generation using the energy equation and effects of temperature are considered where diffusion coefficient and resistance of the SEI are temperature dependent and approximated using empirical equations derived from experimental data. In order to assess the performance of the model, simulation results of the ROM are compared with those of FOM and the experimental data. The experimental data is collected from a test station, where the ROM is implemented using LabVIEW. A single and a multiple load cycle are applied to exam validity of the model.

2.2 Full order modeling of NMC cells

A FOM for a pouch type Li-polymer single cell is a quasi-three dimensional model developed based on electrochemical thermal principles, as shown in Figure 2. The FOM of the single cell is assumed to be made of microcells that are connected in parallel by current collectors at both electrodes. Lithium concentrations in the electrodes and electrolyte, potentials in the electrodes and electrolyte, and overpotential within the solid electrolyte interphase are calculated from the microcell model, while the temperature is calculated from the single cell model. Because of the

high conductivity of the current collectors, we assumed that there is no lateral current flow from one microcell to another, so that all lateral effects are ignored. In addition, the current collectors in each layer have the same potential, so only two current collectors are considered for the model. The terminal tab current of the two collectors in the model are obtained by dividing total tab current by the number of layers.

Chemical reactions take place at the surface of electrode particles that contact with the electrolyte. After the chemical reaction has occurred, the free ions in the electrodes diffuse until having fully intercalated. This mechanism is approximated with a sphere, where ions diffuse only in the radial direction driven by the gradient of ion concentration.

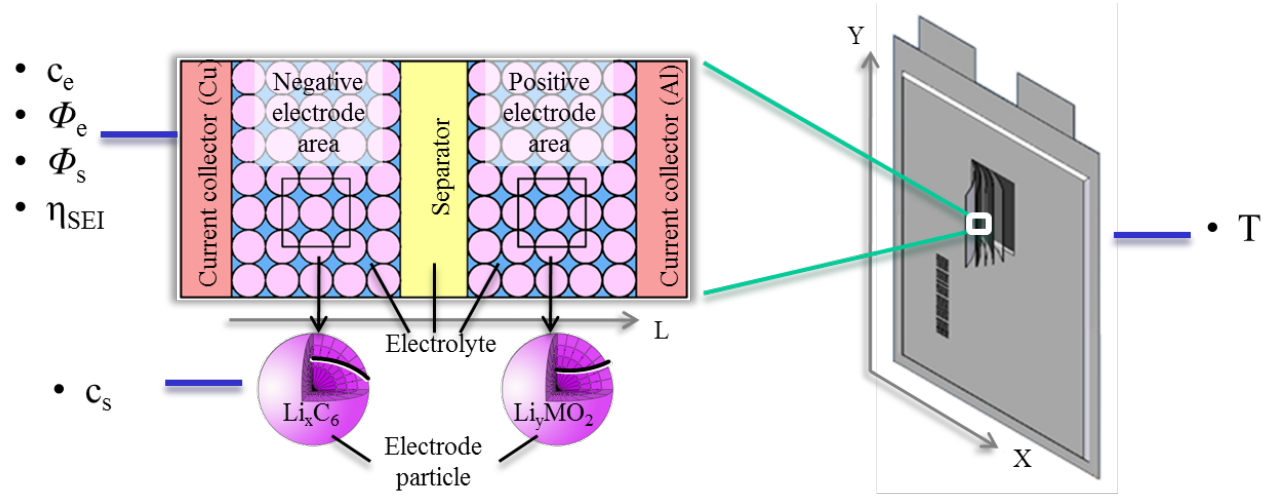

Figure 2. Model set-up for a pouch type cell and a micro cell [19].

A schematic diagram for modeling of a single cell is shown in Figure 3, where initial conditions, input variables and parameters for the model, and outputs are included. The input variables and initial operating conditions are current, voltage, and ambient temperature as a function of time. The output variables are dynamic responses of the loads, including terminal voltage, current, SOC, temperature distributions, lithium concentrations, potentials, and current densities. In addition, the

diagram shows how governing equations of the microcells are interconnected to form a model for the single cell.

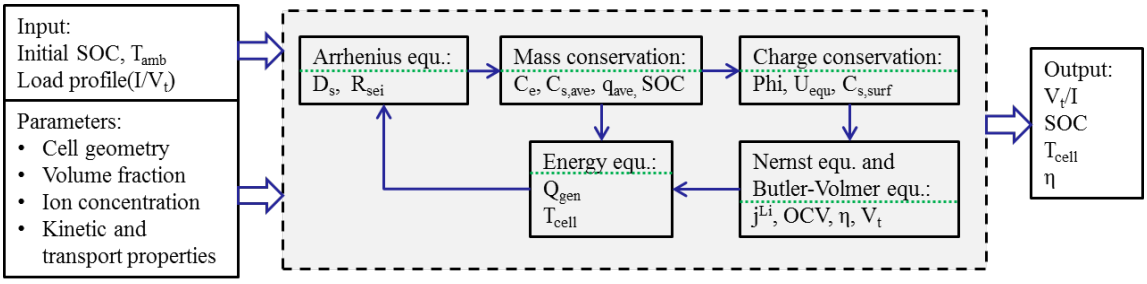

Figure 3. Scheme of the model for a single cell.

2.2.1 Ion concentration in electrodes

A model for electrodes is based on the porous electrode theory, where lithium-ion concentration, c_s, in single spherical particle is described by the Fick's law of diffusion,

$$\frac{\partial c_s}{\partial t} = \frac{D_s}{r^2}\frac{\partial}{\partial r}\left(r^2 \frac{\partial c_s}{\partial r}\right), \tag{1}$$

with boundary conditions,

$$\frac{1}{r}\frac{\partial c_s}{\partial r}\Big|_{r=0} = 0 \text{ and } D_s \frac{\partial c_s}{\partial r}\Big|_{r=R_s} = \frac{-j^{Li}}{a_s F}, \tag{2}$$

where r is the radial coordinate of an electrode particle, R_s is the radius of electrode particles, and F is the Faraday's constant, ε_s is the active material volume fraction, D_s is the solid phase diffusion coefficient that is dependent upon temperature , j^{Li} is the current density, a_s is the interfacial surface area calculated from $3\,\varepsilon_s/R_s$.

2.2.2 Ion concentration in electrolyte

Distribution of ion concentrations in electrolyte and its boundary conditions can be described as,

$$\frac{\partial(\varepsilon_e c_e)}{\partial t} = \frac{\partial}{\partial x}\left(D_e^{eff}\frac{\partial}{\partial x}c_e\right) + \frac{1-t_+^0}{F}j^{Li}$$
$$\frac{\partial c_e}{\partial x}\Big|_{x=0} = \frac{\partial c_e}{\partial x}\Big|_{x=L} = 0 \quad , \tag{3}$$

where c_e is the lithium-ion concentration in electrolyte phase, ε_e is the electrolyte phase volume fraction, t^0_+ is the transference number, D_e^{eff} is the effective diffusion coefficient accounting for tortuosity by correcting diffusion coefficient with electrolyte phase volume fraction ε_e and Bruggeman's exponent, as shown in the following equation,

$$D_e^{eff} = D_e \cdot \varepsilon_e^p \quad . \tag{4}$$

2.2.3 Potentials in both electrodes and electrolyte

The potential in the electrodes, ϕs, is derived from the Ohm's law,

$$\frac{\partial}{\partial x}\left(\sigma^{eff}\frac{\partial}{\partial x}\phi_s\right) - j^{Li} = 0 \quad , \tag{5}$$

with boundary conditions,

$$-\sigma^{eff}\frac{\partial}{\partial x}\phi_s\Big|_{x=0} = -\sigma^{eff}\frac{\partial}{\partial x}\phi_s\Big|_{x=L} = \frac{I}{A}$$
$$\frac{\partial}{\partial x}\phi_s\Big|_{x=L_-} = \frac{\partial}{\partial x}\phi_s\Big|_{x=L_-+L_{sep}} = 0 \quad , \tag{6}$$

where L is the thickness of the cell, L- is the thickness of the negative electrode, Lsep is the thickness of the separator, A is the plate area of electrode, and σ^{eff} is the effective solid phase conductivity that is obtained from the conductivity σ multiplied with active material fraction ε_s, as shown in the following equation,

$$\sigma^{eff} = \sigma \cdot \varepsilon_s \quad . \tag{7}$$

The potential in electrolyte is derived from the charge conservation law,

$$\frac{\partial}{\partial x}\left(\kappa^{\text{eff}}\frac{\partial}{\partial x}\phi_{\text{e}}\right)+\frac{\partial}{\partial x}\left(\kappa_{\text{D}}^{\text{eff}}\frac{\partial}{\partial x}\ln c_{\text{e}}\right)+j^{\text{Li}}=0$$
$$\left.\frac{\partial}{\partial x}\phi_{\text{e}}\right|_{x=0}=\left.\frac{\partial}{\partial x}\phi_{\text{e}}\right|_{x=L}=0 \quad . \tag{8}$$

Similar to the diffusion coefficient, ionic conductivity, κ^{eff}, is obtained from electrolyte phase volume fraction ε_{e} and Bruggeman's exponent p, as shown in the following equation,

$$\kappa^{\text{eff}}=\kappa\cdot\varepsilon_{\text{e}}^{p} \quad . \tag{9}$$

Current density is obtained from the Butler-Volmer electrochemical kinetic equation,

$$j^{\text{Li}}=a_{\text{s}}i_0\left\{\exp\left[\frac{\alpha_{\text{a}}F}{RT}(\eta-\eta_{\text{SEI}})\right]-\exp\left[-\frac{\alpha_{\text{c}}F}{RT}(\eta-\eta_{\text{SEI}})\right]\right\} \quad , \tag{10}$$

where i_0 is the exchange current density, α_{a} and α_{c} are the anodic and cathodic charge transfer coefficient, R is the universal gas constant, T is the temperature, and η is the overpotential defined as the potential difference between the solid, electrolyte and the equilibrium. The SEI on anode side is approximated with a resistor, R_{SEI}, that causes an additional overpotential η_{SEI}, as shown below,

$$\eta=\phi_{\text{s}}-\phi_{\text{e}}-U$$
$$\eta_{\text{SEI}}=\frac{j^{\text{Li}}R_{\text{SEI}}}{a_{\text{s}}} \quad . \tag{11}$$

The equilibrium potential is the difference between the potential of positive electrode and negative electrode of a battery. It can also be called open circuit voltage of a battery, since it can be measured as the terminal voltage of the battery when there is no current flowing and the battery reaches equilibrium state. In this paper the equilibrium potential of the negative electrode is calculated with empirical function of ion concentration as shown in (12); and the equilibrium

potential of the positive electrode is set as the difference between measured OCV and the equilibrium potential of the negative electrode.

$$\begin{aligned} &U_{\_}(x) = 8.00229 + 5.0647x - 12.578x^{1/2} - 8.6322*10^{-4}x^{-1} + 2.1765*10^{-5}x^{3/2} \\ &- 0.46016*\exp(15(0.06 - x)) - 0.55364*\exp(-2.4326(x - 0.92)) \\ &x = c^{-}_{s,surf} / c^{-}_{s,\max} \end{aligned} \tag{12}$$

2.2.4 Temperature effects

Temperature of the cell is described using the energy equation under isothermal condition,

$$\rho C_{\mathrm{p}} \frac{dT}{dt} = Q_{\mathrm{gen}} - q \,. \tag{13}$$

where ρ and C_{p} are the density and heat capacity, Q_{gen} is the heat generation rate per unit volume in a cell during charging/discharging and q is the heat transfer rate per unit volume between the cell and its surroundings expressed as,

$$q = \frac{h}{d}(T - T_{\mathrm{amb}}) \,, \tag{14}$$

where h, d, and T_{amb} are the heat transfer coefficient, cell thickness, and ambient temperature, respectively.

In general, the heat generation is expressed as a sum of irreversible and reversible heat generation term. The irreversible heat source term at a given current is determined by the difference between the terminal voltage and OCV, while the reversible heat source term is the change of entropy at a given temperature that is the same as the change of OCV over temperature,

$$Q_{\mathrm{gen}} = \frac{I}{V}(U_{\mathrm{OCV}} - V_{\mathrm{T}}) - \frac{I}{V}(T \cdot \frac{\partial U_{\mathrm{OCV}}}{\partial T}) \,. \tag{15}$$

where V is volume of the cell, U_{OCV} is the open circuit voltage, V_T is the terminal voltage, and $\frac{\partial U_{OCV}}{\partial T}$ is the entropy coefficient.

The equation above becomes zero when the terminal current goes to zero. In fact, heat is continuously generated even though the terminal current is zero during relaxation after charging or discharging. This extra heat source term is generated by ionic current in electrodes caused by the gradient of ion concentrations and is called the heat of mixing that is derived from the relationship between the power input and chemical energy increase and added as an additional heat generation source as shown below [37],

$$Q_{\text{gen.}} = \frac{1}{L}\int_{L}(\Delta U^{+}_{\text{equ}} \cdot i(r,l) - \Delta U^{-}_{\text{equ}} \cdot i(r,l))dl + \frac{I}{V}(U_{\text{OCV}} - V_{\text{T}} - T \cdot \frac{\partial U_{\text{OCV}}}{\partial T}), \quad (16)$$

where U_{equ} and i denote the equilibrium potential and the local current density, respectively.

When a cell is charged or discharged, temperature in the cell varies. Accordingly, ion diffusions in the solid are affected. The dependence of the diffusion coefficient upon variation of temperature can be described using the Arrhenius equation,

$$D_s = D_{s0} \cdot \exp(\frac{E_a}{R}(\frac{1}{T_0} - \frac{1}{T})), \quad (17)$$

where D_{s0}, E_a, and R denote the diffusion coefficient at temperature of T_0, activation energy, and the universal gas constant, respectively. Curve fitting results for temperature dependence of diffusion coefficient is shown in Figure 4.

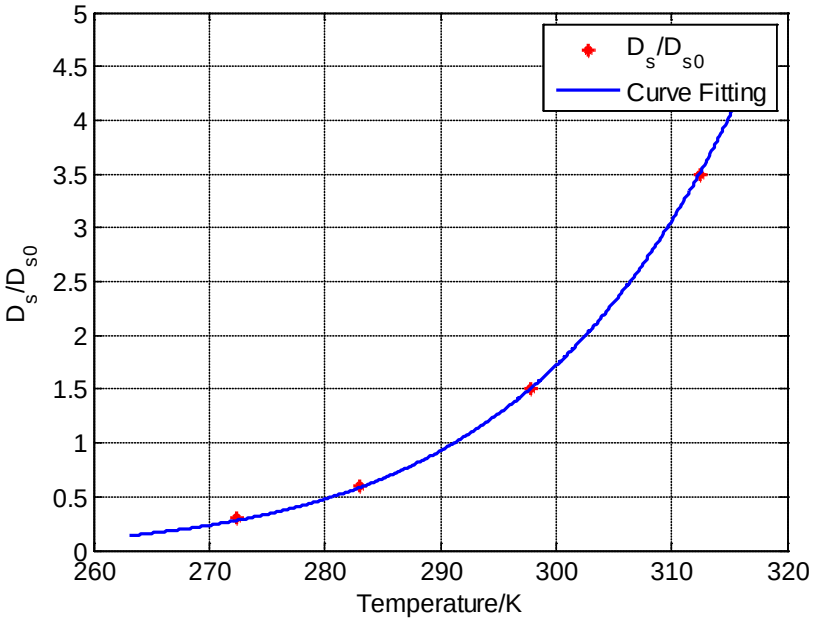

Figure 4. Curve fitting of diffusion coefficient at different temperatures.

In addition, the ion conductivity in the SEI is also affected by the temperature. Impedance of a cell is measured using the Electro-Impedance Spectroscopy (EIS) at different temperatures and a fixed 50% SOC. The Nyquist plot for the cell is shown in Figure 5. The plot shows two semi-circles, one with a relatively small radius and the other with a large radius superposed by a linearly increasing line. The first small semicircle is formed by the impedance of the SEI layer, where the real part presents an ohmic resistance. According to the collected data, the radius of the small semicircle tends to follow the change of the temperature. This relationship is plotted in Figure 6, where an empirical equation is derived and used to consider the temperature dependence of the SEI resistance.

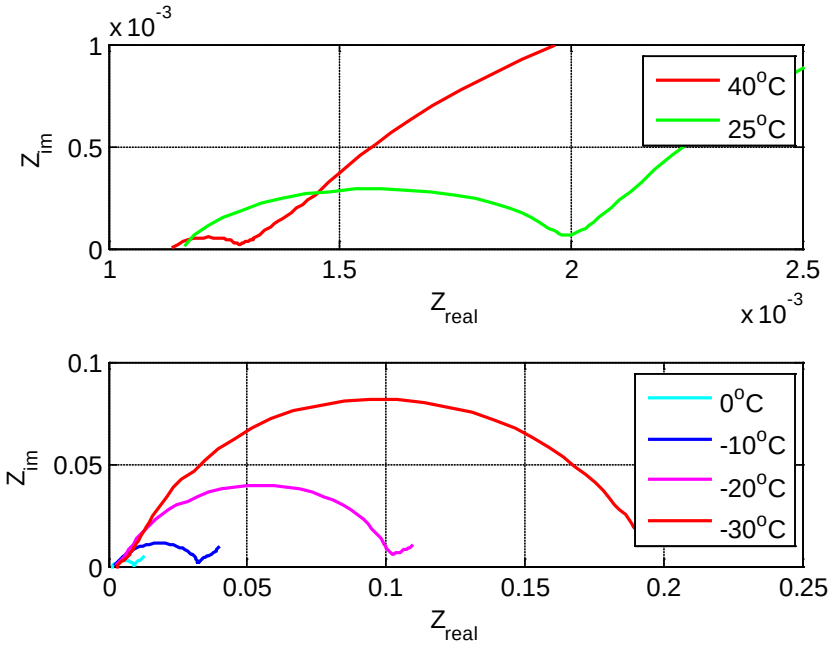

Figure 5. Impedance characteristics of the cell at different temperatures.

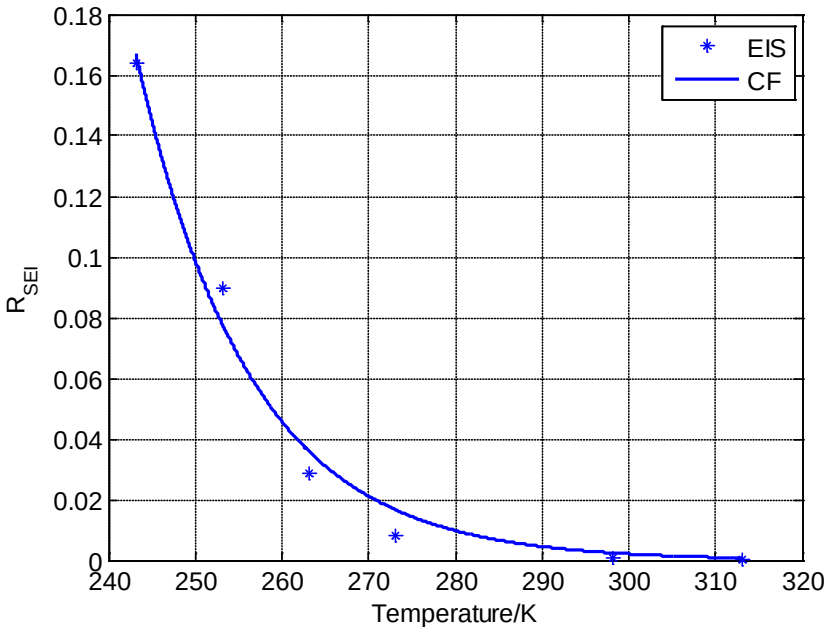

Figure 6. SEI resistance at different temperatures and its interpolation.

2.3 Reduced order modeling of NMC cells

The FOM provides a high accuracy, but needs a high computational time that impedes real-time applications. Therefore, reduction of the FOM has been carried out by simplifying equations for ion concentrations and potentials in electrode and electrolytes.

2.3.1 Polynomial method for ion concentration in electrodes

The governing equation for the ion concentration in electrodes used for the microcell is a partial differential equation (PDE) that is a function of three variables, location of particles, x, the radial coordinate, r and the time, t. In order to solve the PDE numerically, the equation must be discretized. Since there are two coordinates, spherical one for electrodes and Cartesian one for the cell, the concentration in electrodes should be calculated at every node in the cell for a every time step. A high number of nodes in the discretization for two domains increases accuracy of the calculation, but requires a high computational time. Particularly, the high computational time is caused by calculation of concentrations in electrode domain. Therefore, a new formulation for electrode is needed to reduce the computational time and at the same time to represent the dynamics of the ion concentration. The ion concentration in the solid is substituted by a polynomial under an assumption that ion concentrations inside spherical particles are uniform at a radial position within the sphere and represented by a biquadratic equation,

$$c_s(r,t) = a(t) + b(t)\cdot\left(\frac{r^2}{R_s^2}\right) + d(t)\cdot\left(\frac{r^4}{R_s^4}\right), \tag{18}$$

where the three coefficients, $a(t)$, $b(t)$ and $d(t)$ are a function of time.

The three coefficients are obtained by introducing three variables, volume-averaged concentrations, $c_{s,ave}$, volume-averaged concentration fluxes, q_{ave} , and surface concentrations, $c_{s,surf}$,

$$
\begin{aligned}
a(t) &= \frac{39}{4} c_{\mathrm{s,surf}} - 3 q_{\mathrm{ave}} R_{\mathrm{s}} - \frac{35}{4} c_{\mathrm{s,ave}} \\
b(t) &= -35 c_{\mathrm{s,surf}} + 10 q_{\mathrm{ave}} R_{\mathrm{s}} + 35 c_{\mathrm{s,ave}} \\
d(t) &= \frac{105}{4} c_{\mathrm{s,surf}} - 7 q_{\mathrm{ave}} R_{\mathrm{s}} - \frac{105}{4} c_{\mathrm{s,ave}}
\end{aligned}, \tag{19}
$$

where the volume-averaged concentration, volume-averaged concentration flux and surface concentration are defined as follows,

$$
\begin{aligned}
c_{\mathrm{s,ave}} &= \int_{r=0}^{R_{\mathrm{s}}} \frac{3r^2}{{R_{\mathrm{s}}}^3} c_{\mathrm{s}}(r,t) dr \\
q_{\mathrm{ave}} &= \int_{r=0}^{R_{\mathrm{s}}} \frac{3r^2}{{R_{\mathrm{s}}}^3} \left(\frac{\partial}{\partial r} c_{\mathrm{s}}(r,t) \right) dr \\
c_{\mathrm{s,surf}} &= c_{\mathrm{s}}(R_{\mathrm{s}},t) = a(t) + b(t) + d(t)
\end{aligned}. \tag{20}
$$

By combination with the Fick's law and boundary conditions, the three equations of volume-averaged concentration, volume-averaged concentration flux and surface concentration above result in as follows,

$$
\begin{aligned}
&\frac{d}{dt} c_{\mathrm{s,ave}} + 3 \frac{j^{\mathrm{Li}}}{R_{\mathrm{s}} a_{\mathrm{s}} F} = 0 \\
&\frac{d}{dt} q_{\mathrm{ave}} + 30 \frac{D_{\mathrm{s}}}{{R_{\mathrm{s}}}^2} q_{\mathrm{ave}} + \frac{45}{2} \frac{j^{\mathrm{Li}}}{{R_{\mathrm{s}}}^2 a_{\mathrm{s}} F} = 0 \\
&35 \frac{D_{\mathrm{s}}}{R_{\mathrm{s}}} \left(c_{\mathrm{s,surf}} - c_{\mathrm{s,ave}} \right) - 8 D_{\mathrm{s}} q_{\mathrm{ave}} = -\frac{j^{\mathrm{Li}}}{a_{\mathrm{s}} F}
\end{aligned}. \tag{21}
$$

Thus, the ion concentration in electrodes is completely replaced by a set of new equations using the polynomial.

2.3.2 State space approach for Ion concentration in electrolyte

The PDE in equation (21) for ion concentrations in the electrolyte is simplified using dominant eigenvalues found using a state space approach. Assumptions for this approach are the uniform current density in the electrodes and separator,

$$\begin{aligned} j_{-}^{\mathrm{Li}} &= \frac{I}{AL_{-}} && \text{(negative electrode)} \\ j_{\mathrm{sep}}^{\mathrm{Li}} &= 0 && \text{(separator)} \\ j_{+}^{\mathrm{Li}} &= \frac{I}{AL_{+}} && \text{(positive electrode)} \end{aligned}, \tag{22}$$

where L_{-} and L_{+} denote the thickness of negative electrode and positive electrode, respectively.

The PDE can be reformulated using the finite difference method that produces a matrix and written in the state space form as follows,

$$\begin{aligned} \dot{\mathbf{c}}_{\mathbf{e}} &= \mathbf{A}\cdot\mathbf{c}_{\mathbf{e}} + \mathbf{B}\cdot I \\ \mathrm{y} &= \mathbf{C}\cdot\mathbf{c}_{\mathbf{e}} + \mathbf{D}\cdot I \end{aligned}, \tag{23}$$

where I is the current as an input to the system and m×1 vector $\mathbf{c_e}(t)$ is the state variable of the system approximated at discrete node points, $x=x_{\mathrm{i}}$ (i=1,2,…,m).

The transfer function of the state equation above can be transformed into the Laplace domain and expressed as a series of eigenvectors and residues,

$$\frac{\mathbf{Y}(s)}{I(s)} = \mathbf{Z} + \sum_{k=1}^{m} \frac{s\cdot\mathbf{r}_k}{(s-\lambda_k)}, \tag{24}$$

where λ is the eigenvalue, $\mathbf{Z}$ is the steady state vector with m×1 elements, $\mathbf{Z}$=-$\mathbf{CA}^{-1}\mathbf{B}$+$\mathbf{D}$, and $\mathbf{r}$ is the unit step input residue vector with m×1 elements,

$$\mathbf{r}_k = \frac{\mathbf{C}\mathbf{q}_k\mathbf{p}_k\mathbf{B}}{\lambda_k}\left(\mathbf{A}\mathbf{q}_k = \lambda_k\mathbf{q}_k;\ \mathbf{p}_k\mathbf{A} = \lambda_k\mathbf{p}_k\right). \tag{25}$$

Hence, the state space form above is transformed to a modal form given in equation (26)to find out the eigenvalues that dominantly contribute to the dynamics of the system,

$$\begin{aligned}
\hat{\mathbf{A}} &= diag\left[\lambda_1\ \lambda_2 \cdots \lambda_m\right] \\
\hat{\mathbf{B}} &= \left[11\cdots 1\right]^T \\
\hat{\mathbf{C}} &= \left[\mathbf{r}_1\lambda_1\ \mathbf{r}_2\lambda_2 \cdots \mathbf{r}_m\lambda_m\right] \\
\hat{\mathbf{D}} &= \left[\mathbf{Z} + \sum_{k=1}^{m}\mathbf{r}_k\right] = \mathbf{D}
\end{aligned} \quad . \tag{26}$$

The transformed modal form above is replaced by a new state space matrix given in equation (27) that is made of a truncated series of grouped residues with similar eigenvalues. The resulting eigenvalues are obtained from the old eigenvalues with weighed residues,

$$\bar{\mathbf{r}}_f = \sum_{k=k_{f-1}+1}^{k_f}\mathbf{r}_k, \quad \bar{\lambda}_f = \frac{\sum_{k=k_{f-1}+1}^{k_f}\lambda_k\mathbf{r}_{i,k}}{\bar{\mathbf{r}}_{i,f}} \quad . \tag{27}$$

Based on the regrouped eigenvalues, the PDE in equation (28) is reformulated with system matrices that have an nth order as follows.

$$\begin{aligned}
\mathbf{A}^* &= diag\left[\lambda_1\ \lambda_2 \cdots \lambda_n\right] \\
\mathbf{B}^* &= \left[11\cdots 1\right]^T \\
\mathbf{C}^* &= \left[\bar{\mathbf{r}}_1\bar{\lambda}_1\ \bar{\mathbf{r}}_2\bar{\lambda}_2 \cdots \bar{\mathbf{r}}_n\bar{\lambda}_n\right] \\
\mathbf{D}^* &= \left[\mathbf{Z} + \sum_{f=1}^{n}\bar{\mathbf{r}}_f\right]
\end{aligned} \quad . \tag{28}$$

2.3.3 Potentials in both electrolyte and electrodes

When the reaction current is not affected by electrolyte concentration, the second term in the equation (8) for charge conservation can be neglected,

$$\frac{\partial}{\partial x}\left(\kappa_{\mathrm{D}}^{\mathrm{eff}}\frac{\partial}{\partial x}\ln c_{\mathrm{e}}\right) = 0 \quad . \tag{29}$$

In addition, the nonlinear characteristic of the Butler-Volmer equation is approximated with a linear equation below,

$$j^{\mathrm{Li}} = \frac{a_{\mathrm{s}} i_0 F}{RT}\left(\phi_{\mathrm{se}} - U\right), \tag{30}$$

where the phase potential difference, ϕ_{se}, is defined as,

$$\phi_{\mathrm{se}} = \phi_{\mathrm{s}} - \phi_{\mathrm{e}}. \tag{31}$$

Under the assumption that ion conductivity, k^{eff}, is constant, the potential equation becomes,

$$\frac{\partial}{\partial x}\left(\kappa^{\mathrm{eff}} \frac{\partial}{\partial x}\phi_{\mathrm{e}}\right) = \kappa^{\mathrm{eff}} \frac{\partial}{\partial x}\left(\frac{\partial}{\partial x}\phi_{\mathrm{e}}\right). \tag{32}$$

So, the ODE of the potential as shown in equation (5) and (8) can be further simplified as follows,

$$\frac{\partial}{\partial x}\left(\frac{\partial}{\partial x}\phi_{\mathrm{se}}\right) = j^{\mathrm{Li}}\left(\frac{1}{\sigma^{\mathrm{eff}}} + \frac{1}{\kappa^{\mathrm{eff}}}\right). \tag{33}$$

All equations above are coupled to construct a ROM for a single battery cell. For better understanding, the governing equations for FOM and ROM are listed in Table 1.

Table 1 Summary of the difference between FOM and ROM

	FOM	ROM
Ion concentration in solid particles	$\frac{\partial C_s}{\partial t} = \frac{D_s}{r^2}\frac{\partial}{\partial r}\left(r^2 \frac{\partial C_s}{\partial r}\right)$	$\frac{d}{dt}C_{s,ave} + 3\frac{j^{Li}}{R_s a_s F} = 0$ $\frac{d}{dt}q_{ave} + 30\frac{D_s}{R_s^2}q_{ave} + \frac{45}{2}\frac{j^{Li}}{R_s^2 a_s F} = 0$ $35\frac{D_s}{R_s}\left(C_{s,surf} - C_{s,ave}\right) - 8D_s q_{ave} = -\frac{j^{Li}}{a_s F}$
Ion concentration in electrolyte	$\dot{\mathbf{c}}_\mathbf{e} = \mathbf{A}\cdot\mathbf{c}_\mathbf{e} + \mathbf{B}\cdot I$ $\mathrm{y} = \mathbf{C}\cdot\mathbf{c}_\mathbf{e} + \mathbf{D}\cdot I$	$\dot{\mathbf{c}}_\mathbf{e} = \mathbf{A}^*\cdot\mathbf{c}_\mathbf{e} + \mathbf{B}^*\cdot I$ $\mathrm{y} = \mathbf{C}^*\cdot\mathbf{c}_\mathbf{e} + \mathbf{D}^*\cdot I$
Potentials and current density	$\frac{\partial}{\partial x}\left(\sigma^{eff}\frac{\partial}{\partial x}\phi_s\right) - j^{Li} = 0$ $\frac{\partial}{\partial x}\left(k^{eff}\frac{\partial}{\partial x}\phi_e\right) + \frac{\partial}{\partial x}\left(k_D^{eff}\frac{\partial}{\partial x}\ln c_e\right) + j^{Li} = 0$ $j^{Li} = a_s i_0\left\{\exp\left[\frac{\alpha_a F}{RT}\eta\right] - \exp\left[-\frac{\alpha_c F}{RT}\eta\right]\right\}$	$\frac{\partial}{\partial x}\left(\frac{\partial}{\partial x}\phi_{se}\right) = j^{Li}\left(\frac{1}{\sigma^{eff}} + \frac{1}{k^{eff}}\right)$ $j^{Li} = \frac{a_s i_0 F}{RT}\left(\phi_{se} - U\right)$

2.3.4 Reformulation of SOC using the ROM

SOC is an indicator for all of charges that are stored in the anodic electrode and expressed using variables of the ROM. SOC is defined as a ratio of the releasable charge capacity in a cell ($Q_{\text{releasable}}$) to the maximum charge capacity ($Q_{\max}$). The preferred SOC reference should be $Q_{\max}$ rather than the rated charge capacity of a new cell (Q_{rated}) because $Q_{\max}$ decreases as the cell ages. With this approach, the SOC range will always be between 0 and 100%.

$$SOC = \frac{Q_{\text{releasable}}}{Q_{\max.}} \cdot 100\% \tag{34}$$

The SOC varies when a cell is charged or discharged. Percentage of the SOC at any time instant can be calculated as the subtraction from the initial SOC by the integral of current over time,

$$SOC(t) = SOC(0) - \frac{\int_0^{\tau} i(t)\mathrm{dt}}{Q_{\max}} \times 100\% \quad (35)$$

where $SOC(0)$ is the initial SOC at the beginning of the test, SOC(t) is the SOC of the cell at time instant t and $i(t)$ is the current during a time interval, τ.

$Q_{\text{releasable}}$ is a sum of all the charges residing in the particles on the anode side that can be obtained by integrating the volume average charges, $c_{\text{s,ave}}$,in all particles. In reality, some charges cannot be released even at the zero stoichiometric number. In fact, the real releasable charges are the difference between the ideally releasable charges and the number of charges at zero stoichiometric number. Therefore, the $Q_{\text{releasable}}$ and $Q_{\max}$ are expressed using ion concentrations in the electrodes,

$$\begin{aligned} Q_{\text{releasable}} &= \int_0^{L_-} \varepsilon_s \cdot F \cdot c_{\text{s,ave}} \cdot A \cdot dx - \varepsilon_s \cdot F \cdot c_{\text{s,max}} \cdot Stoi_0 \cdot A \cdot L_- \\ Q_{\max} &= \varepsilon_s F c_{\text{s,max}} \cdot (Stoi_{100} - Stoi_0) \cdot A \cdot L_- \end{aligned}, \quad (36)$$

where $Stoi_0$ and $Stoi_{100}$ are the stoichiometry numbers at 0% and 100% SOC, respectively. Accordingly, the SOC is expressed as a ratio between the average lithium concentration and the maximum lithium concentration in particles on the negative electrode from L=0 to L_-.

$$SOC = \left[\frac{1}{L_-} \int_0^{L_-} \frac{(c_{\text{s,ave}} - c_{\text{s,max}} \cdot Stio_0)}{c_{\text{s,max}} \cdot (Stoi_{100} - Stoi_0)} \cdot dx \right] \cdot 100\% \quad (37)$$

2.4 Simulation, experimental validation and analysis

FOM and ROM are developed for a pouch type of Lithium polymer battery and validated experimentally. Key specifications of the cell used for the experiments are as follows;

- Materials: Cathode;$LiMn_2O_4$, anode; Carbon, electrolyte; organic material, and separator; SRS,

- Cell dimensions: 164.2 × 249.6× 5.27 mm^3
- The nominal capacity: 15.7Ah
- Operation range of the terminal voltage: 2.5V to 4.15V.

In addition, a full discharge is the process by which a cell is discharged from 100% SOC to 0% SOC that corresponds to terminal voltages of 4.15V at a cutoff current of 800mA and 2.5V, respectively.

Terminal voltage, current and temperature of cells are measured using a test station designed by our research team. The temperature is the average value of three outputs of thermocouples directly attached to the surface of the cell. Cells are placed in a thermal chamber in order to keep the ambient temperature constant.

2.4.1 Determination of an integration time step

Computational time is dependent upon the integration time step. In order to determine an optimal time step, different currents are applied to the ROM and the responses are analyzed. Terminal voltage, temperature and SOC of the ROM for a cell at different currents are plotted in Figure 7, where the current rates and integration time steps vary. Blue, green, and cyan color show responses at 1C, 2C, and 5C discharge. A solid line and the symbols of plus, star, circle, diamond, and cross show the results of simulation data at different time steps from 100ms, 200ms, 500ms, 1s, 2s to 5s. As expected, the numerical errors in terminal voltage, temperature and SOC are increasing when the integration time step becomes larger. The weighted normalization method is applied to find an optimal integration time, where errors in terminal voltage and temperature are considered. On the other hand, the operating range of SOC for hybrid electric vehicles is from 30% to 80% to prevent a rapid degradation process [38]. In addition, the number of cycles required is

at least 5000 full discharges with less than 10% of capacity fade. These factors can be used as a weighting factor in the method as follows,

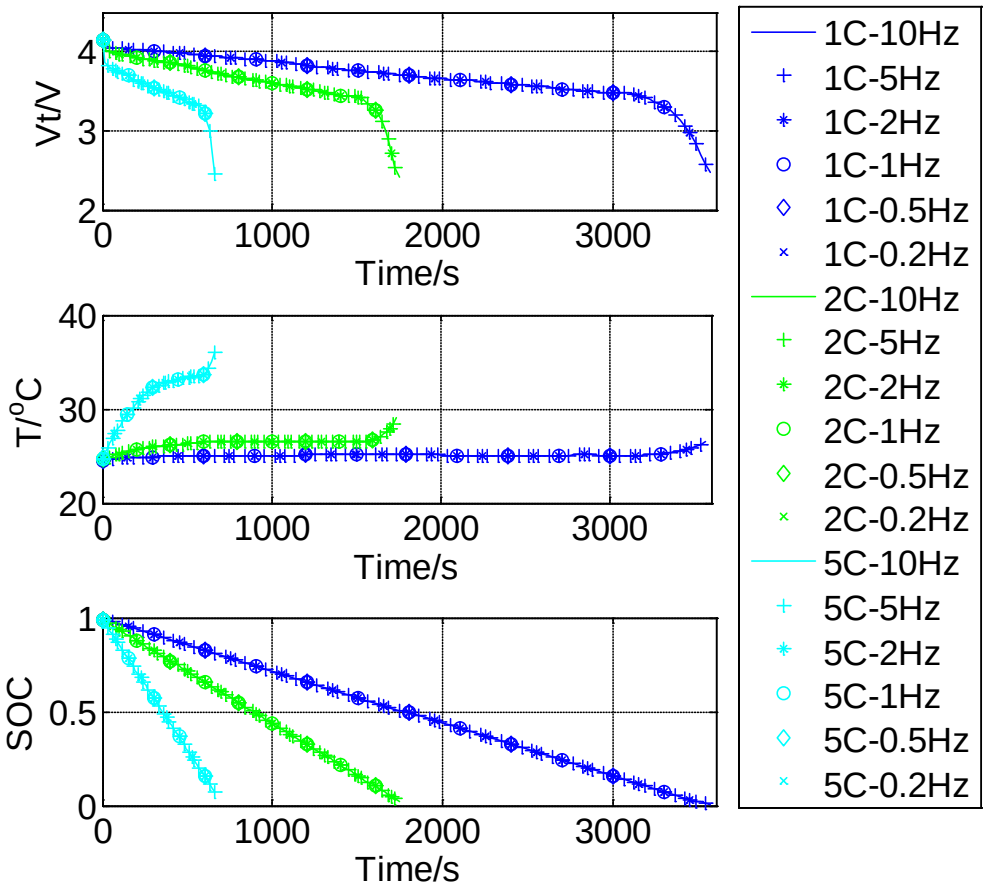

Figure 7. Results of terminal voltage, temperature, and SOC at 1C, 2C and 5C discharge, 1C-10Hz represents the result at the current rate of 1C and the sample frequency is 10Hz.

$$Err = \left(\frac{\sum w_i \left(y_i - \hat{y}_i \right)^2}{\sum w_i} \right)^{\frac{1}{2}}, \tag{38}$$

where y is the simulation data, $\hat{y}$ is the experimental data and w is the weighting factor that is defined as,

$$w = \begin{cases} 2 & 30\% \le SOC \le 80\% \\ 1 & SOC < 30\%, \text{ or } SOC > 80\% \end{cases}. \tag{39}$$

Normalized errors in terminal voltage, temperature and computing times are plotted in Figure 8. The results show that the integration time step should be less than or equal to 2s to ensure no significant error increase in both terminal voltage and temperature. By contrast, the calculation time increases exponentially when the time step is less than 1s. As a result, integration step of 1s for the ROM is optimum for the given application.

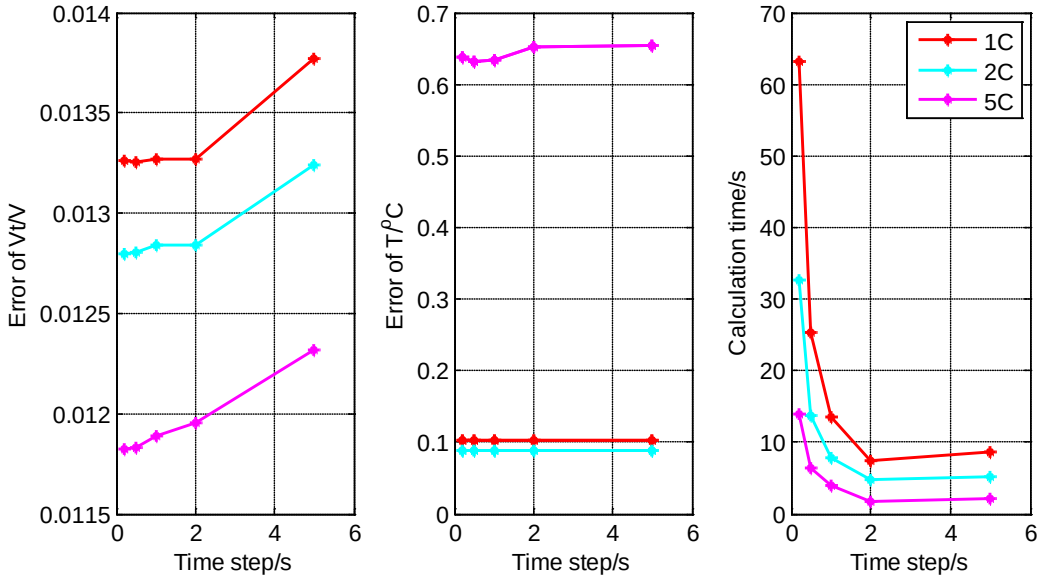

Figure 8. Normalized errors in terminal voltage, temperature and calculation time at 1C, 2C, and 5C discharge and different time-steps.

2.4.2 Performance analysis of the ROM

Performances of the ROM are compared with those of the FOM. Since the errors for SOC calculations are negligibly small and the surface concentrations affect the terminal voltage, only

concentrations in the electrolyte at a discharge are analyzed. A constant current of 1C as the input current is applied to the two models where the initial SOC is set to 80%.

The concentrations in the electrolyte calculated from the FOM (Solid line) and ROM (Stars) are plotted in Figure 10, where the concentrations vary as the time increases. The differences between the two models are caused by the fact that the current density on both electrode sides for the ROM is replaced by the terminal current divided by volume, as shown in equation (22). It is observed that the differences on the negative electrode side are larger than those on the positive electrode side, which are almost negligible. In fact, the concentrations in the electrolyte are affected by current density, as shown in equation (3). Since the ROM uses an average current density, the resulting concentrations are not identical accordingly. In addition, current density gradient on the negative electrode side is larger than that on the positive electrode side. The current density calculated from the FOM (Solid line) and ROM (Dotted line) is shown in Figure. 9. As a result, the differences on the negative electrode side become large.

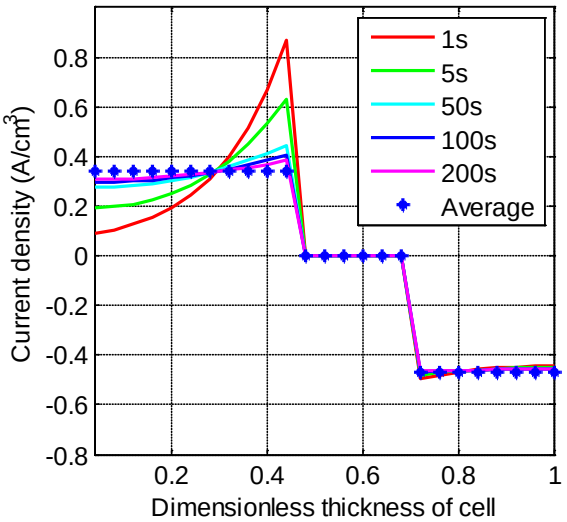

Figure. 9. Current density during 1C constant current discharge at 80% SOC initial condition.

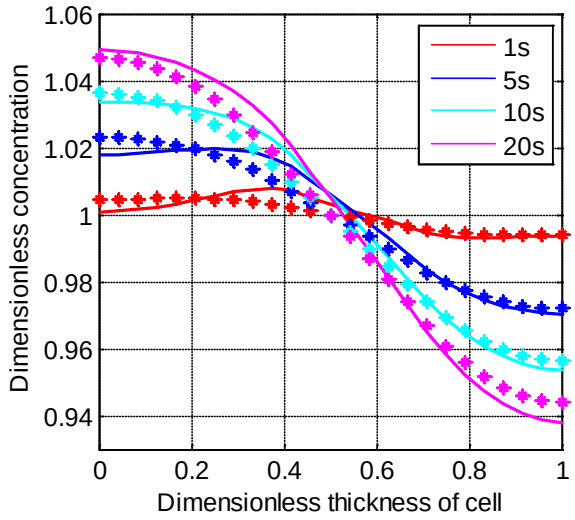

Figure 10. Ion concentration in electrolyte at various times during 1C discharge at 80% SOC initial condition: FOM (-) and ROM (*).

In addition, the computational time of the two models is measured using a PC equipped with a dual core processor of Intel Core I7 CPU 870. The results are shown in Table 2, where 1C, 2C and 5C rate current are applied. The computational time is drastically reduced by the ROM, taking approximately 15% of the time needed for execution of the FOM.

Table 2 Comparison of computation time (Second) between FOM and ROM.

	Full discharge@1C	Full discharge@2C	Full discharge@5C
FOM	79	45	26
ROM	8.7	3.9	2.7

2.4.3 Experimental validation of the ROM

In order to evaluate static and dynamic performance of the ROM developed, experimental data for the pouch type LiPB are collected during charging and discharging and compared with the

simulation results. The parameters related to cell geometry and morphology are provided by manufacturer; some of the parameters are from literature and all the others are from validation with experimental data and.

Maximum solid phase concentration and the stoichiometry are extracted from the measured OCV-SOC curve. The analysis of parameter sensitivity shows that the diffusion coefficients of solid phase affect cell capacity during discharging at various load currents; the diffusion coefficients of electrolyte phase affect the overpotential during discharging at various load currents. Different sets of parameters are optimized based on experimental data at each ambient temperature, then those parameters sensitive to temperature are fitted into the Arrhenius equation

Table 3 List of model parameters (a: Manufacture; b: model validation; c: literature.)

Parameter	Negative electrode	Separator	Positive electrode	unit	
Thickness, δ	$50*10^{-4}$	$25.4*10^{-4}$	$36.4*10^{-4}$	cm	a
Particle radius, R_s	$1*10^{-4}$		$1*10^{-4}$	cm	a
Active material volume fraction, ε_s	0.58		0.5		a
Polymer phase volume fraction, ε_p	0.048	0.5	0.11		a
Conductive filler volume fraction, ε_f	0.04		0.06		a
Porosity, ε_e	0.332	0.5	0.33		a
Maximum solid phase concentration, $c_{s,\,max}$	$16.1*10^{-3}$		$23.9*10^{-3}$	mol cm^{-3}	b
Stoichiometry at 0% SOC: *Stoi*0	0.126		0.936		b
Stoichiometry at 100% SOC: *Stoi*100	0.676		0.442		b
Average electrolyte concentration, c_e	$1.2*10^{-3}$	$1.2*10^{-3}$	$1.2*10^{-3}$	mol cm^{-3}	a
Exchange current density coefficient, k_{i0}	12.9		6.28	A cm^{-2}	c
Charge-transfer coefficient, α_a, α_c	0.5, 0.5		0.5, 0.5		c
Solid phase conductivity, σ	1		0.1	S cm^{-1}	c
Electrolyte phase Li^+ diffusion coefficient, D_e	$2.6*10^{-6}$	$2.6*10^{-6}$	$2.6*10^{-6}$	cm^2 s^{-1}	c
Solid phase Li^+ diffusion coefficient, $D_{s,0}$	$3*10^{-12}$		$5.55*10^{-12}$	cm^2 s^{-1}	b
Activation energy of D_s, $E_{a,D}$	$4.5*10^4$		$4.5*10^4$	J mol^{-1}	b
Film resistance of SEI layer, $R_{SEI,0}$	1000			Ω cm^2	b

Activation energy of R_{SEI}, $E_{a,R}$	$3.8*10^4$			J mol^{-1}	b
Bruggeman's porosity exponent, p	1.5	1.5	1.5		c
Electrolyte phase ionic conductivity, κ	$15.8c_e$ exp(-$13472c_e^{1.4}$)		$15.8c_e$ exp(-$13472c_e^{1.4}$)	S cm^{-1}	c
Li^+ transference number, t_+^0	0.363	0.363	0.363		c

The currents applied to the cells were 1C, 2C, and 5C at a constant ambient temperature of 25°C. The current profile, response of terminal voltage, and temperature during discharging as shown in Figure 11, Figure 12, and Figure 13. During charging, the battery is charged in both CC and CV mode. The current profile, terminal voltage and temperature are plotted in Figure 14, Figure 15, and Figure 16. Comparisons show that the terminal voltage and cell temperature of the ROM are in a fairly good match with those from experiments.

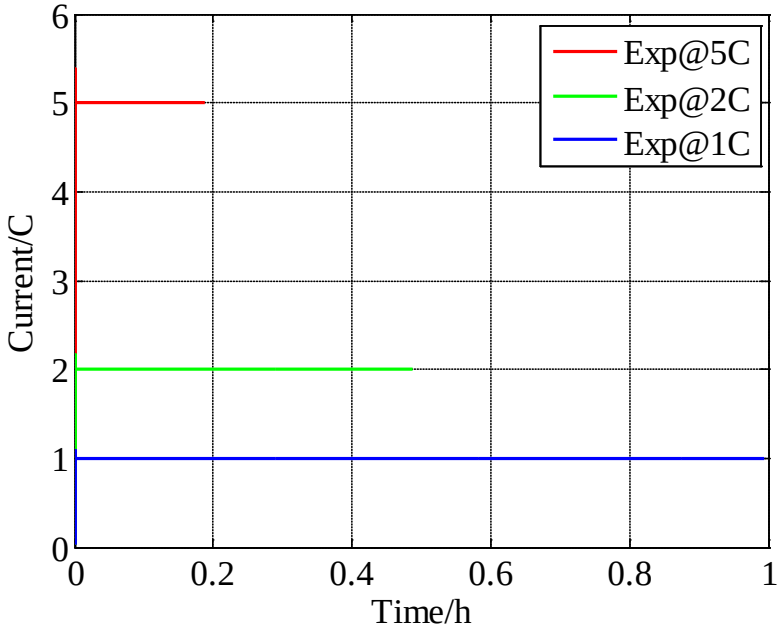

Figure 11. Load profile at 1C, 2C, and 5C during discharging at 25°C.

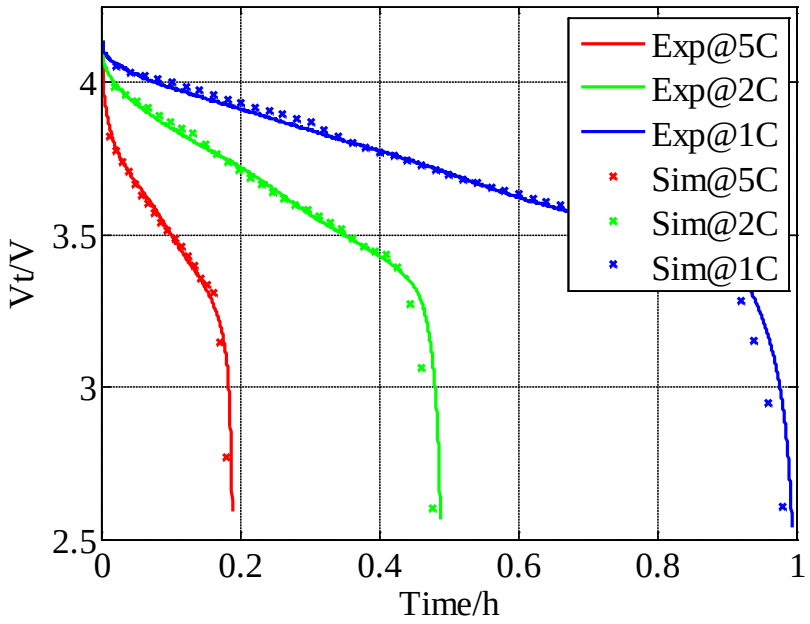

Figure 12. Comparison of terminal voltages from ROM and experiments at 1/2/5C discharge.

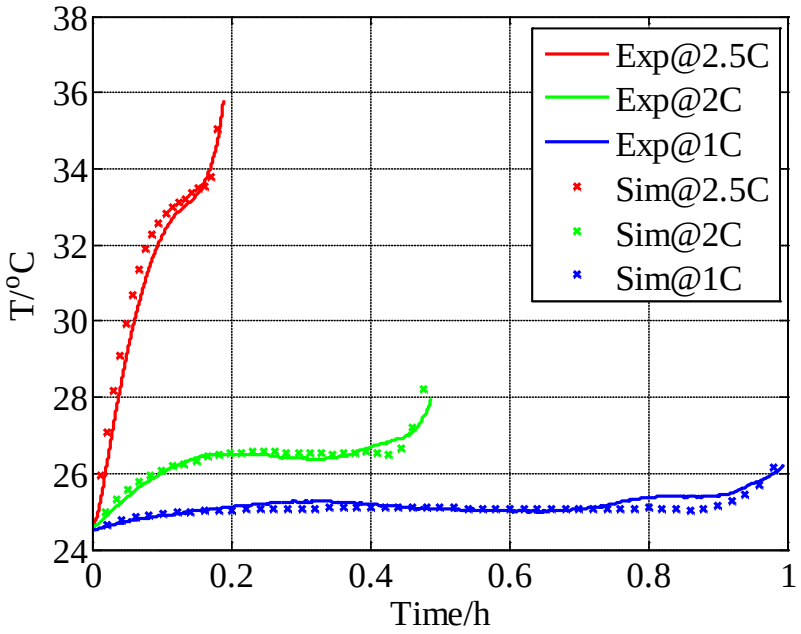

Figure 13. Comparison of temperature between simulation using ROM and experimental data at 1C, 2C and 5C discharge.

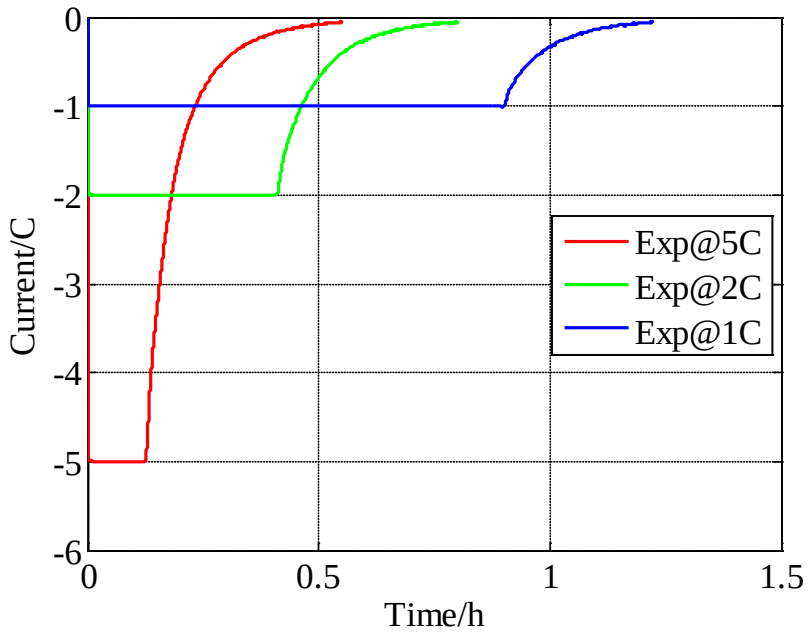

Figure 14. Load profile at 1C, 2C, and 5C during charging at 25°C.

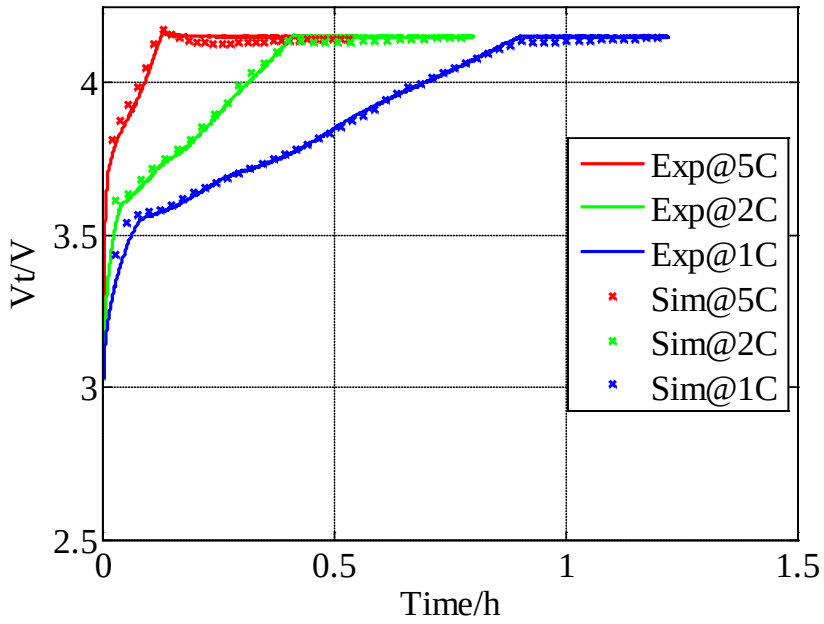

Figure 15. Comparison of terminal voltage between simulation using ROM and experimental data at 1C, 2C and 5C charge.

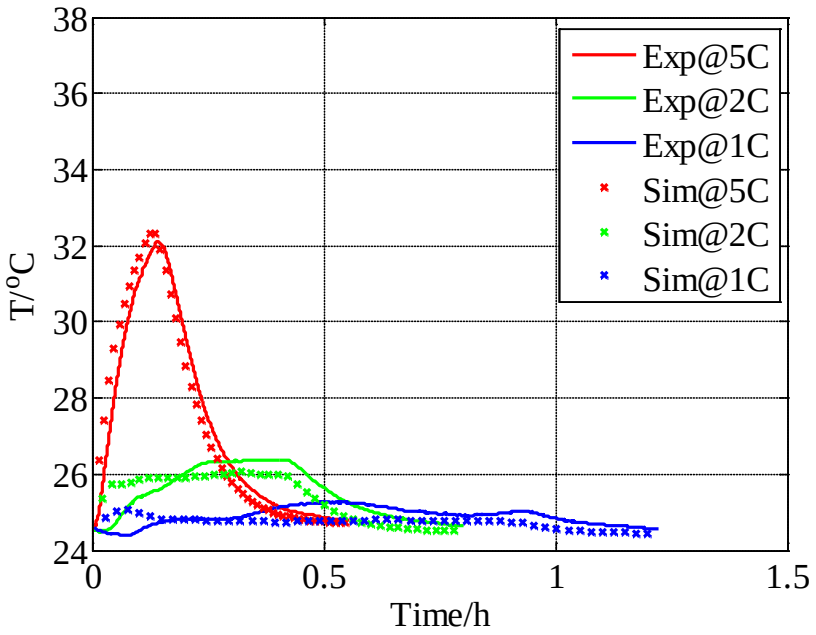

Figure 16. Comparison of temperature between simulation using ROM and experimental data at 1C, 2C and 5C charge.

However, there are two errors in terminal voltage and temperature. Errors in the terminal voltage increase at the end of discharging and at the beginning of charging, where the SOC is low. The terminal voltage is the difference between the OCV and overpotentials that are large at the low SOC. As described in 2.2.3, calculation of overpotentials for the ROM is simplified, which leads to errors in overpotential, then leading to errors in terminal voltage at lower SOC.

Secondly, errors in temperature at low C rates tend to get larger. For example, when 1C discharging and charging current is applied, the errors are observed at 3000s and 200s, as shown in Figure 13 and Figure 16, which is mainly caused by an inaccurate estimation on heat sources. In fact, the second heat source term, as shown in equation (16), is determined by the difference between the OCV and terminal voltage at a given current. As shown in Figure 12, the estimated terminal voltage does not decrease as much as that of the measured data when the discharging current applies. This difference leads to an error in temperature behavior.

On the other hand, there is a delay between the simulated and the measured data of temperature. The calculates temperature rises faster than that of the experimental data when the current rates get high, as shown in Figure 13 and Figure 16. In fact, temperature for this study is measured using three thermocouples placed on the surface of the battery. This delay can be potentially caused by the ignored effect of the heat transfer between layers, where heat is generated, and the surface, where the temperature is measured.

In vehicle applications, the current load profiles vary dynamically. In order to investigate dynamic responses of the ROM, a multi-step current is applied and experimental and simulated data are shown in Figure 17. Initial SOC is set to 80% and then three cycles are applied, where each cycle consists of four operation modes: discharge, rest, charge, and rest, along with increasing current rates: 1C, 2C, and 5C. Each mode lasts for 20s.

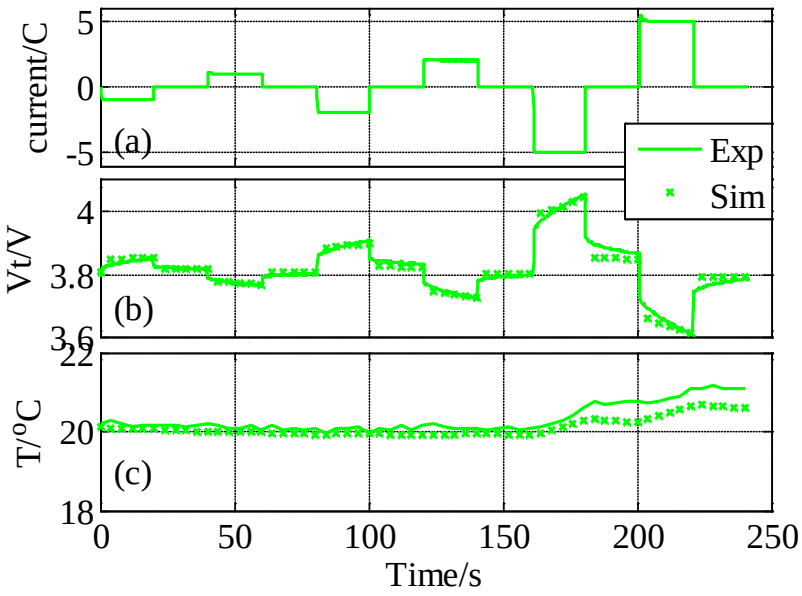

Figure 17. Results of terminal voltage and temperature during pulse discharge at 55% SOC initial condition.

The responses of the ROM follow the experimental data fairly well. However, errors in the terminal voltage and temperature were observed. Particularly, the voltage errors were large at the instants when the abrupt change of current occurs. In fact, the terminal voltage is mainly affected by the ion concentrations on the surface of electrodes. When the current changes abruptly, the concentration near the surface changes immediately. However, the polynomial, as shown in equation (18), does not follow the dynamics of the ion concentration because of the low order of the biquadratic function. Thus, the voltage error results from the inaccurate estimation of the concentration on the surface of electrodes.

Dynamic responses of the ROM are further investigated at three different ambient temperatures of 0°C, 25°C, and 45°C. The input current is shown in Figure 18. The current profile consists of two cycles. The first cycle includes a CC charge at 1C and a CV charge, a rest for 0.5 hour, a full discharge at 2C, and a rest for 1 hour, while the second cycle does a charge at 5C and a CV charge, a rest for 1.25 hour, a full discharge at 1C, and a rest for 1 hour. The rest time is selected so the battery is fully relaxed and reaches an equilibrium state. Responses of the current profile are plotted in Figure 19 and Figure 20.

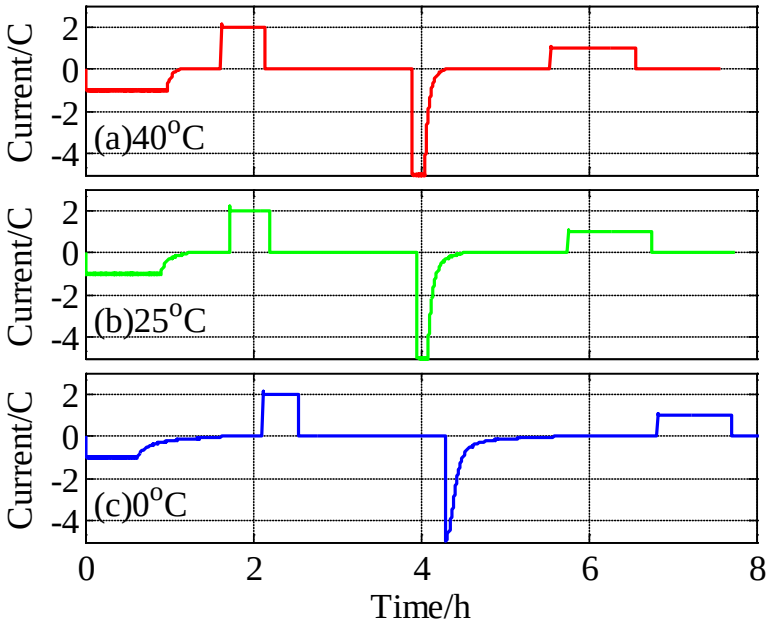

Figure 18. Load profiles for comparison between ROM simulation and experimental data at different temperatures.

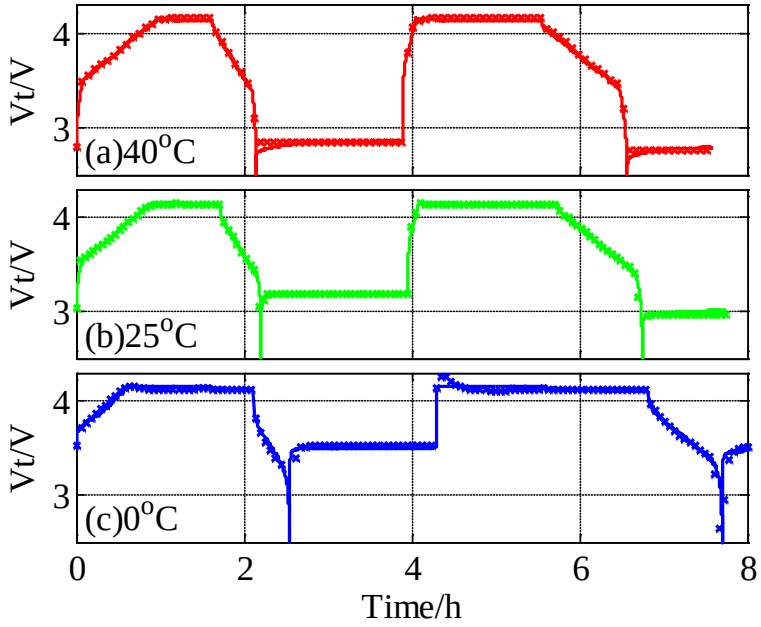

Figure 19. Comparison of terminal voltage between ROM simulation and experimental data at different temperatures.

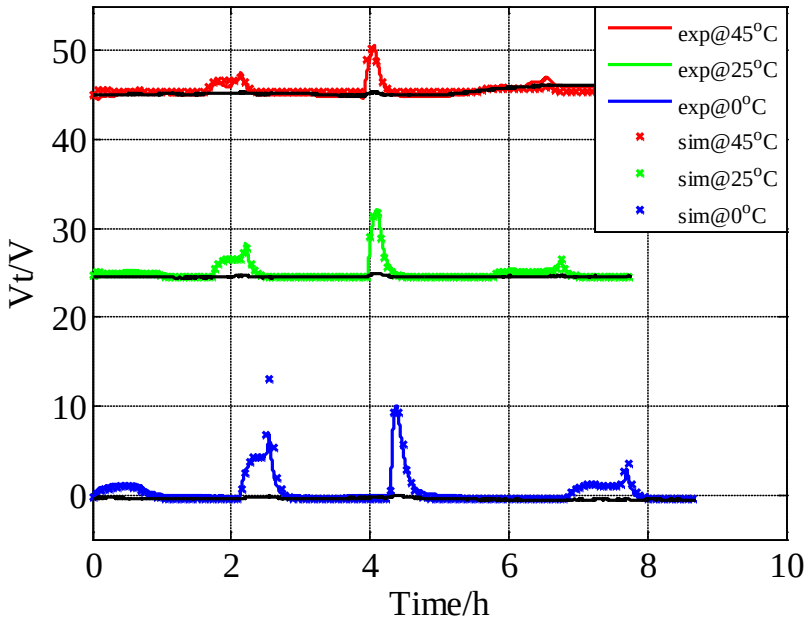

Figure 20. Comparison of temperature between ROM simulation and experimental data at different ambient temperatures.

Comparison of terminal voltage shows a good match between ROM simulation and experimental results. However, the terminal voltage predicted by the ROM increases rapidly during the resting period after a discharge. When discharging, ions in the anodic solid particles start to diffuse and a gradient is formed in the radial direction of particles. While resting, ions get uniformly distributed in the particles and the gradient is slowly reduced. The time needed for ions diffusing from the non-equilibrium state to an equilibrium state is dependent upon characteristics of electrode materials and operation conditions. The mismatch of the time constant in the ROM causes the dynamic voltage errors.

In addition, it is observed that the steady state error in the terminal voltage during the resting period is dependent upon ambient temperature. Particularly, the error tends to increase when temperature drops. In fact, the terminal voltage at the steady state is the same as the OCV. The OCV varies at different SOC that is again a function of maximum capacity of the cell. At the low

ambient temperature, the maximum capacity becomes less than that at high ambient temperature, so the SOC becomes higher and OCV becomes smaller. As a result, the steady state value of the terminal voltage becomes smaller. Since the ROM has not considered the effect of temperature on the maximum capacity, there is a mismatch of terminal voltage during resting period.

Temperature responses at a multiple-step current are plotted in Figure 20, where the ROM follows the experimental data fairly well. There are errors, particularly at low C rate charging, as explained in the previous analysis. In addition, when the ambient temperature is low, the temperature rise becomes higher. At the low ambient temperature, the diffusion coefficient becomes smaller, as shown in Figure 4, so the ions have a high concentration gradient and at the same time the SEI resistance is larger. Consequently, the overpotential becomes higher and the associated heat generation becomes higher according to equation (16).

Moreover, numerical stability of the ROM is tested using a current profile that consists of 5 multiple cycles charging and discharging along with varying amplitude of currents, ranging from 1C to 5C, as shown in Figure 21. Both terminal voltage and temperature at different C rates continue to follow the experimental data after the five cycles and potential errors caused by all of the numerical methods employed stay at a minimum.

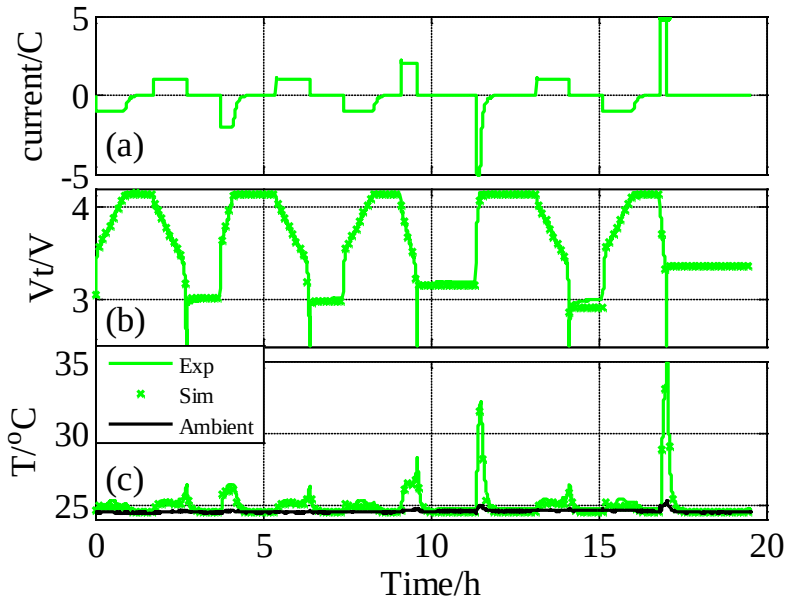

Figure 21. Comparison of terminal voltage and temperature between ROM simulation and experimental data during 5 cycles at 25°C.

2.5 Summary

Based on electrochemical thermal principles, we propose a new ROM that is validated with the FOM and experimental data at different current rates ranging from 1C to 5C, and different ambient temperatures ranging from 0°C to 40°C. In addition, the integration time step for the model is optimized by considering errors in the terminal voltage, temperature and number of cycles.

The performance of the ROM shows promising results with respect to static and dynamic responses, where the terminal voltage and temperature are tested over both a single cycle and multiple cycles.

Major accomplishments and findings are summarized as follows;

- The computational time of the ROM takes less than 15% of the FOM, measured by a PC equipped with a dual core Intel Core I7 CPU 870 processor.

- The terminal voltage is better predicted when effects of temperature on the coefficients have been considered. Particularly, consideration of the temperature dependence of the diffusion coefficient of solid particles and the resistance of the SEI layer increases the accuracy of the terminal voltage and temperature at various operating conditions.
- Prediction of temperature becomes much more accurate after considering the heat of mixing term. The absolute error in the temperature prediction is less than 1.5°C.

Chapter 3 Modeling for LFP

3.1 Review of model with LFP cathode

There has been impressive research focusing on LFP since 1997 [39]. As a promising cathode material, $LiFePO_4$ has been widely used in commercial Li-ion batteries because of excellent safety for its electrochemical and thermal stability, and high rate capacity enhanced especially using nanoparticles in addition to a good cycle life and low cost. All these characteristics enable LFP to be a potential material for applications in electric and hybrid electric vehicles.

Modeling efforts have been made to design estimation algorithms or to understand detailed mechanism of ion transport as well as intercalation and deintercalation process along with material properties. The models widely used for Li-ion battery can be classified into two categories: Electrochemical thermal model based on physical principles, and electric equivalent circuit model composing of a voltage source and electric circuit components. Typically, state-of–charge is calculated using its relationship with open circuit voltage that is estimated from the measured terminal voltage. However, the extreme flat charge/discharge voltage curve of Li ion batteries with LFP chemistry makes it difficult to estimate state-of-charge. In addition, charging/discharging characteristics are dependent upon cycle patterns, so the OCV has some hysteresis. Therefore, a model is needed to predict the SOC in addition to other control purposes. Current electrochemical thermal models using partial differential equations are computationally intensive and cannot be

used for real time applications. Therefore, a ROM is needed for control purpose that reflects two phase transition effects.

Electrochemical thermal models usually involve ion transport between electrodes, chemical reactions at the electrode/electrolyte interface, and ion diffusion and intercalation as well as deintercalation in solid particles. The ion diffusion and distribution dynamics in cathode particles is dependent upon chemistry. For LFP, the lithium ion insertion/extraction reaction takes place through a narrow monophase, a two-phase and another narrow monophase process. The two-phase process is the most dominant one that occurs between lithium deficient phase (α phase: $Li_{\alpha}FePO_4$) and lithium rich phase (β phase: $Li_{1-\beta}FePO_4$). Yamada [40] explains the existence of the monophase region and the reaction of the biphase region with experiments, and estimates nonstoichiometric parameters in the biphase region.

Considering the difference of the conductivity and diffusivity between the two phases, Srinivasan [41] has proposed a shrinking core model that is used to describe the phase change, where the shell of one phase covers the core of the other phase. The model can represent ion diffusion inside of solid particles, and the moving of the interface between the two phases. Wang [42] [43] improves the shrinking core model, assuming that both lithium ion concentration gradient and interface mobility are the driving forces for the two-phase transition. The rate capability is analyzed with different solid solutions and particle size of LFP.

Wheeler [44] has proposed a LFP model based on sandwich structure that considers the phase-change diffusivity with a concentration-dependent solid diffusion coefficient. The model can represent the effect of carbon coating and inter-particle contacts with a spreading resistance. Without considering the two-phase transition process or the porous electrode, Safari [45] also proposed a model with an empirical equation that includes a diffusion coefficient dependent on

the average concentration inside of a particle. The model also considers a resistive-reactant feature caused by the insolation of LFP materials. The results are capable of representing the asymmetry between the charge and discharge curves.

Srinivasan [46] shows that the behavior of LFP cells at a particular SOC depends on the path by which the SOC is reached, which is called path dependence of SOC. The mechanism of the phenomena is explained using a shrinking core model considering the cycling history that affects the diffusion length. Roscher's research [47] on load history dependent cell impedance is consistent with Srinivasan's description. In addition, effects of load history on power capability and available capacity are also analyzed. Safari [48] also proposes a model including the path dependence of the LFP electrode, but without considering phase transitions.

More and more researchers have experimentally proved the moving boundary theory. Phase transition and phase boundary propagation during delithiation in LFP particles is observed using electron energy loss spectroscopy [49] [50]. The lithium ion diffusion coefficient measured by Churikov [51] shows its dependence on the ratio between two phases. However, there is no physical model available for LFP chemistry employing the moving boundary along with multiple layers to analyze path dependence yet. Therefore, we propose a reduced model for real time application of LFP cells, whose cathode is made of micro-size secondary particles. [23]. The model considers the two-phase transition, moving boundary, and multiple layers, which represents responses at both charging and discharging, and the path dependence of the LFP cathode.

3.2 Full order modeling of LFP

3.2.1 Modeling principles

Working principles of cells with LFP cathodes are similar to those of $LiMn_2O_4$ (LMO) or $LiNi_xMn_yCo_{1-x-y}O_2$ (NMC) cathodes. Ion transport and intercalation as well as deintercalation are

described using electrochemical kinetics, mass and charge balance and Ohm's law. The LMO cells are extensively analyzed in a previous work [23] and summarized in Table 6, The values of parameters are listed in . The only difference between the LMO/NMC and LFP chemistry is the mechanism of ions intercalation and deintercalation in solids that are described below.

Table 4 Summary of the governing equations for a FOM and ROM of LMO cells

Equation description	Full order equations	Reduced order equations
Ion concentration in the solid phase	$\frac{\partial c_s}{\partial t} = \frac{D_s}{r^2}\frac{\partial}{\partial r}\left(r^2 \frac{\partial c_s}{\partial r}\right)$ $\frac{1}{r}\frac{\partial c_s}{\partial r}\Big\|_{r=0} = 0$ $D_s \frac{\partial c_s}{\partial r}\Big\|_{r=R_s} = \frac{-j^{Li}}{a_s F}$	$\frac{d}{dt}c_{s,ave} + 3\frac{j^{Li}}{R_s a_s F} = 0$ $\frac{d}{dt}q_{ave} + 30\frac{D_s}{R_s^2}q_{ave} + \frac{45}{2}\frac{j^{Li}}{R_s^2 a_s F} = 0$ $35\frac{D_s}{R_s}\left(c_{s,surf} - c_{s,ave}\right) - 8D_s q_{ave} = -\frac{j^{Li}}{a_s F}$
Ohm's law in the solid phase	$\frac{\partial}{\partial x}\left(\sigma^{eff}\frac{\partial}{\partial x}\phi_s\right) - j^{Li} = 0$ $-\sigma^{eff}\frac{\partial}{\partial x}\phi_s\Big\|_{x=0} = -\sigma^{eff}\frac{\partial}{\partial x}\phi_s\Big\|_{x=L} = \frac{I}{A};$ $\frac{\partial}{\partial x}\phi_s\Big\|_{x=L_-} = \frac{\partial}{\partial x}\phi_s\Big\|_{x=L_- + L_{sep}} = 0$	$\frac{\partial}{\partial x}\left(\frac{\partial}{\partial x}\phi_{se}\right) = j^{Li}\left(\frac{1}{\sigma^{eff}} + \frac{1}{\kappa^{eff}}\right)$
Ohm's law in the solution phase	$\frac{\partial}{\partial x}\left(\kappa^{eff}\frac{\partial}{\partial x}\phi_e\right) + \frac{\partial}{\partial x}\left(\kappa_D^{eff}\frac{\partial}{\partial x}\ln c_e\right) + j^{Li} = 0$ $\frac{\partial}{\partial x}\phi_e\Big\|_{x=0} = \frac{\partial}{\partial x}\phi_e\Big\|_{x=L} = 0$	
Butler-Volmer equation	$j^{Li} = a_s i_0 \left\{ \begin{array}{l} \exp\left[\frac{\alpha_a F}{RT}(\eta - \eta_{SEI})\right] \\ -\exp\left[-\frac{\alpha_c F}{RT}(\eta - \eta_{SEI})\right] \end{array} \right\}$ $\eta = \phi_s - \phi_e - U$	$j^{Li} = \frac{a_s i_0 F}{RT}\left(\phi_{se} - U\right)$
Ion concentration in the solution phase	$\frac{\partial(\varepsilon_e c_e)}{\partial t} = \frac{\partial}{\partial x}\left(D_e^{eff}\frac{\partial}{\partial x}c_e\right) + \frac{1-t_+^0}{F}j^{Li}$ $\frac{\partial c_e}{\partial t}\Big\|_{x=0} = \frac{\partial c_e}{\partial t}\Big\|_{x=L} = 0$	
SOC definition	$SOC = \left[\frac{1}{L_-}\int_0^{L_-}\frac{(c_{s,ave} - c_{s,max}\cdot Stio0)}{c_{s,max}\cdot(Stoi100 - Stoi0)}\cdot dx\right]\cdot 100\%$	

Table 5 List of model parameters (a: Manufacture; b: validation; c: estimated.)

Parameter	Negative electrode	Separator	Positive electrode		unit	
			α phase	β phase		
Electrode plate area, A	13.30		12.60		cm^2	a
Thickness, δ	$65*10^{-4}$	$16*10^{-4}$	$162*10^{-4}$		cm	a
Particle radius, R_s	$8.5*10^{-4}$		$12.5*10^{-4}$		cm	a
Active material volume fraction, ε_s	0.62		0.56			a
Polymer phase volume fraction, ε_p	0.017	0.5	0.065			a
Conductive filler volume fraction, ε_f	0.013		0.025			a
Porosity, ε_e	0.35	0.5	0.35			a
Average electrolyte concentration, c_e	0.0123	0.0123	0.0123		mol cm^{-3}	a
Maximum solid phase concentration, $c_{s,max}$	0.042		0.012		mol cm^{-3}	c
Diffusion coefficient in solid, D_s	$2.20*10^{-9}$		$4.27*10^{-9}$	$2.56*10^{-8}$	$cm^2\ s^{-1}$	b
Diffusion coefficient in electrolyte, D_e	$2.60*10^{-6}$	$2.60*10^{-6}$	$2.60*10^{-6}$			b
Limitation concentration ($c_{s,\alpha\beta}/\ c_{s,max}$)			0.064	0.8		b
Stoichiometry at 0% SOC, $Stoi_0$	0.1155		0.9059			b
Stoichiometry at 100% SOC, $Stoi_{100}$	0.6958		0.0064			b
Equilibrium potential of positive electrode	$3.4245+0.85\cdot\exp(-400\cdot y^{1.3})-17\cdot\exp(-0.98\cdot y^{-14})$, $y= c_{s,surf}/\ c_{s,max}$					a,b
Equilibrium potential of negative electrode	$(0.1011-0.04\cdot\tanh(13.76\cdot x-8.4))\cdot(x<=1)-252.707\cdot(x-0.854)^3\cdot(x>0.854\ \&\ x<=1)+(0.0523-0.05275\cdot\tanh(14.05\cdot x-0.856))\cdot(x<=0.4)+(71.43\cdot(x-0.085)^2)\cdot(x<=0.085)$; $x= c_{s,surf}/\ c_{s,max}$					a,b

For a lithium cell with graphite anode and LFP cathode, lithium ions extract from anode to insert into cathode during discharging, and vice versa. The insertion of lithium ion into $FePO_4$ during discharging and extraction from $LiFePO_4$ during charging can be described as,

$$\begin{aligned} &FePO_4 + xLi^+ + xe^- \xrightarrow{\text{discharge}} xLiFePO_4 + (1-x)FePO_4 \\ &LiFePO_4 - xLi^+ - xe^- \xrightarrow{\text{charge}} xFePO_4 + (1-x)LiFePO_4. \end{aligned} \tag{40}$$

When LFP cells are charged or discharged, there are transitions between single phase and two-phase dependent upon ion concentration inside of particles. This transition versa is schematically depicted in Figure 22. When a cell of 100% SOC is discharged, lithium ions transported from anode to cathode diffuse into LFP particles, which creates a single phase called α phase, as shown in the particle 5 of Figure 22. While the discharging process continues, the ion concentration on the surface of the particles get increased and saturated with a value, $c_{s,\alpha\beta}$, then creates a new phase called β phase. The concentration in β phase is equal to or larger than the maximum value of $c_{s,\beta\alpha}$. With more ions inserted and diffused in the particle, the region of α phase decreases, while the region of β phase grows, and the region where two phases coexist is called a two-phase region shown with particle 6 to 8. As discharging continues, the cell finally reaches a low SOC, α phase gets depleted and only β phase is present, so a single-phase exists, which is called a single phase region of β as shown in particle 1. This two-phase dynamics can be described using a two-phase transition and the moving interface [41].

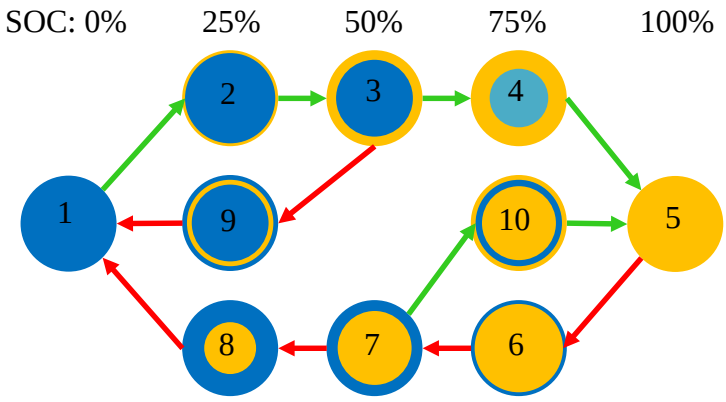

Figure 22. Juxtaposition of phases in LFP particles at different SOCs with different cycling history: Green and red arrows for discharging and charging, respectively; blue and yellow color for β and α phase.

When the cell is sufficiently rested, it can be assumed that there is no gradient of the ion distribution in a particle. Ion distribution for LFP particles is determined by the juxtaposition of the two phases that depends on the cycling history of the cell. When a battery that has an initial value of 0% SOC is charged to 50% SOC, the particle in the shell finds itself in β phase, but in the core α phase, as shown the step 1→2→3 in Figure 22. Conversely, the particle becomes α phase in the shell and β phase in the core, as shown with step 5→6→7, when the battery is discharged from 100% SOC to 50%. Besides juxtapositions, the number of layers at the same SOC can be different. When being discharged from 50% to 25% SOC, the particles might have two layers with β on the surface as shown with step 7→8 , or three layers as shown with step 3→9. Consequently, multiple layers can be formed during charging and discharging.

When particles are in single phase, as shown in Figure 22, the ion diffusion within particles is simply described using Fick's law of diffusion. The governing equation of ion concentration c_s in a particle with a radius of R_s and the boundary conditions on the surface of the particle are as follows,

$$\begin{aligned} &\frac{\partial c_s}{\partial t} = \frac{D_s}{r^2}\frac{\partial}{\partial r}\left(r^2 \frac{\partial c_s}{\partial r}\right) \\ &D_s \frac{\partial c_s}{\partial r}\Big|_{r=0} = 0 \\ &D_s \frac{\partial c_s}{\partial r}\Big|_{r=R_s} = \frac{-j^{Li}}{a_s F} \end{aligned} \quad , \tag{41}$$

where r is the radial coordinate, ε_s is the volume fraction of active material, D_s is the solid phase diffusion coefficient, j^{Li} is the current density, a_s is the interfacial surface area calculated from 3 ε_s/R_s, and F is the Faraday's constant. The diffusivity of α and β phase are different, so the value of the diffusion coefficient depends on the phase of the particle.

When two layers are formed, as shown with steps from 2 to 4 and 6 to 8 in Figure 22, Fick's law can be extended to describe ion diffusion, where boundary conditions are different. When a fully charged battery is being discharged, the ion concentration increases at the surface of the particle, and creates β phase. The interface between two phases moves into the center of the particle. Correspondingly, the governing equations for ion concentration in the two-regions are as follows,

$$\frac{\partial c_s}{\partial t} = \frac{D_{s,\alpha}}{r^2}\frac{\partial}{\partial r}\left(r^2 \frac{\partial c_s}{\partial r}\right), \quad D_{s,\alpha}\frac{\partial c_s}{\partial r}\Big|_{r=0} = 0 \tag{42}$$

$$\frac{\partial c_s}{\partial t} = \frac{D_{s,\beta}}{r^2}\frac{\partial}{\partial r}\left(r^2 \frac{\partial c_s}{\partial r}\right), \quad D_{s,\beta}\frac{\partial c_s}{\partial r}\Big|_{r=R_s} = \frac{-j^{Li}}{a_s F} \tag{43}$$

The location of the moving interface between layer 1 and layer 2, as shown in (a) of Figure 23, can be calculated based on ion concentration. Assuming the moving interface between the two regions is driven only by the concentration gradient of ions that are distinct in the two phases, the governing equation for the moving interface of the mass balance can be rewritten as,

$$\left(c_{s,\beta\alpha} - c_{s,\alpha\beta}\right)\frac{\mathrm{d}r_0}{\mathrm{d}t} = D_{s,\alpha}\frac{\partial c_s}{\partial r}\Big|_{r=r_{0-}} - D_{s,\beta}\frac{\partial c_s}{\partial r}\Big|_{r=r_{0+}}. \tag{44}$$

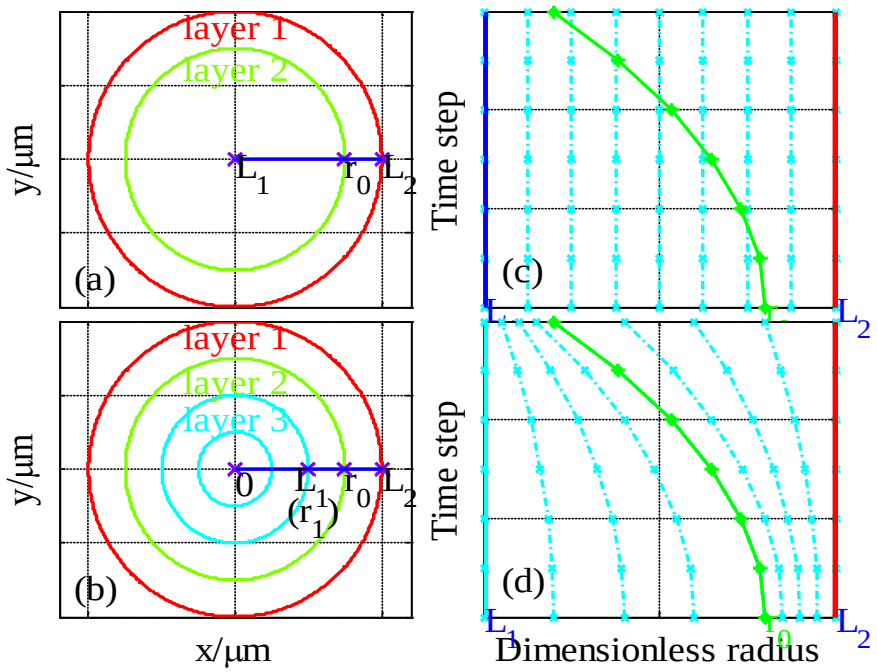

Figure 23. Fixed finite difference grid

When a fully charged battery is being discharged, there is a state that β phase generated on the surface as shown in particle 7. After a period when discharging stops and then a charging current is applied, the ion concentration at the surface of LFP particles decreases and α phase is created, which results in three layers, as shown with particle 10 in Figure 22, and more details are shown in (b) of Figure 23. The ion concentration in multiple layers can be described by modified Fick's law and the following assumptions are made: the ion concentration in Layer 3 and the inner layers does not change, and the location of the interface between Layer 2 and Layer 3 does not moving during cell operation,

$$\frac{\partial c_s}{\partial t} = \frac{D_{s,\beta}}{r^2}\frac{\partial}{\partial r}\left(r^2\frac{\partial c_s}{\partial r}\right), \qquad D_{s,\beta}\frac{\partial c_s}{\partial r}\Big|_{r=r_1} = 0 \tag{45}$$

$$\frac{\partial c_s}{\partial t} = \frac{D_{s,\alpha}}{r^2}\frac{\partial}{\partial r}\left(r^2 \frac{\partial c_s}{\partial r}\right), \qquad (46)$$

$$D_{s,\alpha}\frac{\partial c_s}{\partial r}\Big|_{r=R_s} = \frac{-j^{Li}}{a_s F}$$

$$\left(c_{s,\alpha\beta} - c_{s,\beta\alpha}\right)\frac{\mathrm{d}r_0}{\mathrm{d}t} = D_{s,\beta}\frac{\partial c_s}{\partial r}\Big|_{r=r_0-} - D_{s,\alpha}\frac{\partial c_s}{\partial r}\Big|_{r=r_0+}, \qquad (47)$$

where r_0 is the location of the interface between layer 1 and layer 2, while r_1 is the location of the interface between layer 2 and layer 3, as shown in (b) of Figure 23.

3.2.2 Numerical method

The equations describing ion diffusion are partial differential equations (PDE) that can be solved using the finite difference method in both time domain and space domain. To achieve high numerical accuracy and better stability, the Crank-Nicholson implicit method is employed. The location of the boundary is a function of both time and space, as seen in the PDEs of (2) to (12), which is called 'moving boundary' problem or Stefan problem. This problem can be solved by either fixed finite difference grid method or variable space grid method. The appropriateness of two methods are studied with respect to their scheme.

For the fixed finite difference method, at different time steps the moving boundary r_0 is plotted in green curve, and the fixed boundary of L1 and L2 are plotted in blue and red lines as (c) of Figure 23 shows, where the boundary is not always on the grid points, but is located between two grid points. So the space derivatives on the moving boundary need to be modified.

An alternative method is to modify the space grid. The variable space grid [52] and the moving boundary are shown in (d) of Figure 23. With the following transformation, two new space coordinates are created as,

$$x = \frac{r - L_2}{r_0 - L_2}, \text{for layer} 1, \qquad (48)$$

$$y = \frac{r - L_1}{r_0 - L_1}, \text{for layer2} \tag{49}$$

So the moving boundary is always on the grip point of x=1 at any time instant. According to equation (45)in 3.2.1, the left term in the PDEs could be transformed from r domain to x and y domain for the cell and the core, respectively,

$$\begin{aligned} &\left(\frac{\partial c_s}{\partial t}\right)_r = \left(\frac{\partial c_s}{\partial x}\right)_t \left(\frac{\partial x}{\partial t}\right)_x + \left(\frac{\partial c_s}{\partial t}\right)_x \\ &\frac{\mathrm{d}x}{\mathrm{d}t} = \frac{\partial x}{\partial r_0}\frac{\mathrm{d}r_0}{\mathrm{d}t} \end{aligned}. \tag{50}$$

And the governing equations and the boundary conditions in (42) to (44) and (45) to (47) could be transformed to (51) to (53),

$$\begin{aligned} &\left(r_0 - L_1\right)^2 \frac{\partial c_s}{\partial t} = D_{s,y} \frac{\partial^2 c_s}{\partial y^2} + \left(r_0 - L_1\right)\left(y\frac{\mathrm{d}r_0}{\mathrm{d}t} + \frac{2D_{s,y}}{L_1 + y\left(r_0 - L_1\right)}\right)\frac{\partial c_s}{\partial x} \\ &D_{s,y}\frac{\partial c_s}{\partial y}\bigg|_{y=0} = 0 \end{aligned} \tag{51}$$

$$\begin{aligned} &\left(r_0 - L_2\right)^2 \frac{\partial c_s}{\partial t} = D_{s,x} \frac{\partial^2 c_s}{\partial x^2} + \left(r_0 - L_2\right)\left(x\frac{\mathrm{d}r_0}{\mathrm{d}t} + \frac{2D_{s,x}}{L_2 + x\left(r_0 - L_2\right)}\right)\frac{\partial c_s}{\partial x} \\ &\frac{D_{s,x}}{\left(r_0 - L_2\right)}\frac{\partial c_s}{\partial x}\bigg|_{x0} = \frac{-j^{\mathrm{Li}}}{a_s F} \end{aligned}. \tag{52}$$

$$\left(c_{s,yx} - c_{s,xy}\right)\frac{\mathrm{d}r_0}{\mathrm{d}t} = \frac{D_{s,x}}{r_0 - L_2}\frac{\partial c_{s,x}}{\partial x}\big|_{x=1} - \frac{D_{s,y}}{r_0 - L_1}\frac{\partial c_{s,y}}{\partial r}\big|_{y=1} \tag{53}$$

where the sub-index of diffusion coefficient Ds and concentration c_s represent the phase of the layer, x for layer 1 and y for layer 2.

3.3 Reduced order modeling of LFP

The equations introduced in section 3.2.2 are partial differential equations, the order of which needs to be reduced to find a viable solution for real time applications. One of the order reduction methods used for ion concentrations in NMC cells is the polynomial approach. When there exists

single α or β phase, the approach applied to NMC cells can be used, but the coexistence of two-phase in particles requires modification of the method considering the number of layers.

Two phase states in the particles during discharging process are approximated with a core of α phase and a shell of β phase. The concentration in α phase is assumed to be a biquadratic function of spatial position, while concentration in β phase is assumed to be a quadratic function of spatial coordinate.

For the inner layer of α phase,

$$\begin{aligned} & c_{\mathrm{s}}(r,t) = a(t) + b(t)\cdot\left(\frac{r^2}{r_0^2}\right) + d(t)\cdot\left(\frac{r^4}{r_0^4}\right) \\ & \frac{1}{r}\frac{\partial c_{\mathrm{s}}}{\partial r}\Big|_{r=0} = 0 \\ & c_{\mathrm{s}}(r_0,t) = c_{\mathrm{s},\alpha\beta} \end{aligned} \quad , \tag{54}$$

where the coefficients, $a(t)$, $b(t)$ and $d(t)$ denote the coefficients that are a function of time, and r_0 is the current location of the interface between the outer two phases and r_1 is the current location of the interface between the inner two phases, which is assumed to be constant.

Similar to the reduction method introduced in [23], the three coefficients are obtained by introducing three variables, volume-averaged concentrations $c_{s,ave}$, volume-averaged concentration fluxes q_{ave}, and surface concentrations $c_{s,surf}$, which is a constant,

$$\begin{aligned} a(t) &= \frac{39}{4}c_{\mathrm{s,surf}} - 3q_{\mathrm{ave}}R_{\mathrm{s}} - \frac{35}{4}c_{\mathrm{s,ave}} \\ b(t) &= -35c_{\mathrm{s,surf}} + 10q_{\mathrm{ave}}R_{\mathrm{s}} + 35c_{\mathrm{s,ave}} \\ d(t) &= \frac{105}{4}c_{\mathrm{s,surf}} - 7q_{\mathrm{ave}}R_{\mathrm{s}} - \frac{105}{4}c_{\mathrm{s,ave}} \end{aligned} \quad . \tag{55}$$

Combined with (52) and (53) , the three equations of volume-averaged concentration, volume-averaged concentration flux and surface concentration above result in as following,

$$\begin{aligned}
&\frac{d}{dt}c_{\mathrm{s,ave}} - 3\frac{D_{\mathrm{s}}}{r_0^{\,2}}\left(35\left(c_{\mathrm{s,surf}} - c_{\mathrm{s,ave}}\right) - 8q_{\mathrm{ave}}r_0\right) = 0 \\
&\frac{d}{dt}q_{\mathrm{ave}} + \frac{1}{2}\frac{D_{\mathrm{s}}}{r_0^{\,3}}\left(60q_{\mathrm{ave}}r_0 - 45\right)\left(35\left(c_{\mathrm{s,surf}} - c_{\mathrm{s,ave}}\right) - 8q_{\mathrm{ave}}r_0\right) = 0
\end{aligned} \quad . \tag{56}$$

For the outer layer of β phase,

$$\begin{aligned}
&c_{\mathrm{s}}(r,t) = a(t) + b(t)\cdot\left(r - r_0\right) + d(t)\cdot\left(r - r_0\right)^2 \\
&D_{\mathrm{s}}\left.\frac{\partial c_{\mathrm{s}}}{\partial r}\right|_{r=R_{\mathrm{s}}} = \frac{-j^{\mathrm{Li}}}{a_{\mathrm{s}}F} \\
&c_{\mathrm{s}}(r_0,t) = c_{\mathrm{s},\beta\alpha}
\end{aligned} \quad , \tag{57}$$

where the coefficients of $a(t)$, $b(t)$ and $d(t)$ are also a function of time. The three coefficients are derived from three new variables, averaged ion concentration in β phase, $c_{s,ave}$, ion concentration on the particle surface, $c_{s,surf}$, and the location of the interface, r_0.

The averaged ion concentration in β phase can be obtained as,

$$\begin{aligned}
&c_{\mathrm{s,ave}} = \frac{\int_{r_0}^{r_s} 4\pi r^2 C_s(r,t)\mathrm{d}r}{\frac{4}{3}\pi r^2} = a(t) + b(t)*k_1 + d(t)*k_2 \\
&k_1 = \frac{3}{4}\left(\frac{r_s^4 - r_0^4}{r_s^3 - r_0^3}\right) - r_0 \\
&k_2 = \frac{3}{5}\left(\frac{r_s^5 - r_0^5}{r_s^3 - r_0^3}\right) - \frac{3}{2}r_0\left(\frac{r_s^4 - r_0^4}{r_s^3 - r_0^3}\right) + r_0^2
\end{aligned} \quad . \tag{58}$$

At the interface where $r=r_0$, the concentration of β phase is equal to the constant of $c_{s,\beta\alpha}$, which yields,

$$c_{\mathrm{s},\beta\alpha} = c_{\mathrm{s}}(r,t)_{r=r_0} = a(t)\,. \tag{59}$$

At the surface of the particle, where $r=r_s$, the concentration is equal to the variable, $c_{s,surf}$, which yields,

$$\begin{aligned}
&c_{\mathrm{s,surf}} = c_{\mathrm{s}}(r,t)_{r=r_s} = a(t) + b(t)\cdot k_3 + d(t)\cdot k_4 \\
&k_3 = \left(r_s - r_0\right) \\
&k_4 = \left(r_s - r_0\right)^2
\end{aligned} \quad . \tag{60}$$

So the coefficients of $a(t)$, $b(t)$ and $d(t)$ can be replaced with polynomial functions of $c_{s,ave}$, $c_{s,surf}$, and r_0 , as shown in following equations,

$$\begin{aligned} a(t) &= c_{\mathrm{s},\beta\alpha} \\ b(t) &= \frac{\left(c_{\mathrm{s,surf}} - c_{\mathrm{s},\beta\alpha}\right)k_2 - \left(c_{\mathrm{s,ave}} - c_{\mathrm{s},\beta\alpha}\right)k_4}{k_2 k_3 - k_1 k_4} \\ d(t) &= \frac{\left(c_{\mathrm{s,ave}} - c_{\mathrm{s},\beta\alpha}\right)k_3 - \left(c_{\mathrm{s,surf}} - c_{\mathrm{s},\beta\alpha}\right)k_1}{k_2 k_3 - k_1 k_4} \end{aligned} \tag{61}$$

Since the ion concentrations can be substituted using $c_{s,ave}$, $c_{s,surf}$, and r_0 , the boundary condition can also be rewritten as,

$$\frac{\left(c_{\mathrm{s,surf}} - c_{\mathrm{s},\beta\alpha}\right)\left(k_2 - 2k_1\left(r_s - r_0\right)\right) - \left(c_{\mathrm{s,ave}} - c_{\mathrm{s},\beta\alpha}\right)\left(2k_3\left(r_s - r_0\right) - k_4\right)}{k_2 k_3 - k_1 k_4} = \frac{-j^{Li}}{a_s F}. \tag{62}$$

It should be noted that the control volume changes when the interface moves, but the charges in the control volume should be conserved, as shown in Figure 24.

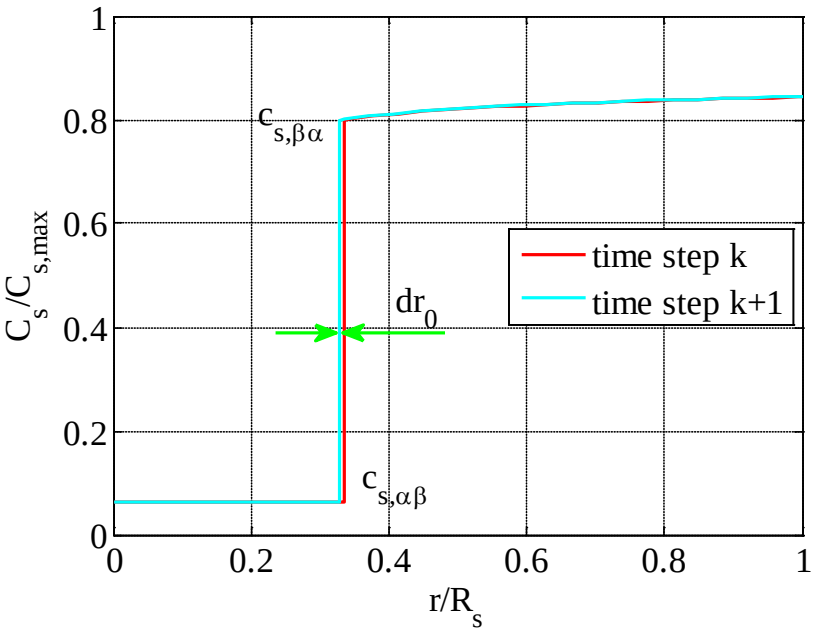

Figure 24. Mass conservation in the control volume

Based on the charge conservation, following equation can be derived using averaged ion concentration,

$$\begin{aligned} & c_{s,ave0}^{k+1}\frac{4}{3}\pi\left(r_s^3-\left(r_0^{k+1}\right)^3\right)-c_{s,ave0}^{k}\frac{4}{3}\pi\left(r_s^3-\left(r_0^{k}\right)^3\right) \\ & +c_{s,ave1}^{k+1}\frac{4}{3}\pi\left(r_0^{k+1}\right)^3-c_{s,ave1}^{k}\frac{4}{3}\pi\left(r_0^{k+1}\right)^3=\frac{-j^{Li}}{a_s F}4\pi r_s^2 \end{aligned} \quad . \tag{63}$$

So, the governing equation for the moving interface can be simplified as,

$$\begin{aligned} \left(c_{s,\beta\alpha}-c_{s,\alpha\beta}\right)\frac{\mathrm{d}r_0}{\mathrm{d}t} &= -D_{s,\beta}\frac{\left(c_{\mathrm{s,surf}}-c_{s,\beta\alpha}\right)k_2-\left(c_{\mathrm{s,ave}}-c_{s,\beta\alpha}\right)k_4}{k_2k_3-k_1k_4} \\ &+\frac{D_s}{r_0}\left(35\left(c_{\mathrm{s,surf}}-c_{\mathrm{s,ave}}\right)-8q_{\mathrm{ave}}r_0\right) \end{aligned} \quad . \tag{64}$$

For a particle with three or more layers, the governing equations for ion concentration in the outer layer and the location of the interface are as same as those of two layers, so the same order reduction methods can be applied except the boundary condition at the inner layer. Since the ion concentration at both the boundaries of the inner layer are constant, the polynomial function is defined as,

$$\begin{aligned} & c_{\mathrm{s}}(r,t)=a(t)+b(t)\cdot\left(r-\frac{r_0+r_1}{2}\right)^2 \\ & c_{\mathrm{s}}(r_1,t)=c_{\mathrm{s},\alpha\beta} \\ & c_{\mathrm{s}}(r_0,t)=c_{\mathrm{s},\alpha\beta} \end{aligned} \quad . \tag{65}$$

Similar to the process from (58) to (61), the average concentration in Layer 2 can be calculated as,

$$\frac{d}{dt}c_{\mathrm{s,ave}}-3D_{\mathrm{s}}\left(c_{\mathrm{s},\alpha\beta}-c_{\mathrm{s,ave}}\right)\frac{\left(r_0^2+r_1^2\right)\left(r_0-r_1\right)}{-r_0r_1\left(r_0^3-r_1^3\right)+\frac{3}{4}(r_0+r_1)\left(r_0^4-r_1^4\right)-\frac{3}{5}\left(r_0^5-r_1^5\right)}=0 . \tag{66}$$

And the derivatives in (47) also need to be updated,

$$c_{s,ave0}^{k+1}\frac{4}{3}\pi\left(r_s^3-\left(r_0^{k+1}\right)^3\right)-c_{s,ave0}^{k}\frac{4}{3}\pi\left(r_s^3-\left(r_0^{k}\right)^3\right)$$
$$+c_{s,ave1}^{k+1}\frac{4}{3}\pi\left(\left(r_0^{k+1}\right)^3-\left(r_1^{k+1}\right)^3\right)-c_{s,ave1}^{k}\frac{4}{3}\pi\left(\left(r_0^{k}\right)^3-\left(r_1^{k+1}\right)^3\right)=\frac{-j^{Li}}{a_s F}4\pi r_s^2 \quad (67)$$

SOC of the cell is defined as the ratio of available charge capacity ($Q_{\text{releasable}}$) to the maximum charge capacity ($Q_{\max}$), which can be calculated based on number of charges,

$$SOC=\frac{Q_{\text{releasable}}}{Q_{\max.}}\cdot 100\% \quad (68)$$

The maximum capacity and the available capacity can be calculated based on the averaged ion concentration,

$$\begin{aligned} Q_{\text{releasable}} &= \int_0^{L_-}\varepsilon_s\cdot F\cdot c_{s,\text{ave}}\cdot A\cdot dx-\varepsilon_s\cdot F\cdot c_{s,\max}\cdot Stoi_0\cdot A\cdot L \\ Q_{\max} &= \varepsilon_s F c_{s,\max}\cdot(Stoi_{100}-Stoi_0)\cdot A\cdot L \end{aligned}, \quad (69)$$

where A is the plate area of the electrode, L is the thickness of the electrode, $Stoi_{100}$ and $Stoi_0$ are the stoichiometry at the SOC of 100% and 0%, $c_{s,\max}$ is the maximum ion concentration in solid particles and $c_{s,\text{ave}}$ is the volume average ion concentration in solid particles. For a particle with m layers, $c_{s,\text{ave}}$ can be calculated as,

$$c_{s,\text{ave}}=\frac{\sum_{i=1}^{m}\left(r_{out,i}^3-r_{in,i}^3\right)c_{s,ave,i}}{R_s^3}, \quad (70)$$

where r_{out} and r_{in} are the location of ith layer's outer and inner boundary.

A ROM for ion concentrations in LFP particles during discharging are derived. The PDEs from (41) to (47) that describe ion concentrations in the FOM are replaced by ODEs of (56) to (67) using polynomial method, so the calculation time can be drastically reduced. For charging, the interface moves from outer to inner, which is the same as that of discharging. However, the outer layer is α phase, while the inner layer is β phase. Thus, the same equations can be used but with changed parameters according to the corresponding phase.

Rest of submodels for ion concentration in anode particles and the potentials are summarized in Table 6, and more details could be found in [14].

3.4 Results and analysis

A full order shrinking core model is developed at first and then reduced. Then, the reduced model is integrated into the reduced order cell model developed previously [23] that includes mass transport equation in solution phase, Ohm's law for both solution and solid phase, and the Butler Volmer equation. The integrated ROM is validated against experimental data obtained during galvanostatic discharging and charging with various current rates at constant ambient temperature of 25°C.

The experiments data is collected for coin cells made of LFP cathode and carbon anode with the equipment of PNE 20mA. The geometry of the cell and the volume fraction of each material are listed in Table 7. The rated capacity of the cell is 17.284mAh, which is measured by the following steps: fully charge at 1C, rest for 60min, fully discharge at 1C in CC mode, and rest for 60min. The discharge capacity is considered as the rated capacity.

3.4.1 Analysis of ion concentration at constant discharging current density

When a particle is fully charged, only α phase exists. After a discharging current is applied, changes of the ion concentration distribution 3.2.1 take place according three sequences as explained in section. At the beginning, particles find themselves in a state where the ion concentration is at the lowest and in only α phase. As time goes on, more ions are transported to particles and diffuse into inner parts of the particles. The transient behavior of ion concentration is plotted in Figure 25 as a function of time.

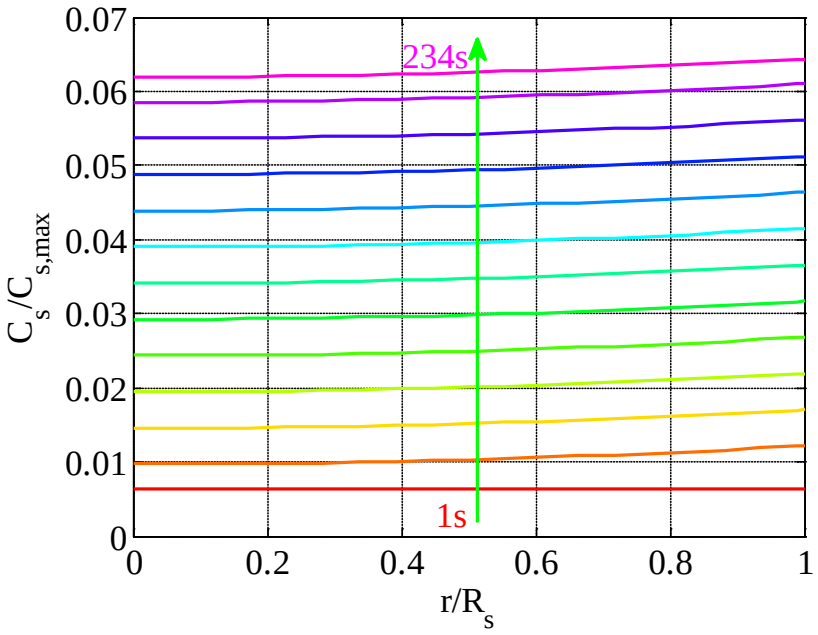

Figure 25. Ion concentration in a particle with presence of only α phase during discharging.

When the ion concentration at the surface of particles reaches the saturation value $c_{s,\alpha\beta}$, β phase is generated at the surface and continues growing while the discharging current is being applied. As a result, a two-phase is formed inside of particles, where α phase is in the core and β phase is in the shell.

With more ions inserted into particles, ion concentration continuously increases in both phases, which drives the interface between two phases moving toward the inside of the particle. This transient behavior of the ion concentration at different times is plotted in Figure 26.

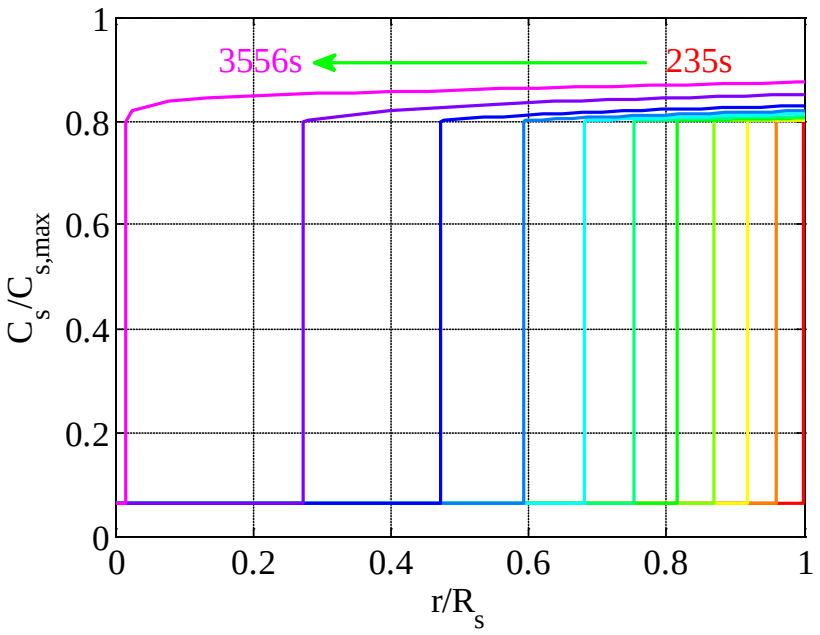

Figure 26. Ion concentration in a particle at presence of two-phase during discharging.

When the interface moves further to the center of the particle, α phase shrinks and finally disappears. Consequently, only β phase is presented in particles. With discharging continues, ion concentration increases until the ion concentration on the surface of the particle reaches its maximum limit and then the discharge stops. The ion concentration of β phase is shown in Figure 27.

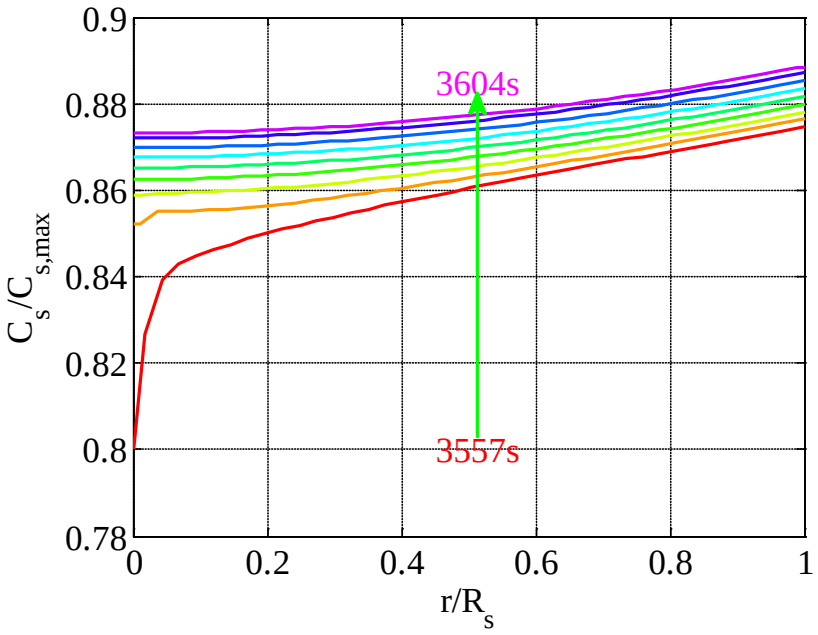

Figure 27. Ion concentration in a particle at presence of only β phases during discharging.

Ion concentration in LFP particles can be calculated using FOM. However, due to the large number of meshed grids and multiple layers, the calculation speed is not fast enough for real time application. So the FOM is reduced to a model using the method introduced in section 3.3. The accuracy and calculation time of the ROM is compared to those of FOM in this section, where constant discharging current rates, 1C, 3C, 5C, and 10C are applied to a single particle with 100% initial SOC. Average ion concentration in the particle, ion concentration at particle surface, and location of the moving interface are plotted in (a), (b), and (c) of Figure 28. The average concentration of the FOM is the exactly same as that of the ROM because of charge conservation. Likewise, the ion concentration at particle surface and generation and the movement of the interface of both models is the same except a small discrepancy in the location of the interface at the very end of discharging.

In addition, calculation time of the FOM is dramatically reduced by ROM. The number of grid points for FOM in radial direction is 20 in each layer within one particle, so the size of the matrix is 40*40 if the particle has two layers. The FOM takes around 1.05s at 3C discharging rate. The size of the matrix in the ROM is 7 for a two-layer particle. The calculation time of the ROM was 0.05s, which is 1/20 of the FOM calculation time.

After testing the accuracy and calculation time of the ROM for a single particle, the ROM is coupled with other equations in Table 4, so the performance of cells can be simulated. The results of the ROM at different load profiles are analyzed in the following sections.

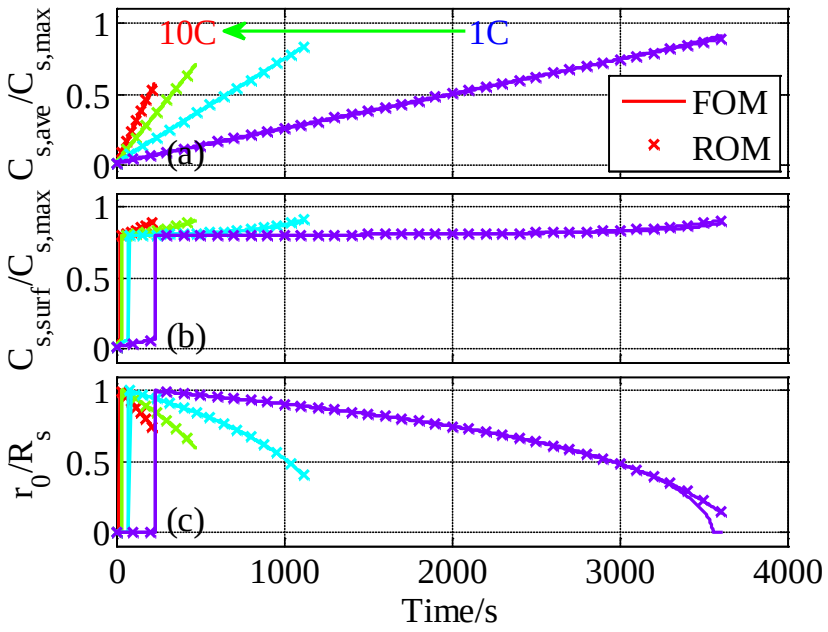

Figure 28. Comparison of ion distribution in a single particle between FOM and ROM.

3.4.2 Analysis of the ROM during discharging

In order to analyze performances of the ROM, different discharging current rates are applied as inputs to the model and terminal voltages and SOC as outputs. In addition, internal variables like ion concentrations on surface, current density, and the location of the interface between two

layers are calculated. The current rates applied are 1C, 3C, 5C, and 10C, where the initial state of the cell is set to 100% SOC.

Comparisons of simulation results and experimental results of terminal voltage are shown in Figure 29.The cell is fully charged and particles find themselves in single α phase. When discharging starts, the terminal voltage drops rapidly. This drop is dependent upon the value of α. α is the stoichiometry number that once lithium ion reaches β phase will be generated. The value is tentatively set to be 0.05 in the ROM. In the following region, the terminal voltage drops very slowly, which is caused by the two-phase transition from α phase to β phase. The difference between the value of α and β determines the length of the flat voltage that continues. At the end of discharge, the terminal voltage drops rapidly again, which is determined by β phase, and the discharge stops once the terminal voltage reaches 2.5V.

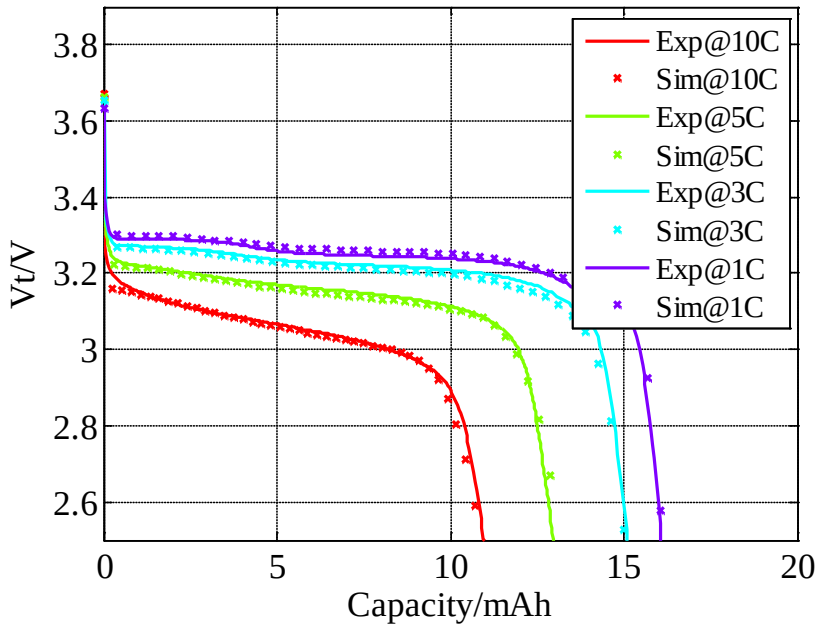

Figure 29. Comparison of terminal voltage at 1C, 3C, 5C, and 10C during discharging.

Simulation results and experimental results are plotted in Figure 30. The SOC is estimated based on the average ion concentration in the composite electrode, while the experimental value is measured based on Coulomb counting. Since the cell is discharged with a constant current rate, the measured SOC linearly decreases from 100% SOC. The estimated SOC is derived using average ion concentration calculated based on charge conservation. The simulation results can follow the experimental results with high accuracy.

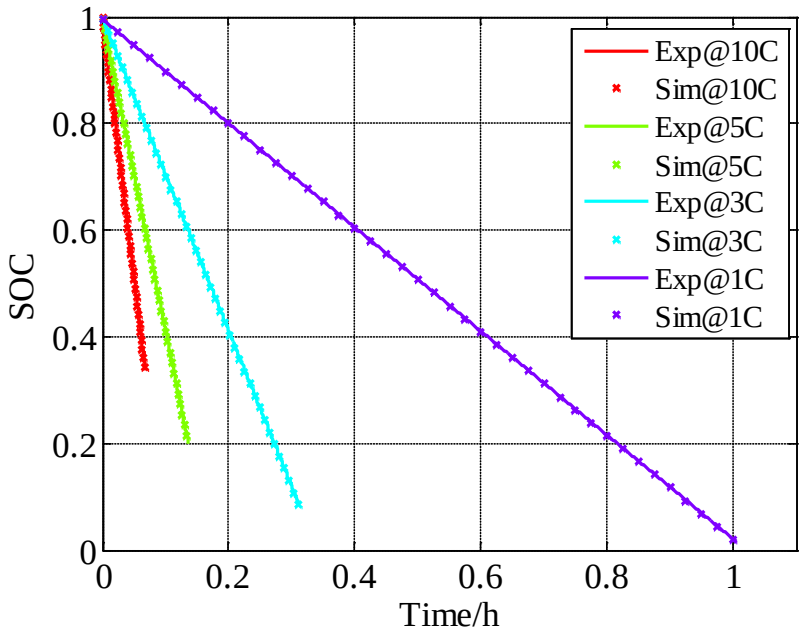

Figure 30. Comparison of SOC at 1C, 3C, 5C, and 10C during discharging.

The validated model is used to analyze the dependence of ion concentration on locations of particles. When the cell is discharged with a constant current, the current density in the particles near the separator side is high, while the current density near the current collector side is low.

The high current density decreases ion concentration on the surface of particles in the anode side. Conversely, in the cathode side, the current density in the particles near the separator is not always the highest, according to boundary conditions on the surface of the particle.

At the beginning, there exists only α phase in the cathode side, so the current density is high at the particles near the separator. As discharging continues, the ion concentration in the particles increases. When the concentration reaches $c_{s,\alpha\beta}$, β phase is generated first in those particles located near the separator. Since the diffusivity of β phase is lower than that of α phase, the ion concentration starts to increase on the surface of the particle and then the current density drops at the particle where β phase is generated. While discharging continues, the location of peak current density in the cathode moves from the particles near the separator to the particles near the current collector side, as shown in Figure 31.

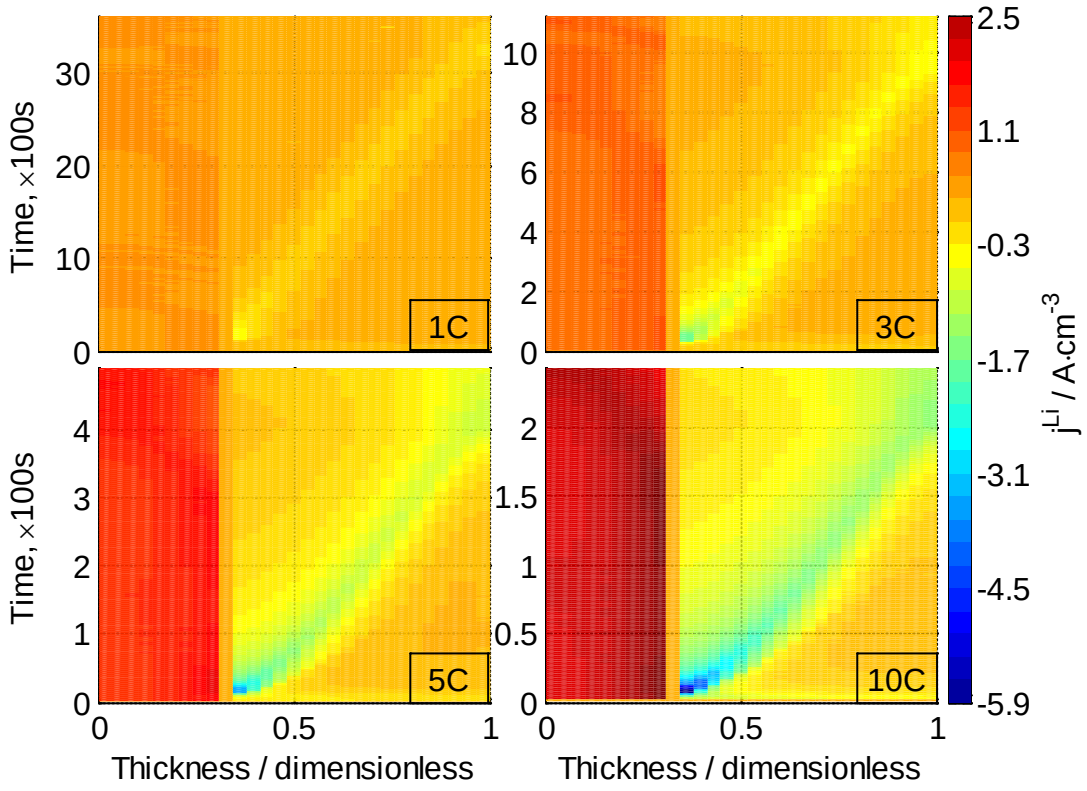

Figure 31. Current density at 1C, 3C, 5C, and 10C during discharging.

The ion concentration on the surface of the particles at different current rates is shown in Figure 32. The ion concentration in the anode side decreases during discharging. When the discharging

current is high, the concentration gradient in the thickness direction becomes large. Conversely, the ion concentration increases during discharging on the cathode side with the two-phase transition, as shown in Figure 32.

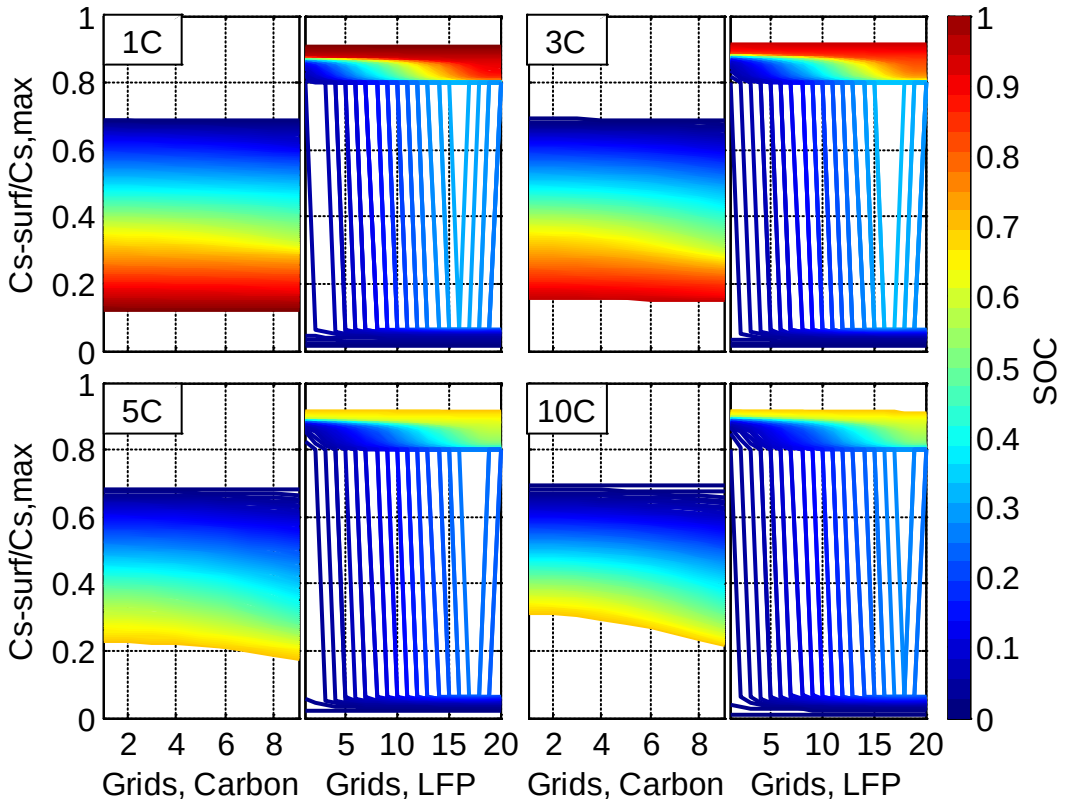

Figure 32. Simulation results of ion concentrations on the surface particles of both the anode and cathode at 1C, 3C, 5C, and 10C during discharging.

More details of the two-phase transition and the moving interface between α and β phase are shown in Figure 33. At the beginning of discharging, the value of r_0/R_s is 0, which indicates presence of only α phase. Once a new phase is generated on the surface of particle, the interface between α and β phase moves from the surface toward the center of the particle and the value of r_0/R_s changes from 1 to 0. When r_0/R_s is 0 again, only β phase is present. At low current rates like 1C, most of the particles find themselves in only β phase at the end of discharging. At high current

rate like 10C, all the particles still have two phases and as a result the discharging capacity at a high current rate is lower than that at a low current rate.

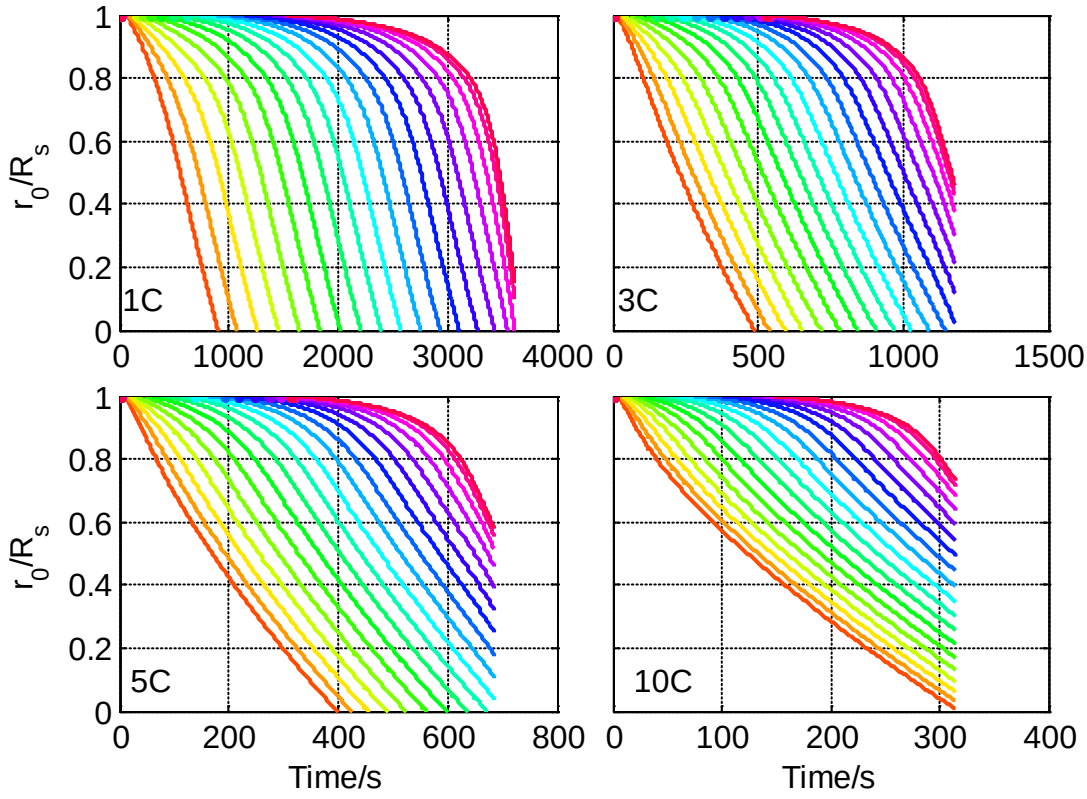

Figure 33. Simulation results of the moving interface in LFP particles at 1C, 3C, 5C, and 10C during discharging.

3.4.3 Analysis of the ROM during charging

Similar to the analysis of the ROM during discharging, the response of the ROM during charging is analyzed in terms of only terminal voltage and SOC because the others like current density, ion concentration, and location of the interface between two phases have not shown any particular differences in characteristics compared with those of discharging.

The calculated and measured terminal voltage versus capacity are plotted in Figure 34, where different currents are applied. The simulated results match pretty well with the experimental data.

The larger the current rates are, the smaller the charging capacity is. When large current is applied, both concentration overpotential and ohmic overpotential are large, so the terminal voltage during charging would get to its upper limitation early, which leads to small charging capacity.

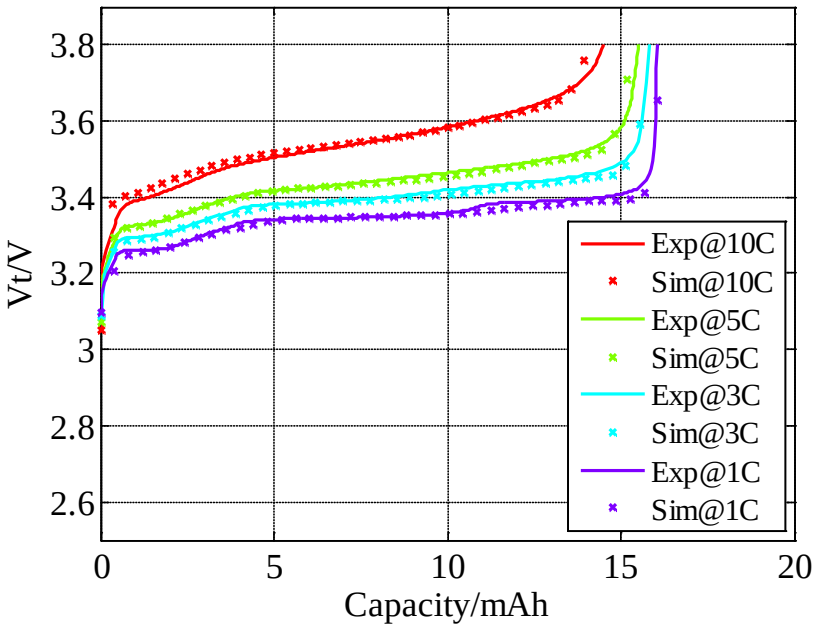

Figure 34. Comparison of terminal voltage at 1C, 3C, 5C, and 10C charging.

In addition, capacity during charging is larger than that during discharging even though the current rate is the same. During charging, α phase is formed in the shell while β phase is in the core. Since the diffusivity of α phase is better than that of β phase, the concentration gradient in the α phase is smaller than that of β phase and as a result the concentration overpotential caused by the gradient becomes small and the charging capacity is large.

SOCs at different charging currents are plotted in Figure 35. The estimated SOC using ROM matches well with the experimental data measured using Coulomb counting method.

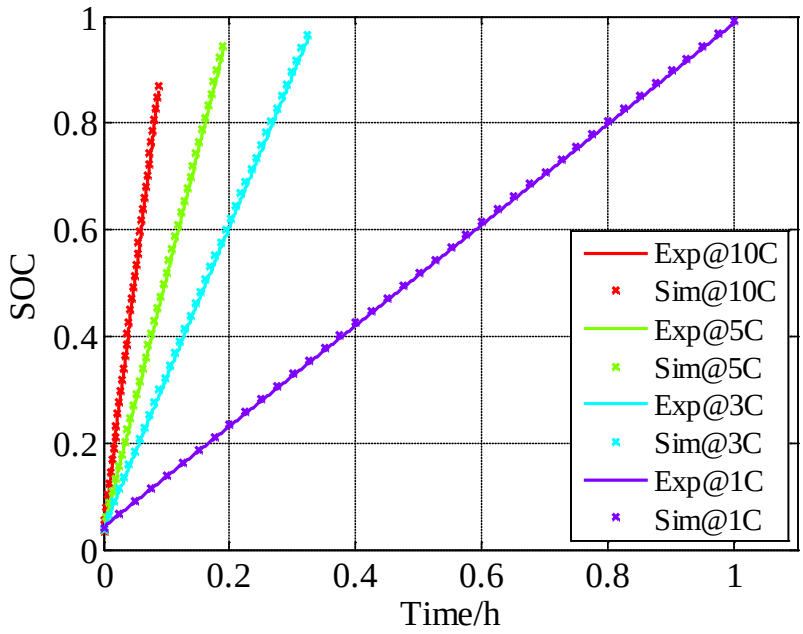

Figure 35. Comparison of SOC at 1C, 3C, 5C, and 10C during charging.

3.4.4 Analysis of the ROM during cycling

When the cell is sufficiently rested, it can be assumed that a steady state is reached, so ions within particles are evenly distributed in the solid particles, which represent a single phase. However, the distribution of the ions in LFP particles is determined by the juxtaposition of the two phases that depends on the cycling history of the cell. For example, when a cell is charged to 50% SOC from an initial 0% SOC, two phases are formed, β phase in the shell and α phase in the core, as step 1→2→3 shows in Figure 22. In contrast, when the cell is discharged to 50% SOC from 100% SOC, discharged, α phase and β phase are formed in the shell and in the core of particles, respectively, as the step 5→6→7 shows.

In addition to juxtapositions of the two phase, the number of layers is also dependent upon cycling history. The number can be different even at the same SOC When a cell is discharged from an initial state of 50% to 25% SOC, two layers can be formed in particles, β on the surface as the step 7→8 show, or three layers as step 3→9 shows.

Moreover, cycling history affects cell performance during discharging or charging. For example, the terminal voltage and change of juxtaposition are plotted in Figure 36 for the case when a cell is discharged with 3C rate from an initial state of 50% SOC. Two kinds of juxtaposition of the two phases in the particles are possible, as shown in step 3 and 7 of Figure 22, with α phase or β phase on the surface of the particles, respectively. The terminal voltage of the cell is marked with circles for steps 3→9→1, and stars for steps 7→8→1.

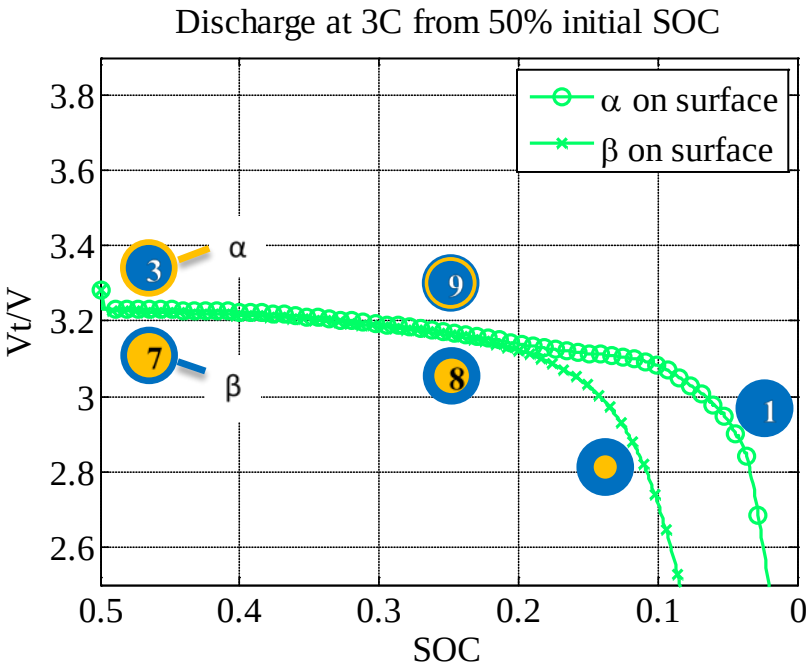

Figure 36. Juxtaposition of phases in LFP particles and the terminal voltage at 3C discharging with 50% of initial SOC and different juxtaposition of the two phases; (a) for 3→9→1, and (b) for 7→8→1

When a discharging current is applied, β phase is generated on the surface of the particles that initially have two layers as status 3, so three layers are formed in the particle, $\beta/\alpha/\beta$ from the shell to the core as status 9 shows. As the discharge continues, the layer of β phase gets enhanced and the interface between the layers moves towards the core, which leads to depletion of the layer of α phase. Finally, α phase disappears and there is only one layer of β phase left as status 1 shows, and the interface between the two layers also disappears as (a) in Figure 37 shows. Different colors are used to indicate the distances of the particles from the separator. The red to purple solid line denote the particles nearest to and farthest from the separator.

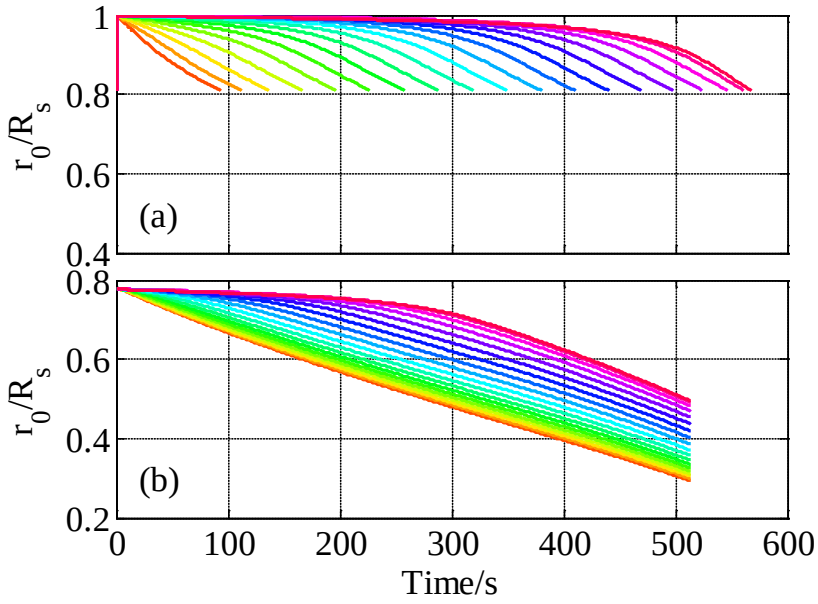

Figure 37. Location of the interface between the two phases in LFP particles at 3C discharging with 50% of initial SOC and different juxtaposition of the two phases; different colors represent particles at different locations in composite cathode. (a) for 3→9→1, and (b) for 7→8→1.

When discharge a particle with status of 7, since there is β phase on the surface, the thickness of this layer grows, and the core shrinks as status 8 shows, at the same time the interface moves

towards the core as (b) in Figure 37 shows, and there are two layers in all particles at the end of discharging. However, the total number of charges extracted from the cell with particles of status 3 is more than that of status 7, which matches with the experimental results mentioned in [46] and [45].

In contrast to the discharging process, during the charging process, the total number of charges inserted to the LFP particles of status 3 is less than that of status 7. The terminal voltage and the change of juxtaposition of the phases in LFP particles are plotted in Figure 38. The location change of the interface at different locations in the cathode is plotted in Figure 39. At the end of 3C charging from status 3, for the particles near the separator there is only one layer of α phase left, while for the particles near the current collector there are two layers left. However, charging from status 7, all of the particles reach status 5 with only one layer of α phase. This explains why more charges are inserted to particles of status 5 than that of status 3.

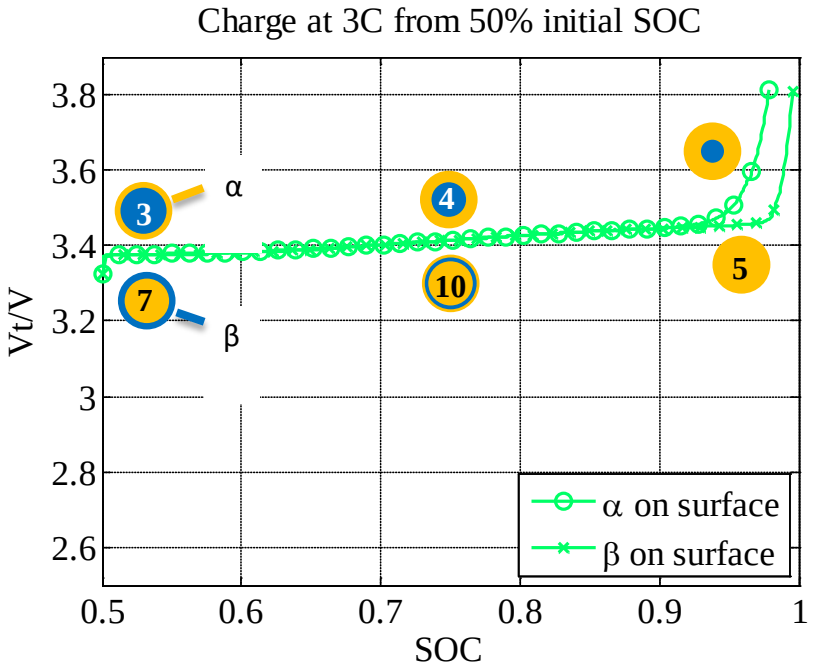

Figure 38. Juxtaposition of the phases in LFP particles and the terminal voltage at 3C charging with 50% of initial SOC and different juxtaposition of the two phases.

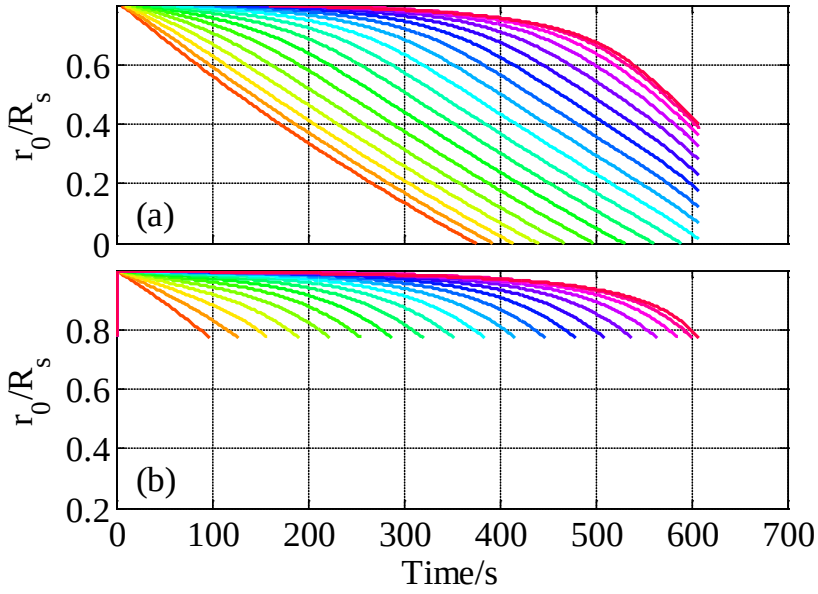

Figure 39. The location of the interface between two phases in LFP particles at 3C charging with 50% of initial SOC and different juxtaposition of the two phases; (a) for 3→4→5, and (b) for 7→10→5.

When discharging or charging a cell from a certain initial SOC, the capacity change depends on both current rate and the juxtaposition of the phases in LFP particle. Figure 40 shows the capacity change at different operating conditions. Different colors represent different initial SOCs, and circles and stars represent cells with α and β phase on the surface of LFP particles respectively. We can draw the following conclusions from the figure: during discharging there is a larger capacity change of the cell with α phase on the surface of LFP particles, while during charging there is a larger capacity if there is β phase on the surface of LFP particles; the larger the current rate is, the more severe the path dependence phenomenon is; when the initial SOC is in the range of 30% to 70%, the effect of cycling history is more obvious; the juxtaposition plays a more important role during discharging than during charging.

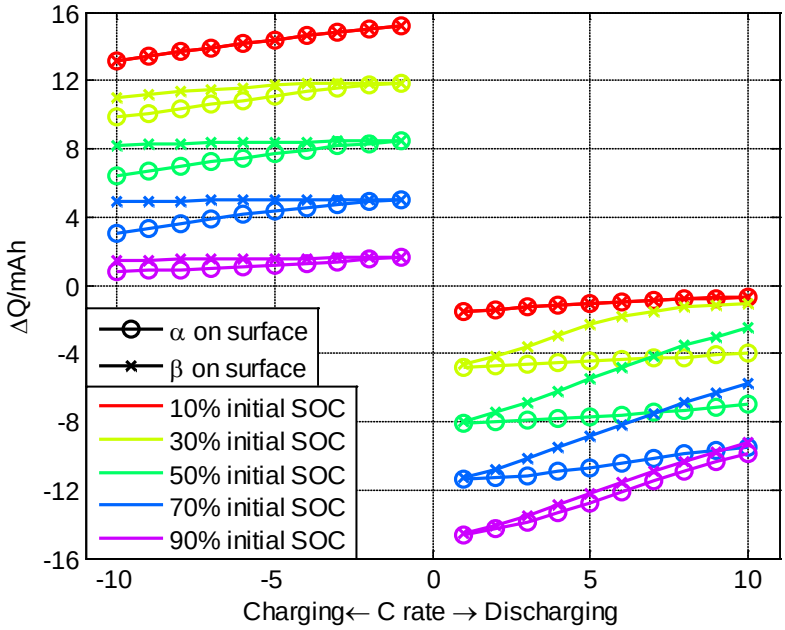

Figure 40. The available capacity depending on different current rates, initial SOC, and the juxtaposition of the two phases.

3.5 Summary

A new reduced order mathematical model for cells with LFP chemistry as cathode and carbon as anode is developed based on electrochemical principles. Particularly, the ion distribution in LFP particles is approximated by a shrinking core model that is described using diffusion equations and simplified using polynomial approximation. The model is capable of representing the three major characteristics of the battery determined by the two-phase transition taking place in LFP particles that include voltage plateau, hysteresis between charging and discharging, and path dependence.

The developed ROM is validated against experimental data of terminal voltage and SOCs during galvanostatic charging and discharging process, and then is used to analyze the major characteristics mentioned above. Major accomplishments of this work are summarized as follows:

1. The model can capture realistic behaviors of LFP cells that includes plateau, hysteresis and particularly path dependence that is otherwise not possible;
2. More available charges are observed during discharging when α phase is present in the shell at the beginning and during charging when β phase is present in the shell.
3. The path dependence is a function of current rates and SOC range. The dependence becomes severe when current rates increase or SOC ranges from 30% to 70%;
4. Performance is more affected by the cycling history during discharging than that during charging.

Chapter 4 Modeling for blended chemistry

4.1 Literature review

4.1.1 Review of models for a cell with blended cathode

Since the cathode is made of two different materials, the working mechanism of blended cells is substantially different from that made of a single material, which should be considered in modeling. Generally, behavior of two blended materials are approximated using two different sets of parameters that include particle size, ion diffusivity, conductivity, and equilibrium potential. A model using the two parameter sets has been used to analyze cell performances. Jung [53] studied effects of the different blending ratio between LMO and NMC materials for optimization of cell design. Dai [54] studied effect of blend ratio between LMO and NCA materials on stress generation during cell operation. In addition, interactions between particles that have different radii are modeled using contact resistances present between particles [55]. Similarly, cathode made of NCA and LMO is modeled considering contact resistances between various particles and conductive matrix, which shows improved prediction of terminal responses, particularly at high current rates. The model is used to analyze effects of molar fraction of LMO on energy and power [10].

The active materials used for their modeling efforts have the same intercalation mechanisms. However, the blended cathode with NMC and LFP is difficult to model because of the two-phase transition taking place in LFP particles and has not been modeled yet. In this paper we propose a

reduced order electrochemical and thermal model to simulate the performance of cells with graphite anode and NMC/LFP blended cathode. Firstly the modeling principles for two cathode materials are introduced. Secondly the equilibrium potential of the blended cathode regarding to blending ratio is analyzed. Finally we validate the ROM and analyze the effects of blending ratio on cell performance.

4.1.2 Review of SOC estimation methods

The SOC is a gauge that predicts an amount of charges stored in each electrode, which is comparable with an indicator for a fuel tank. Wrong estimation of the SOC leads to overcharge or undercharge of a battery, which causes a high rate of degradation or a low utilization of the capacity. Therefore, it is very desirable to accurately estimate the SOC regardless of operating conditions. The SOC estimation algorithm should be able to accurately handle slight variations in cell construction, operations, and attain numerical convergence, as well as calculation speed.

A review on literatures recently published unveils that SOC estimation methods can be arranged into two main categories, with or without a mathematical model. The one ‘without’ is based on direct measurement of the current and a lookup table, including: the Coulomb counting, open circuit voltage (OCV) [56], resistance and impedance [57], and quantum magnetism [58]. Methods with a model can be arranged into four subcategories including: empirical models [59], electrical equivalent circuit models (EECM) [21], and full order (FOM) and reduced order (ROM) electrochemical models [20, 36, 37]. To increase accuracy of estimation, mathematical models are usually combined with error correction techniques, such as with Kalman filter [29], adaptive extended Kalman filter [59], linear observer [30], sliding-mode observer [60], or neural network [33].

The Coulomb counting that calculates SOC by integrating the measured current over time, resulting in units of C or Ah. The Coulomb counting has several drawbacks. The initial SOC cannot be estimated by the method unless recalling charging and discharging history data. In addition, errors of the current sensors caused by offsets, drifts, and nonlinearity decrease accuracy of the method. Moreover, if the battery gets aged and the maximum capacity gets less, then the accuracy drops. Consequently, the algorithms should be able to compensate errors caused by inaccurate information of initial SOC, maximum capacity, and sensors.

The second method using the OCV is based upon a set of experimentally collected data that includes a relationship between OCV and SOC. The data is obtained by discharging battery with a low current rate along with resting periods. When the battery reaches an equilibrium state during the rest period, a corresponding SOC can be read from the values that are stored in a lookup table. Errors of the Coulomb counting can be reduced by combination with this method. However, the challenging issue is the accurate estimation of the OCV because the measured terminal voltage is different from the OCV due to overpotential that are dependent upon currents. The OCV—SOC method can predict the SOC accurately if the battery is sufficiently rested and completely relaxed.

A third method is based on the principle that impedance of a cell varies as a function of charge state [57]. Impedances of a cell are measured by the Electrochemical Impedance Spectroscopy (EIS) at different SOCs. An electric equivalent circuit model is used to represent the impedance response, whose values are extracted by fitting the response to the model. The measured data is stored in a look-up table and used for the estimation of SOC during operations. However, due to the dependence of the parameters on temperature, SOC, and current rates, it is hard to accurately measure the impedances during charging and discharging processes.

The OCV-SOC method introduced above can be further improved through an accurate estimation of the OCV using a model during operations. The models widely used are empirical models [59] or Randles' circuit models that can be of first [56] or second order [21]. This method allows for simple and easy implementation and possibility to combine with an error correction method. However, the values of circuit components of the model are not the same when the states and operating conditions are changing. In addition, the model does represent dynamics of cell characteristics, but not fully. To better consider cell physics, such as ion concentration, overpotential, and heat generation rates, high order models have been developed, such as single particle model[24] and electrochemical model [37]. The model is extended to consider temperature effects [61]. The governing equations for physics based models are the electrochemical kinetics, the charge conservation, the mass balance conservation, the energy equation and Ohm's law. Since this physical FOM is very complex and consumes a high computational time, the model is inappropriate for use in real time applications, so a reduction of the model is required. The reduction is carried out for three governing equations that describe ion concentrations in electrodes and in electrolytes and the electrochemical kinetics (the Butler-Volmer equation). As a result, the calculation time is significantly reduced while maintaining model accuracy.

However, there are still mismatch of responses between the model and the real cell. These model errors can be minimized with error correction techniques by applying advanced control theory. For the battery system, the current can be regarded as input and terminal voltage as output, ion concentration is defined as a state, which should be estimated. When a current is applied, the terminal voltage is compared with that of the model and the difference is then feed-backed to the states of the model with gains that can be optimized using EKF with respect to dynamics and suppression of noises. In this section, SOC estimation with EKF based ROM is presented, which

includes the derivation of a model for determination of the EKF algorithm, experimental validations, and analysis.

4.2 Reduced Order Modeling for cells with blended cathode

Mathematical models for NMC cells and LFP cells were developed separately in previous work [23]. The governing equations for the two models are summarized in Table 6, which include the mass transport equations in both solid and solution phase, the Ohm's law for both solid and solution phase, the Butler-Volmer equation, the energy equation, and the SOC equation that are derived using ion concentration. All the equations for the two models are same except the one to calculate ion concentration in solid particles of cathode electrode, because the ion intercalation mechanisms for NMC and LFP particles are different. In addition, two sets of parameters are employed for the two types of cells, including cell geometry, concentration, kinetic, and transport properties.

The model for cells with blended cathode is built based on combination of the two separate models, and modifications are made to treat two active cathode materials. The equations need to be modified, which are related to equilibrium potential of and ion concentration in solid particles of cathode electrode.

The total local current flow in the cathode electrode is a sum of the current flow from the two individual active materials, which is calculated using Butler-Volmer equation,

$$
\begin{aligned}
j^{\mathrm{Li}} &= j_{\mathrm{NMC}}^{\mathrm{Li}} + j_{\mathrm{LFP}}^{\mathrm{Li}} \\
j_i^{\mathrm{Li}} &= a_{\mathrm{s,i}} i_{0,\mathrm{i}} \left\{ \exp\left[\frac{\alpha_{\mathrm{a}} F}{RT} \eta_{\mathrm{i}} \right] - \exp\left[-\frac{\alpha_{\mathrm{c}} F}{RT} \eta_{\mathrm{i}} \right] \right\} \\
\eta_{\mathrm{i}} &= \phi_{\mathrm{s}} - \phi_{\mathrm{e}} - U_{\mathrm{i}} - R_{contact,i} j_i^{\mathrm{Li}}
\end{aligned}
\tag{71}
$$

where i represents active material, j^{Li} is the current density, a_s is the interfacial surface area, i_0 is the exchange current density, which is a function of ion concentration in electrolyte c_e and solid

particles c_s, α_a and α_c are the anodic and cathodic charge transfer coefficient, R is the universal gas constant, T is the temperature, and η is the overpotential defined as the potential difference between the solid Φ_s, electrolyte Φ_e and the equilibrium U, and $R_{contact,i}$ is the contact resistance between the solid particle and the conductive matrix.

Due to different particle size, the interfacial surface area of the two materials, a_s, are different, which can be calculated from $3\ \varepsilon_s/R_s$. Likewise, the surface overpotentials of the two types of particles are also different because of their different equilibrium potentials determined by the surface ion concentration. As a result, the current density used for all the basic equations in Table 6 should be replaced by the equation derived for the blended cathode.

Table 6 Summary of the governing equations for a FOM of NMC and LFP cells

Equation description	Equation for NMC	Equation for LFP
Ion concentration in the solid phase	$\frac{\partial c_s}{\partial t}=\frac{D_s}{r^2}\frac{\partial}{\partial r}\left(r^2\frac{\partial c_s}{\partial r}\right)$ $\frac{1}{r}\frac{\partial c_s}{\partial r}\Big\vert_{r=0}=0$ $D_s\frac{\partial c_s}{\partial r}\Big\vert_{r=R_s}=\frac{-j^{Li}}{a_s F}$	$\frac{\partial c_s}{\partial t}=\frac{D_{s,\beta}}{r^2}\frac{\partial}{\partial r}\left(r^2\frac{\partial c_s}{\partial r}\right);\ D_{s,\beta}\frac{\partial c_s}{\partial r}\Big\vert_{r=r_1}=0$ $\frac{\partial c_s}{\partial t}=\frac{D_{s,\alpha}}{r^2}\frac{\partial}{\partial r}\left(r^2\frac{\partial c_s}{\partial r}\right);\ D_{s,\alpha}\frac{\partial c_s}{\partial r}\Big\vert_{r=R_s}=\frac{-j^{Li}}{a_s F}$ $\left(c_{s,\alpha\beta}-c_{s,\beta\alpha}\right)\frac{\mathrm{d}r_0}{\mathrm{d}t}=D_{s,\beta}\frac{\partial c_{s,\beta}}{\partial r}\Big\vert_{r=r_0}-D_{s,\alpha}\frac{\partial c_{s,\alpha}}{\partial r}\Big\vert_{r=r_0}$
Ion concentration in the solution phase	$\frac{\partial(\varepsilon_e c_e)}{\partial t}=\frac{\partial}{\partial x}\left(D_e^{\mathrm{eff}}\frac{\partial}{\partial x}c_e\right)+\frac{1-t_+^0}{F}j^{\mathrm{Li}}$ $\frac{\partial c_e}{\partial t}\Big\vert_{x=0}=\frac{\partial c_e}{\partial t}\Big\vert_{x=L}=0$	
Ohm's law in the solid phase	$\frac{\partial}{\partial x}\left(\sigma^{\mathrm{eff}}\frac{\partial}{\partial x}\phi_s\right)-j^{\mathrm{Li}}=0$ $-\sigma^{\mathrm{eff}}\frac{\partial}{\partial x}\phi_s\Big\vert_{x=0}=-\sigma^{\mathrm{eff}}\frac{\partial}{\partial x}\phi_s\Big\vert_{x=L}=\frac{I}{A};\ \frac{\partial}{\partial x}\phi_s\Big\vert_{x=L_-}=\frac{\partial}{\partial x}\phi_s\Big\vert_{x=L_-+L_{\mathrm{sep}}}=0$	
Ohm's law in the solution phase	$\frac{\partial}{\partial x}\left(\kappa^{\mathrm{eff}}\frac{\partial}{\partial x}\phi_e\right)+\frac{\partial}{\partial x}\left(\kappa_D^{\mathrm{eff}}\frac{\partial}{\partial x}\ln c_e\right)+j^{\mathrm{Li}}=0$ $\frac{\partial}{\partial x}\phi_e\Big\vert_{x=0}=\frac{\partial}{\partial x}\phi_e\Big\vert_{x=L}=0$	
Butler-Volmer equation	$j^{\mathrm{Li}}=a_s i_0\left\{\exp\left[\frac{\alpha_a F}{RT}(\eta-\eta_{\mathrm{SEI}})\right]-\exp\left[-\frac{\alpha_c F}{RT}(\eta-\eta_{\mathrm{SEI}})\right]\right\}$ $\eta=\phi_s-\phi_e-U$	
Energy equation	$\rho C_p\frac{dT}{dt}=Q_{\mathrm{gen}}-q$ $Q_{\mathrm{gen.}}=\frac{I}{V}(U_{\mathrm{OCV}}-V_T-T\cdot\frac{\partial U_{\mathrm{OCV}}}{\partial T})$ $q=\frac{h}{d}(T-T_{\mathrm{amb}})$	
SOC definition	$SOC=\left[\frac{1}{L_-}\int_0^{L_-}\frac{(c_{s,\mathrm{ave}}-c_{s,\max}\cdot Stio0)}{c_{s,\max}\cdot(Stoi100-Stoi0)}\cdot dx\right]\cdot 100\%$	

In addition, the effective conductivity of the blended cathode is a sum of individual conductivity reflecting the volume fraction of the material,

$$\sigma^{\text{eff}} = \sum_{i=1}^{n} \sigma_{\text{i}} \cdot \varepsilon_{s,\text{i}} \tag{72}$$

Similar to the SOC definition for cells with a single cathode material mentioned in Table 6, a new equation for SOC is derived based on the principle of charge conservation considering difference in volume fraction, stoichiometry number, and maximum ion concentration of each active material,

$$SOC = 100\% \frac{1}{L_+} \cdot \int_0^{L_+} \frac{\sum_{i=1}^{n} \varepsilon_s^{\text{i}} \cdot (c_{\text{s,ave}}^{\text{i}} - c_{\text{s,max}}^{\text{i}} \cdot Stio0_0^{\text{i}})}{\sum_{i=1}^{n} \varepsilon_s^{\text{i}} \cdot c_{\text{s,max}}^{\text{i}} \cdot (Stio0_{100}^{\text{i}} - Stio0_0^{\text{i}})} \cdot dx \,. \tag{73}$$

The energy equation in Table 6 is also updated to calculate heat generation rate in blended cathode, which considers current and overpotential of each active material,

$$Q_{\text{gen.}} = \sum_{i=1}^{n} \frac{I_{\text{i}}}{V} \left(U_{\text{OCV,i}} - V_{\text{T}} - T \cdot \frac{\partial U_{\text{OCV,i}}}{\partial T} \right) \cdot \tag{74}$$

The governing equations above include partial differential equations (PDE) that can be discretized and solved numerically. However, the computational time of the FOM based on the PDEs increases exponentially with increased number of equations. By contrast, the hardware currently being used for BMS has a limited performance, so the FOM cannot be implemented. Thus, the model order is further reduced, which includes ion concentrations in both the electrode and the electrolyte, potentials, and kinetics. The reduction of the ion concentration in the electrode and electrolyte is accomplished using the polynomial approach and the state space method, while potentials and electrochemical kinetics are reduced by linearization. In addition, the energy equation is used to calculate the heat generation during cell operation, on which the diffusion coefficients are dependent. Details can be found in the previous paper. The results show that the

calculation time of the ROM is approximately one fifteenth of that of the FOM, while the accuracy can be maintained.

4.3 Equilibrium potential

The equilibrium potential is dependent upon lithium ion concentration in solid particles and expressed as a function of stoichiometric number. Below are the equilibrium potentials for anode and cathode materials that include graphite, NMC and LFP, as shown in (75) and plotted in Figure 41.

$$U_{equ,i} = f_i(x_i), \text{where } i = \text{Li}_x\text{C, NMC and LFP}$$
$$x_i = \frac{c_{s,i}}{c_{s,\max,i}} \tag{75}$$

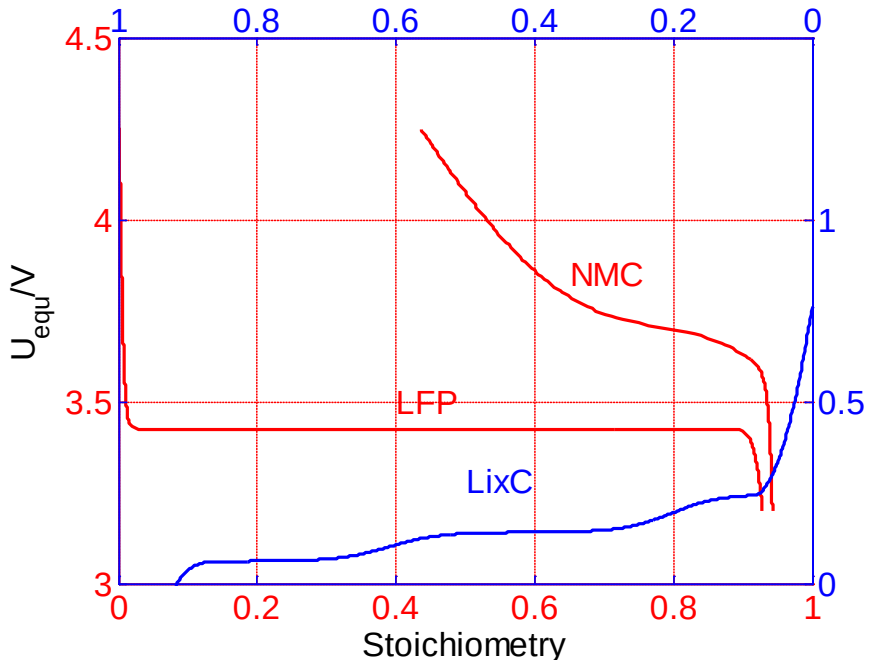

Figure 41 Equilibrium potential of pure active materials including NMC, LFP, and Li_xC.

SOC of each material as well as its capacity can be expressed as a function of stoichiometric number, as shown in (76),

$$\begin{aligned} SOC_i &= \frac{x_i - Stoi_{0,i}}{Stoi_{100,i} - Stoi_{0,i}} \\ Capacity_i &= (1 - SOC_i) \cdot Capacity_{\max,i} \end{aligned} \quad , \tag{76}$$

where the maximum capacity density of NMC and LFP is 157 and 149.6mAh/g, respectively.

Based on the two equations above, the relationship between capacity and equilibrium potential for a single active material is derived, as the red and purple curves showing in Figure 42. Using NMC allows for a high operating voltage, but a rapid voltage drop occurs at 3.6V during discharging. Conversely, the equilibrium potential of LFP is around 3.425V that is relatively low and constant for most of operating ranges. However, the outputting power is still high even at the end of discharge.

For a cathode made of *n* types of materials, its resulting equilibrium potential is obtained from the equations above using characteristics and the blending ratio of each material. Under the assumption that the *n* types of electrode particles are evenly mixed and in contact to each other, the equilibrium potential of all the particles should be the same at any given steady states. As a result, the stoichiometry of each material can be calculated by the inverse function of (75), $x_i = f_i^{-1}(U_{equ,i})$ at any given U_{equ} and then the SOC and capacity of each material can be obtained using equation (76). In addition, the capacity of the blended cathode as well as SOC at a given blending ratio can be calculated as following,

$$\begin{aligned} Capacity_{cell} &= \sum_{i=1}^{n} Capacity_i \cdot Ratio_i \\ SOC_{cell} &= 1 - \frac{Capacity_{cell}}{Capacity_{cell,\max}} \end{aligned} \quad . \tag{77}$$

Based on the relationship above, OCV and capacity of a cathode composed of NMC and LFP as a function of its blending ratio are plotted in Figure 42. Different colors represent different mass

ratio between NMC and LFP. Likewise, an equilibrium potential of an anode made of multiple active materials can be calculated.

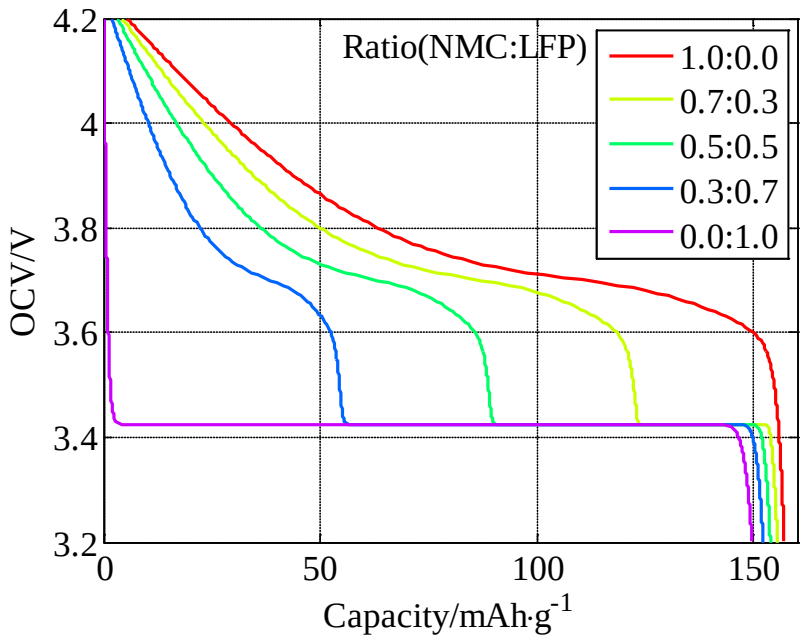

Figure 42 Equilibrium potential of NMC/LFP blended cathode with different mass ratios of 1:0, 7:3, 5:5, 3:7, and 0:1.

Once the equilibrium potentials of both cathode and anode are known, the Open Circuit Voltage (OCV) of a cell is given by the difference between the equilibrium potential of cathode and anode and can also be measured experimentally. The cells used for this study have a graphite anode and a cathode composed of 70% NMC and 30% LFP. On one hand, measurement of the OCV of the cells is carried out using voltage relaxation method. The method starts with an initial state where the battery is fully charged and correspondingly SOC is 100%. Then, the battery is discharged at a 0.1C rate for 1 min. and then keeps open circuit for 15 min. for the cell to be sufficiently relaxed. After the relaxation, the measured terminal voltage is considered to be the OCV at that state. At the same time, SOC is estimated by the Coulomb counting method. This

process is repeated until the terminal voltage reaches the cutoff voltage. The measured data of the OCV are plotted with cyan stars in Figure 43. On the other hand, based on the calculation method above, a predicted OCV from the potential of cathode (yellow solid line) and anode (blue solid line) is plotted and compared with that measured experimentally. The comparison shows relatively good match, so the same method can be also used to calculate the equilibrium potential of a cathode or anode composed of multiple active materials with different blending ratio.

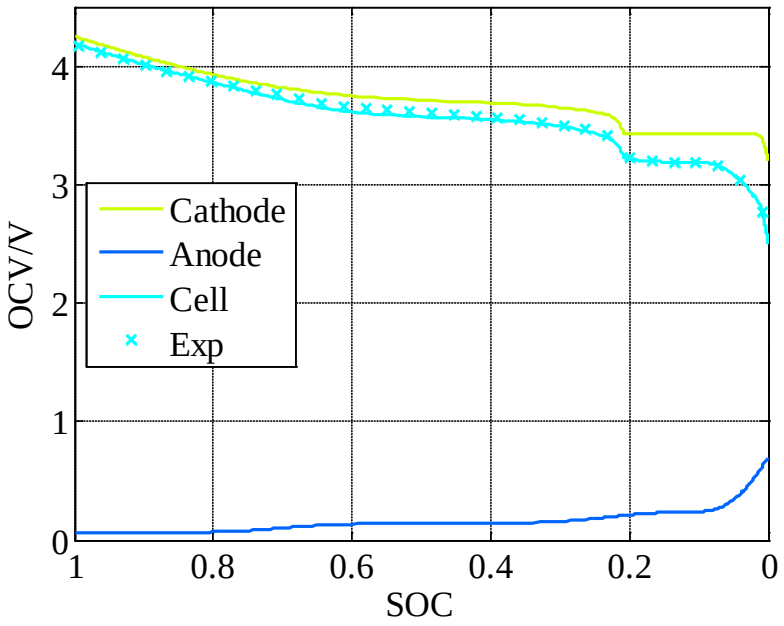

Figure 43 Calculated and measured equilibrium potential of NMC/LFP blended cathode with mass ratio of 7:3.

4.4 Results and analysis of the blended model

The ROM developed is validated experimentally and ion concentrations in each active material are analyzed. Key specifications of the cell used for the experiments are as follows;

- Materials: Cathode; NMC and LFP, Anode; Carbon, ; Electrolyte; organic material, and separator; PE/PP/PE

- The nominal capacity: 41Ah
- Operation range of the terminal voltage: 2.5V to 4.2V. 0% SOC to 100% SOC correspond to 2.5V and 4.2V at a cutoff current of 2.05A, respectively.

A test station is constructed to cycle cells and measure terminal voltage, current and temperature. The cell is placed in a calorimeter in order to keep the cell temperature constant, at the same time, heat generation rate can be measured. The temperature of the cell is the average measurements of three thermal couples placed on the surface of the cell

Validation of the ROM is performed under following operation conditions, where cells are charged at various current rates of CC/CV mode and discharged at various current rates of CC mode. The ambient temperature ranges is from 10 to 60°C. The responses of the ROM are compared with the experimental data collected with the test station, which includes terminal voltage, SOC, and temperature. The values of the parameters of the model are listed in Table 7.

Table 7 List of model parameters (a: Manufacture; b: validation; c: estimated.)

Parameter	Negative electrode	Separator	Positive electrode		unit	
			NMC	LFP		
Electrode plate area, A	23675		22290		cm^2	a
Thickness, δ	$100*10^{-4}$	$25*10^{-4}$	$135*10^{-4}$		cm	a
Particle radius, R_s	$8.5*10^{-4}$		$3.45*10^{-4}$	$5.5*10^{-4}$	cm	a
Active material volume fraction, ε_s	0.655		0.432	0.258		a
Porosity, ε_e	0.32	0.5	0.28			a
Average electrolyte concentration, c_e	0.0123	0.0123	0.0123		$mol \cdot cm^{-3}$	a
Maximum solid phase concentration, $c_{s,max}$	0.012		0.015	0.007	$mol \cdot cm^{-3}$	c
Diffusion coefficient in solid, D_s	$3.2*10^{-10}$		$2.22*10^{-9}$	$1.3*10^{-9}$	$cm^2 \cdot s^{-1}$	b
Diffusion coefficient in electrolyte, D_e	$2.60*10^{-6}$	$2.60*10^{-6}$	$2.60*10^{-6}$			b
Limitation concentration ($c_{s,\alpha\beta}$/ $c_{s,max}$)			0.02	0.85		b
Stoichiometry at 0% SOC, $Stoi_0$	0.01		0.9427	0.9284		b

Stoichiometry at 100% SOC, $Stoi_{100}$	0.87	0.4358	0.0012		b
Contact resistance, $R_{contact}$	30	400	300	Ω cm^2	b
Equilibrium potential of NMC	$3.4245+0.85\cdot\exp(-400\cdot y^{1.3})-17\cdot\exp(-0.98\cdot y^{-14})$; $y= c_{s,surf}/ c_{s,max}$				a,b
Equilibrium potential of LFP	$91.05\cdot y^6-361.4\cdot y^5+561.9\cdot y^4-438.3\cdot y^3+181.4\cdot y^2-43.02\cdot y+5872-5863\cdot\exp(5.601\cdot y^{193.3})+0.1$; $y= c_{s,surf}/ c_{s,max}$				a,b
Equilibrium potential of Li_xC	$(0.1011-0.04\cdot\tanh(13.76\cdot x-8.4))\cdot(x<=1)-252.707\cdot(x-0.854)^3\cdot(x>0.854 \& x<=1)+(0.0523-0.05275\cdot\tanh(14.05\cdot x-0.856))\cdot(x<=0.4)+(71.43\cdot(x-0.085)^2)\cdot(x<=0.085)$; $x= c_{s,surf}/ c_{s,max}$				a,b

4.4.1 Response of the ROM during discharging at 25°C

Three constant discharging current rates of 1C, 2C, and 2.5C are applied to validate the ROM, where an initial SOC is needed as an input parameter. Output variables of the ROM includes the terminal voltage, SOC, current density, heat generation rate and ion concentration. The initial SOC value for the cell is set to be100%.

The load current profile, terminal voltage and SOC during discharging as a function of time are plotted in Figure 44, Figure 45 and Figure 46, where solid lines and stars represent experimental data and simulation results, respectively. The terminal voltage suddenly drops at the beginning when a step discharging current is applied and then decreases according to a characteristic that firstly follows the characteristic of NMC and finally LFP cells. As expected, the SOC decreases linearly, which can be excellently predicted by the ROM. Analysis of discharging processes in the two different chemistries using the ROM at 1C rate reveals that discharging process takes place in the NMC dominantly until a certain SOC is reached and then in LFP, as shown in Figure 46, where the blue stars dashed line and dash dot represent the SOC of the cathode, NMC, and LFP,

respectively. More details of the contribution of NMC and LFP are show in Figure 47. Once discharge current is applied, NMC becomes the major contributor for change of the SOC, while LFP remains almost the same as its initial value, until SOC reaches 30%. When SOC reaches a value around 30%, charges inserted into LFP particles begin to increase and the SOC of LFP drops dramatically until the end of discharge, while the SOC change of NMC becomes much slower. This different discharging behavior of the two materials is caused by the nonlinear dependency of the equilibrium potentials upon stoichiometry number. In fact, the ratio of SOC changing rates of two materials is reversely proportional to that of their equilibrium potentials changing rates. As shown in Figure 41, for the range of high SOC (low stoichiometry), the equilibrium potential slope of LFP is much higher than that of NMC. As a result the change of SOC in NMC is faster than that in LFP. Likewise, the change of SOC in NMC is slower than that in LFP for a low range of SOC. In addition, different reaction rates of the two materials are another factor that affects not only SOC of the two materials, but also the terminal voltage during discharging process.

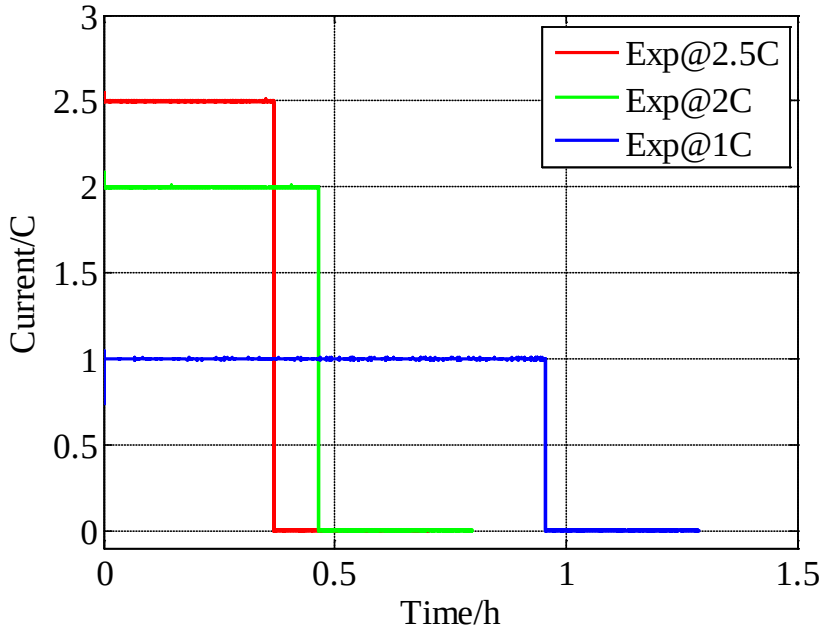

Figure 44. Load profile at 1C, 2C, and 2.5C during discharging at 25°C.

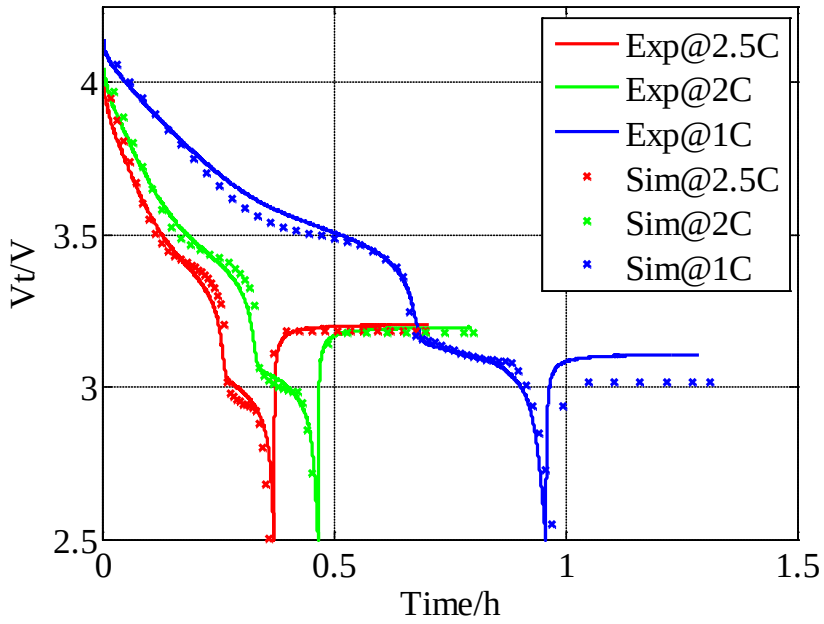

Figure 45. Comparison of terminal voltage at 1C, 2C, and 2.5C during discharging at 25°C.

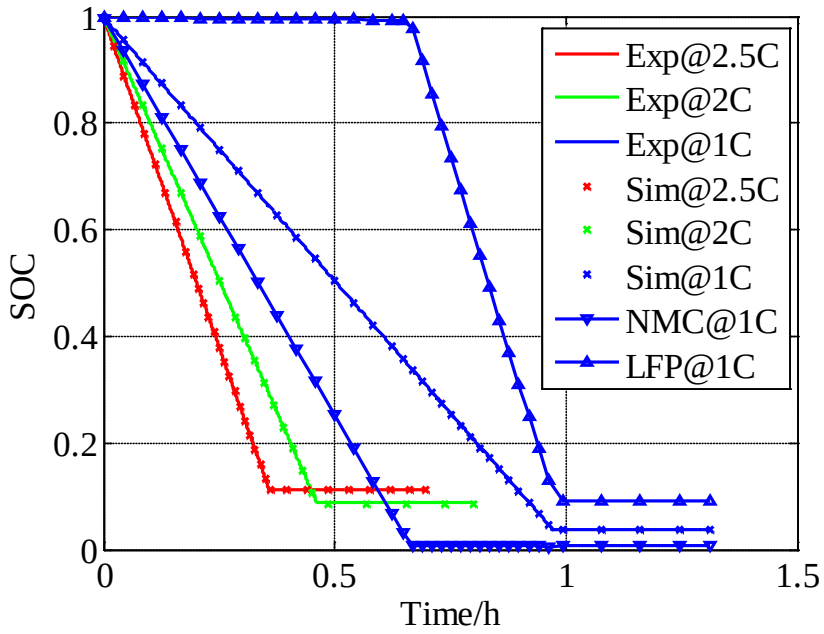

Figure 46. Comparison of SOC at 1C, 2C, and 2.5C during discharging at 25°C.

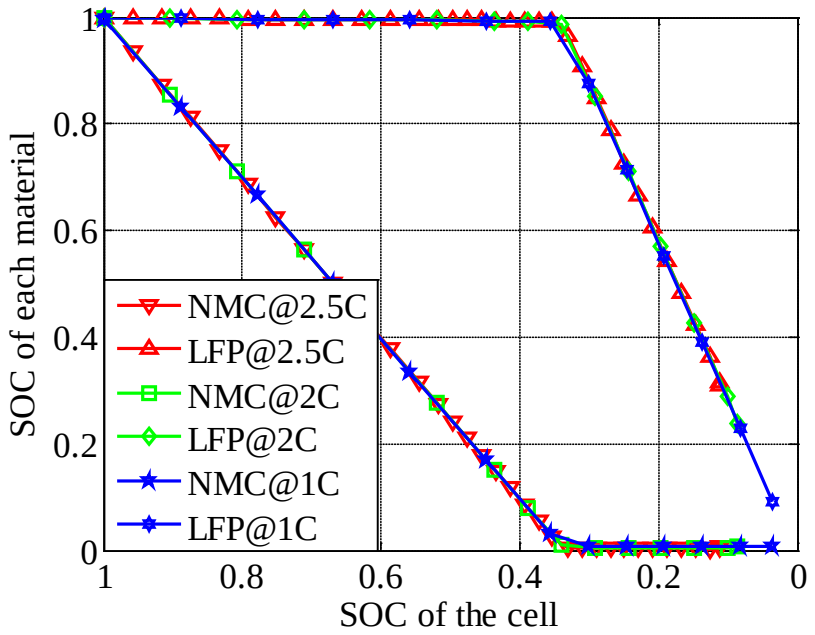

Figure 47. SOC of each active material in cathode at 1C, 2C, and 2.5C during discharging at 25°C.

When the cell is discharged with a constant current of 1C rate, there is only α phase inside of LFP particles, and the terminal voltage continuously drops until around 3.2V, where the plateau begins. LFP particles find themselves in the two-phase region. The starting time of the plateau found in Figure 45 is around 0.7h, which matches well with the simulation results of ion concentration on the surface of the LFP particles, as shown in (a) of Figure 48. At around 0.7h, β phase starts to form on the surface of the LFP particles, and then the interface between the two phases is moving toward the center of particles with discharge going on, until the terminal voltage reaches 2.5V. The generation and the movement of the interface in LFP particles are shown in (b) of Figure 48. Before 0.7h, there is only α phase inside of the particle, so the location of the interface r/Rs is 0. Once β phase starts to be generated, the value of r/Rs becomes 1 and then continues to decrease until the discharging process stops.

More details of the ion concentration in the particles of both negative and positive composite electrodes during 2C discharging are plotted in Figure 49. The ion concentration on the surface of Li_xC, NMC, and LFP particles are shown from left to right. During discharging process, ion concentration decreases in negative electrode and at the same time increases in positive electrode. Note that there are two regions in the plot of LFP, the lower concentration implies there is only single α phase inside of LFP particles, and the high concentration range implies the generation and growth of β phase in the LFP particles.

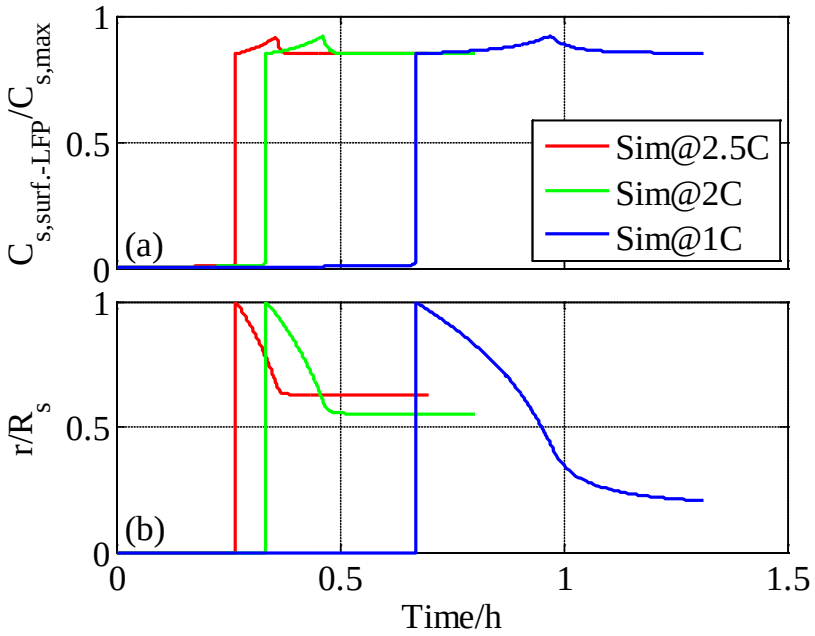

Figure 48. Ion concentration on the surface of LFP particles and the location of the interface between α and β phase inside of LFP particles at 1C, 2C, and 2.5C during discharging at 25°C.

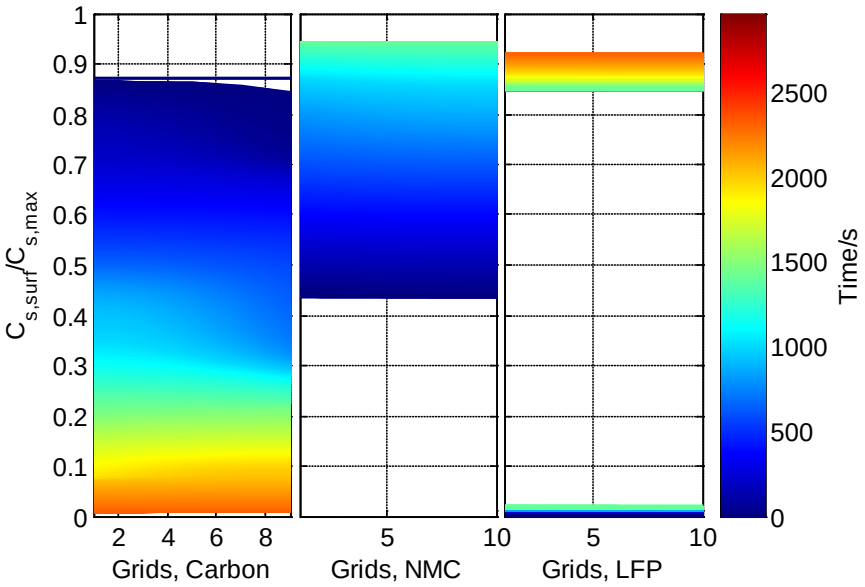

Figure 49. Simulation results of ion concentration on the surface particles of both the anode and cathode at 2C during discharging at 25°C.

Contribution of two active materials in the cathode electrode to the total current is analyzed with 1C rate during discharge. The current density produced from NMC and LFP particles during discharging are plotted in stars and circles in Figure 50. Similar to the analysis of SOC, NMC produces high current, while LFP does low current when discharging process starts. When the voltage drops below 3.2V, LFP actively produces high current while the current from NMC suddenly drops to a very small value near 0 until the end of discharge process.

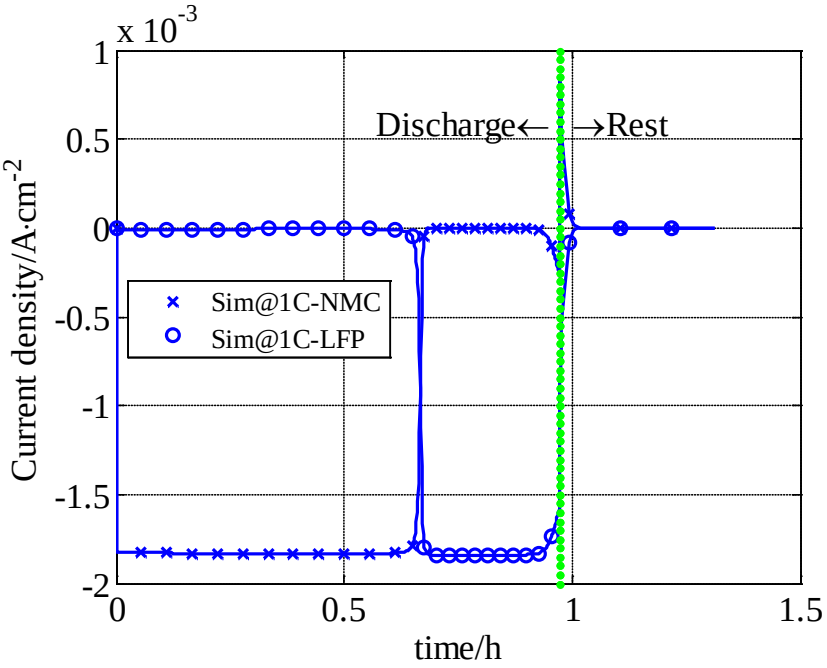

Figure 50. Current density from NMC and LFP particles at 1C during discharging at 25°C.

The current fraction from NMC at different current rates are plotted in Figure 51. A sudden drop of the current from NMC is observed for all cases, which is directly related to the sudden drop of the terminal voltage, as shown in Figure 45. In fact, active participation of the two different materials on cathode in intercalation or deintercalation processes depends upon the equilibrium potential of two materials.

If the potentials at a given SOC on the surface of both particles are greater than around 3.425V given by LFP potential, then NMC is actively participating in intercalation process. Otherwise, LFP is actively participating in the process. Consequently, the current fraction from LFP is small and almost zero at high SOC range, while the current fraction from NMC is small, but larger than zero at low SOC. Particularly, the current fraction from NMC tends to increase at high current rates, when the terminal voltage is approaching to 2.5V. Initial conditions are that SOC is 100% and ions in both NMC and LFP particles are evenly distributed. When a discharging current is

applied, ion concentration gradient within NMC particles is formed in radial and through-the-plane direction. The gradient of ion concentration in NMC particles continuously grows until LFP particles dominantly become in charge of main reaction for intercalation. Then, the gradient becomes small and as a result the overpotential decreases because of diffusion, which results in more ions accepted by NMC particles. The larger the current is applied, the larger becomes the concentration overpotential, which leads to a high ion acceptance by NMC particles at low SOC range.

Capacity of each material as a function of current rates is calculated with the ROM based on integration of currents and plotted in Figure 52, where green and cyan bar represent the capacity of NMC and LFP, respectively. Generally the capacity of the active material decreases when current increases, because a high current induces high ohmic and concentration overpotential. However, the plot shows that the capacity of NMC remains almost the same regardless of different current rates, while the capacity of LFP depends upon current rates, which implies NMC can be better utilized when blending with LFP. Therefore, the rate capability of blended cells can be improved compared to that of cells with a single cathode material.

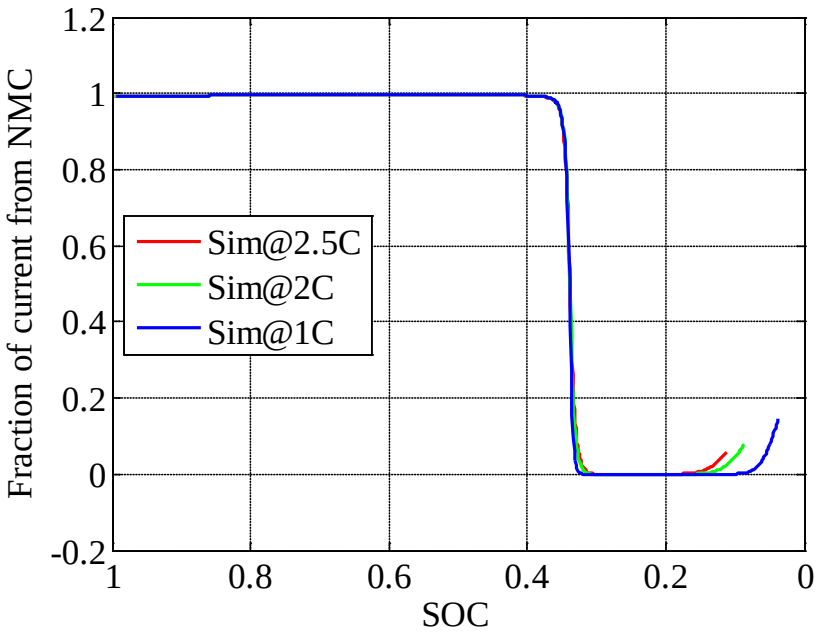

Figure 51. Current fraction of NMC particles at 1C, 2C, and 2.5C rate during discharging at 25°C.

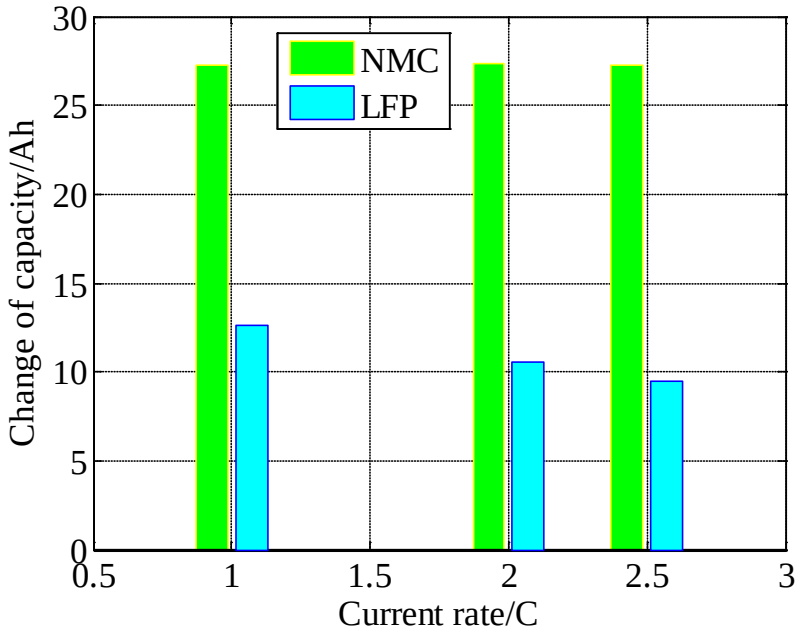

Figure 52. Capacity change of NMC and LFP particles at 1C, 2C, and 2.5C rate during discharging at 25°C.

Discharging process stops for all three cases when the terminal voltage reaches 2.5V and then cells are rested for 1200s long. When the discharging current is interrupted, no current flows from anode to cathode. However, there are ionic currents flowing between particles until an equilibrium state is reached. As shown in the right part of Figure 50, current of NMC is positive, while that of LFP is negative, which implies a current flow from LFP particles to NMC particles. During the relaxation, the potentials on the surfaces of all particles in anode or cathode become equivalent levels and subsequently the terminal voltage reach a steady state as shown in Figure 43. Hence, the ions are evenly distributed in carbon and NMC particles, the interface inside of LFP particles stops moving as shown in Figure 48.

The terminal voltage during relaxation matches well with experimental data at 2.5C and 2C during discharging, while a slight discrepancy at 1C is observed. The total discharging time of simulation is longer than that of experiment, which leads to lower SOC and lower OCV of the simulation result.

4.4.2 Response of the ROM during charging at 25°C

Likewise, the charging behavior of the blended cell is analyzed using the ROM under different CC and CV charging conditions. Simulated terminal voltage is compared with experimental data, as shown in Figure 54 and Figure 55. In contrast to discharge, when a charging process starts, LFP particles release charges at the first, while NMC particles do not participate at the first moment, which are more obvious in analysis of SOC of the two particles as shown in Figure 55.

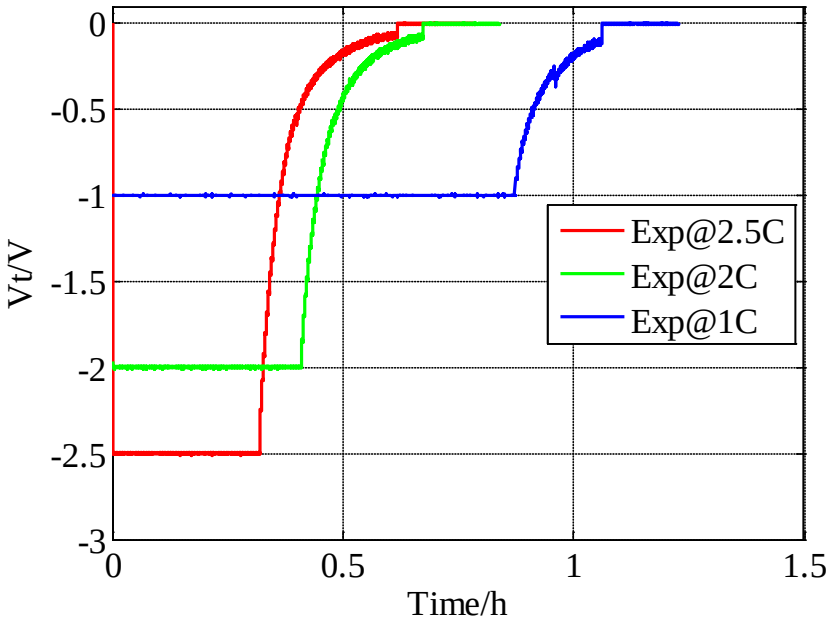

Figure 53. Load profile at 1C, 2C, and 2.5C during charging at 25°C.

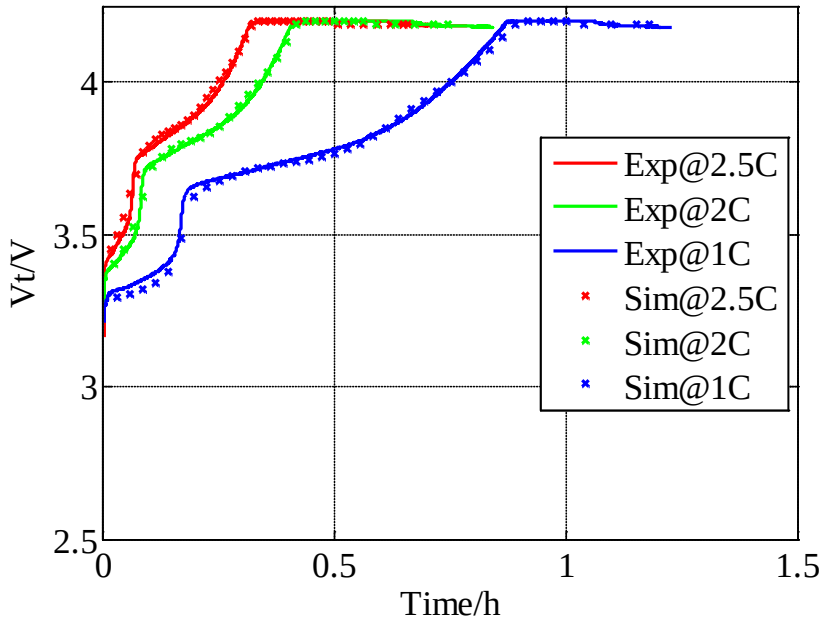

Figure 54. Comparison of terminal voltage at 1C, 2C, and 2.5C during charging at 25°C.

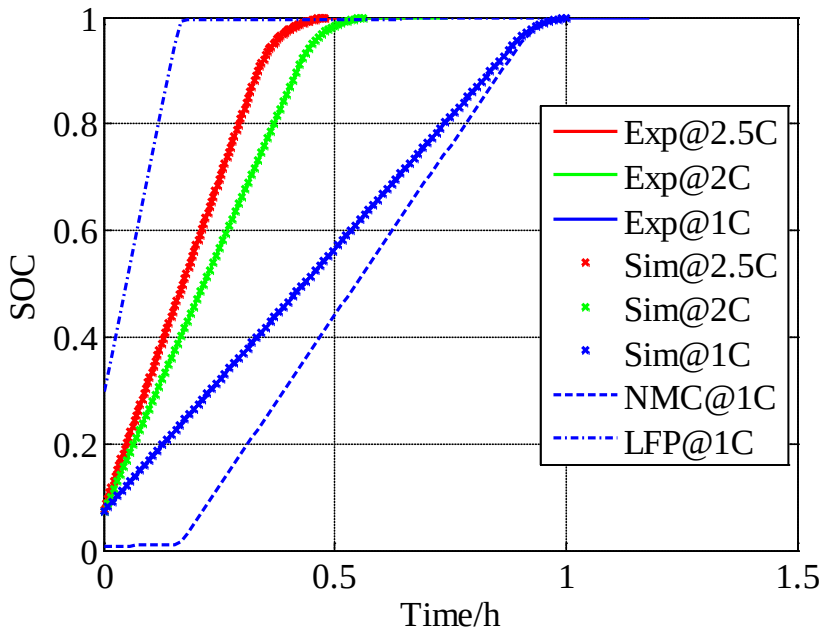

Figure 55. Comparison of SOC at 1C, 2C, and 2.5C during charging at 25°C.

In addition, ion concentration on the surface of LFP particles and the location of the moving interface between the two-phase in the LFP particles are plotted in (a) and (b) in Figure 56. The initial SOC of the cell before charging is set to be 10%. Ions in the particles are evenly distributed within the two-phase region, where β and α phase are in the shell and core, respectively. The initial interface is located at 0.62 of the particle's radius. When the charging current is applied, α phase is generated on the surface of the particles, which results in a generation of the second interface. As a result, three layers inside of the particle are formed and two interfaces coexist, which is α/β/α from the shell to the core. Since there is no ion concentration gradient around the first interface, it stays as before; but the second interface is in motion because of decreasing amount of ions in the outer layer. As ion concentration in α phase decreases, the layer of α phase is getting thicker and the second interface moves toward the first interface. As a result, r/Rs decreases to less than 1. When the second interface meets the first interface, where r/Rs is 0.67, β phase completely

disappears and only α phase is left inside of the particle. Then r/Rs drops to 0, and there exists only α phase inside of the LFP particles.

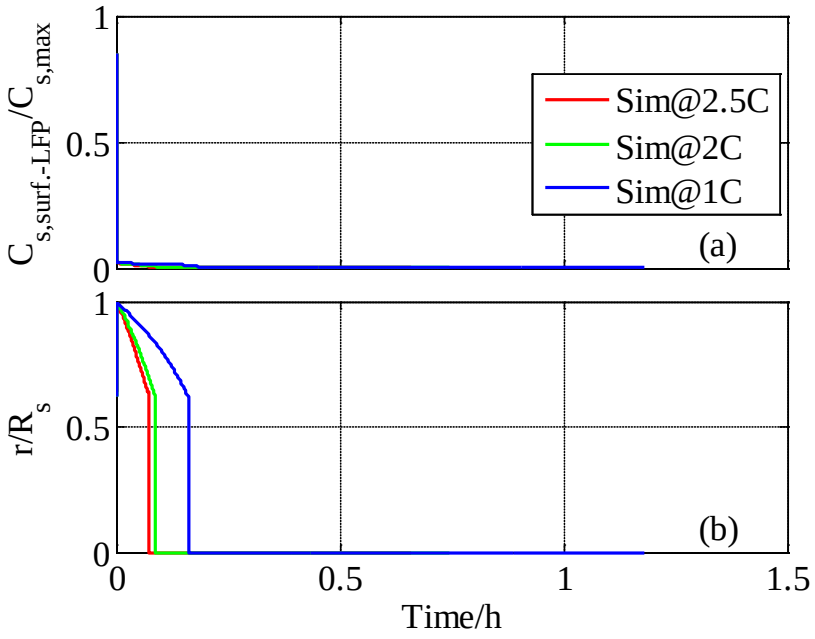

Figure 56. Ion concentration on the surface of LFP particles and the location of the interface inside of LFP particles at 1C, 2C, and 2.5C during charging at 25°C.

4.4.3 Response at different ambient temperatures

When cells are charged and discharged, heat is generated and transferred to ambient. Temperatures on the surface of the cells measured by infrared camera are used to analyze heat generation rates. However, the amount of heat generated is not easy to accurately measure. Therefore, a calorimeter is designed using two thermal-electric-modules, which facilitates dynamic measurements of heat generated during discharging and charging processes. The heat generated in a cell is described based on the energy equation of (74) that does not take heat of mixing [61] into account. Comparison between simulations (solid lines) and experiments (dotted lines) are plotted in Figure 57 and Figure 58. During discharging, the ROM can predict the

measured heat generation, except the discrepancy at the end of discharging caused by mismatch of terminal voltage as shown in Figure 45. Even for the period of relaxation, heat is continuously generated because of ionic currents flowing within and among particles. Since ROM does not consider gradient of ion concentrations within particles, heat generation after a current interruption becomes immediately zero [61]. During charging process, a discrepancy between the simulations and experiments is observed at the beginning of charging, which is caused by the increased overpotential of LFP during charging.

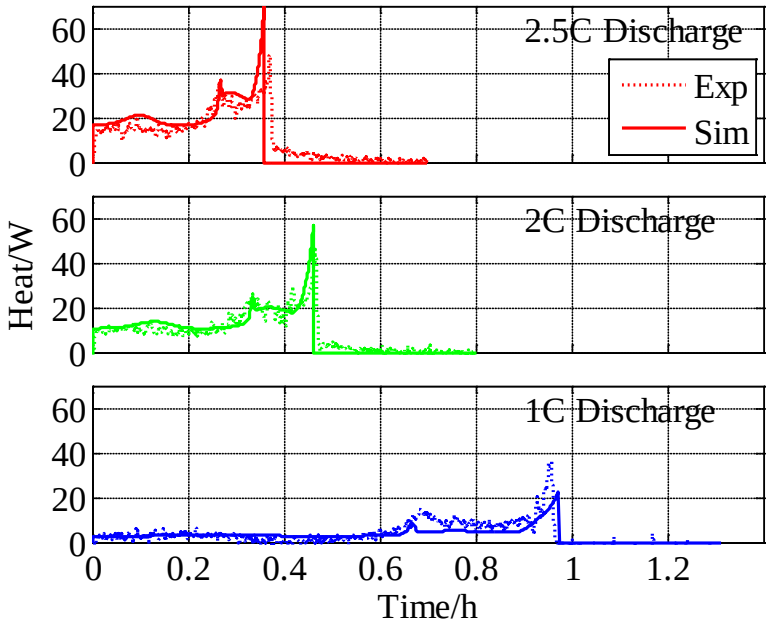

Figure 57. Heat generation at 1C, 2C, and 2.5C during discharging at 25°C.

Heat generation of the blended cells are strongly affected by characteristic of two active materials. During both discharging and charging, there are two peaks of heat generation rate. The first one is produced when NMC are almost saturated and LFP becomes a dominant part for chemical reactions. The second one is formed at the very end of the discharging process, when LFP are almost saturated and carbons are almost depleted. Accordingly, two peaks of heat

generation rate are observed in both simulation and experimental data. The first and the second one are corresponding to instants when ions in NMC and LFP are saturated respectively, and are determined by the mass ratio of NMC material.

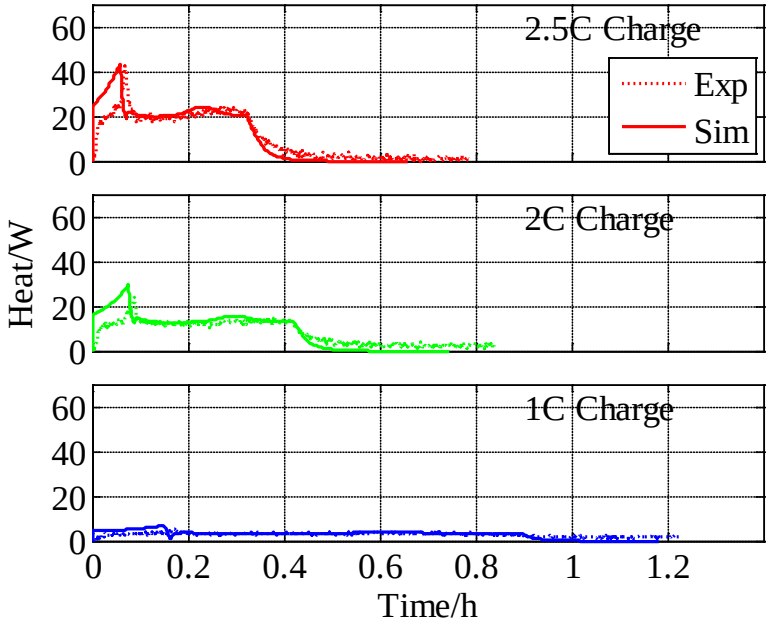

Figure 58. Heat generation at 1C, 2C, and 2.5C during charging at 25°C.

The ROM validated at 25 °C is further developed at different ambient temperatures. Cells are placed in a thermal chamber to keep the ambient temperature constant. At the same time, small current rates are applied to minimize effects of the generating heat on the cell performance during discharging. Comparison between simulated and experimental terminal voltage at different ambient temperatures is plotted in Figure 59, where the diffusion coefficient of NMC and graphite are fitted to experimental data using exponential functions, as shown in Figure 60, and incorporated into the ROM aforementioned. Sensitivity analysis of parameters on performance shows no significant dependence of temperature on diffusion coefficient of LFP, which can also be seen from the terminal voltage during 0.1C discharging at different temperatures. As shown in

Figure 61, starting from 100% SOC, the terminal voltage at different ambient temperatures shows a big difference at around 8h, which corresponds to saturation of NMC, and a small difference at the end of discharging. It also implies the NMC and graphite is more sensitive to temperature than LFP.

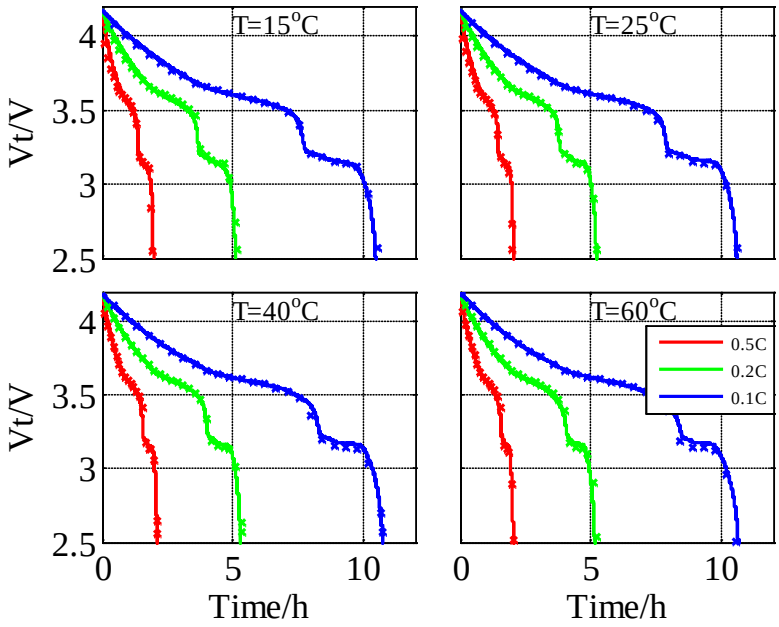

Figure 59. Experimental (solid line) and simulated terminal voltage (dotted line) during discharging at 0.1C, 0.2C and 0.5C rate and different ambient temperatures.

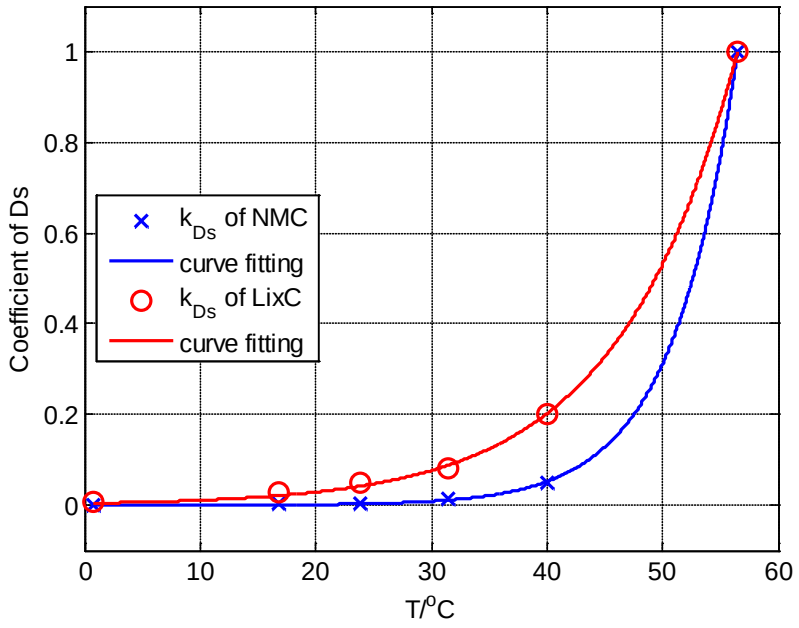

Figure 60. Diffusion coefficient versus temperature.

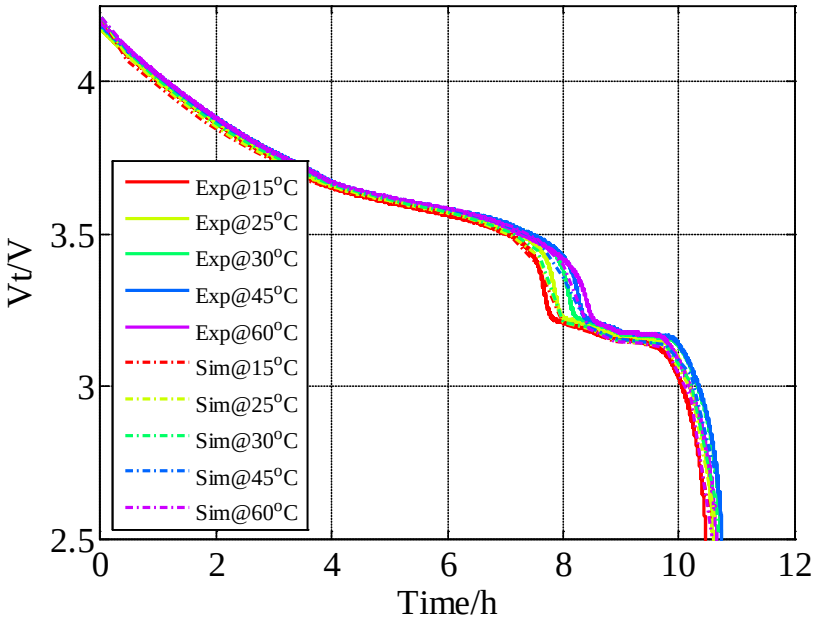

Figure 61. Experimental (solid line) and simulated terminal voltage (dotted line) during discharging at 0.1C rate and different ambient temperatures of 15, 30, 45, and 60°C.

4.5 Application

4.5.1 Effects of mass ratio on discharge performance

In section 4.3, the effect of mass ratio on the equilibrium potential of the blended cathode is analyzed. Likewise, performances of cells can be analyzed as a function of the mass ratio of active materials. Effects of the ratio on terminal voltage and heat generation rate is shown in (a) and (b) Figure 62. The higher the ratio of LFP is, the longer becomes the plateau in terminal voltage. At the same time, the magnitude of two peaks of heat generation becomes large and appears early because the saturation of ions in NMC occurs at the first. The blending ratio of multiple active materials is an important factor for design of cells and can significantly affects the characteristics of cell performances, which can be predicted using the developed ROM.

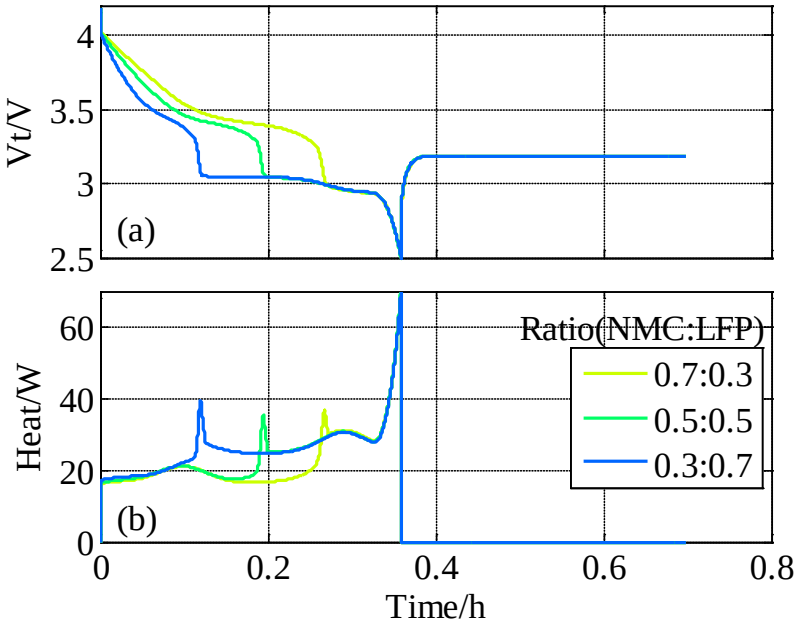

Figure 62. Comparison of terminal voltage (a) and heat generation rate (b) at 2.5C during discharging at 25 °C with different mass ratio between NMC and LFP.

4.5.2 SOC estimation

The equations in previous chapters show that the SOC can be calculated using the average ion concentration of the active materials in each composite electrode of a battery, which is given in the ROM. The accuracy of the estimation can be further improved by error correction techniques. Typical error sources are the inaccuracy of the ROM and initial values of the states of the ROM that are unknown at the beginning of calculation. Those errors can be reduced by feedback loops that amplify the difference of the battery and ROM responses and continuously correct states of the ROM. In addition, there are other sources of errors that include noises of measurements caused by sensors. EKF is employed to compensate those errors, so that the accuracy of SOC estimation can be further increased.

4.5.2.1 The principle of EKF

Kalman Filters have been proved over the last decade as the very effective algorithm for stochastic processes that suppresses process and sensor noises and at the same time reduces model errors. Since the ROM is nonlinear, the KF is extended to consider the nonlinearity. A nonlinear system can be described using the following difference equations,

$$\begin{aligned} \mathbf{x}_k &= f\left(\mathbf{x}_{k-1}, \mathbf{u}_{k-1}, \mathbf{w}_{k-1}\right) \\ \mathbf{z}_k &= h\left(\mathbf{x}_k, \mathbf{v}_k\right) \end{aligned} \quad . \tag{78}$$

where x_k and z_k are the states and the measurement of output at a time step k, for a given input u_{k-1} and a state x_{k-1} at the previous time step $k-1$. w_k and v_k represent the process noises and measurement noises, respectively. Both of the noises are assumed to be normally distributed with static, zero mean and constant covariance, which are described as follows,

$$\begin{aligned} p(w) &\sim N(0, Q) \\ p(v) &\sim N(0, R) \end{aligned} \quad . \tag{79}$$

The EKF algorithm consists of three parts: initialization, time update, and measurement update as shown in Table 8.

Table 8 Steps for Extended Kalman filter

Initialization:	Initial state estimation: $\hat{\mathbf{x}}_{k-1}$	(80)
	Initial error covariance : $\mathbf{P}_{k-1}$	
	Initial process noise covariance : $\mathbf{W}_k$	
	Initial measurement covariance : $\mathbf{V}_k$	
Time update:	State prediction: $\hat{\mathbf{x}}_k^- = f\left(\hat{\mathbf{x}}_{k-1}, \mathbf{u}_{k-1}, 0\right)$	(81)
	Error covariance prediction: $\mathbf{P}_k^- = \mathbf{A}_k \mathbf{P}_{k-1} \mathbf{A}_k^{\mathrm{T}} + \mathbf{W}_k \mathbf{Q}_{k-1} \mathbf{W}_k^{\mathrm{T}}$	
Measurement update:	Kalman gain: $\mathbf{K}_k = \mathbf{P}_k^- \mathbf{H}_k^{\mathrm{T}} \left(\mathbf{H}_k \mathbf{P}_k^- \mathbf{H}_k^{\mathrm{T}} + \mathbf{V}_k \mathbf{P}_{k-1} \mathbf{V}_k^{\mathrm{T}}\right)^{-1}$	(82)
	State correction: $\hat{\mathbf{x}}_k = \hat{\mathbf{x}}_k^- + \mathbf{K}_k \left(\mathbf{z}_k - h\left(\hat{\mathbf{x}}_k^-, 0\right)\right)$	
	Error covariance correction: $\mathbf{P}_k = (\mathbf{I} - \mathbf{K}_k \mathbf{H}_k) \mathbf{P}_k^-$	

where **A**, **W**, is the Jacobian matrix of partial derivatives of the nonlinear function, f , with respect to x and w at the k-1 step. **H** and **V** are the Jacobian matrix of partial derivatives of h with respect to x and w evaluated at the k step.

The block diagram for estimation of SOC with EKF based ROM is shown in Figure 63, where two algorithms for time update and measurement update are included. SOC is calculated based on estimated ion concentrations.

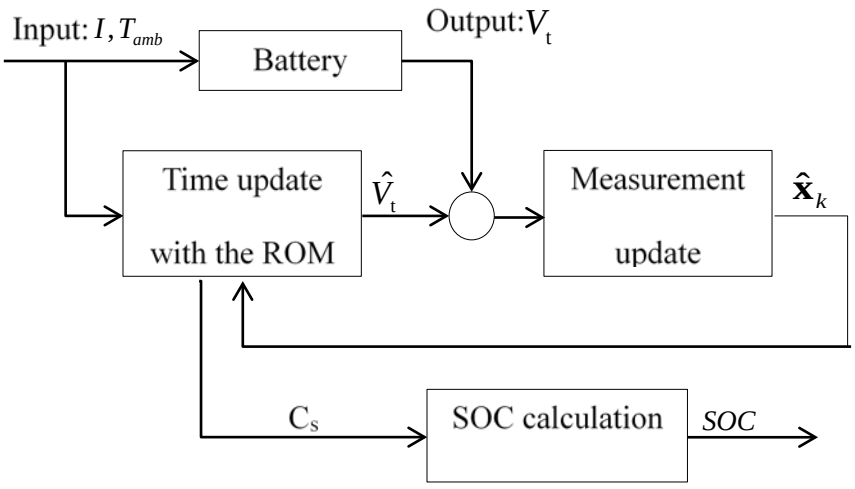

Figure 63. Block diagram for SOC estimation based on the ROM with EKF.

The terminal voltage is the output of the battery, which is affected instantaneously by ion concentration and the current applied, so the average concentration and the surface concentration are chosen as the states. In addition, there are three active materials, so the all the variables that affect the terminal voltage are six and affect each other. Relationships between those variables are formulated as follows;

a) Based on the charge conservation law, the total number of lithium ions in the battery is constant, so the amount of change of ions in the anode should be the same as that of ions in the cathode,

$$\begin{aligned} &n_{Li} \equiv \text{constant} \\ &\left(\Delta c_{s,ave} AL\varepsilon_s\right)_{\text{LixC}} + \left(\Delta c_{s,ave} AL\varepsilon_s\right)_{\text{LFP}} + \left(\Delta c_{s,ave} AL\varepsilon_s\right)_{\text{NMC}} = 0 \end{aligned} \quad (83)$$

b) Since the potentials of NMC and LFP particles are the same, any change of the surface concentration of NMC leads to change of LFP concentration, which has already been considered in the ROM. No feedback correction is needed for the surface concentration of LFP particles directly.

c) Moreover, the average concentration in NMC and carbon particles can be derived directly from the model. However, due to presence of the multiple layers in the LFP particles the average concentrations cannot be calculated directly from the concentration and should be calculated based on the average concentration in each layer and the location of the interface between the layers. The relationship between the change of average concentration and the change of interface location are shown as,

$$\begin{aligned}&\text{1st interface}: \ \Delta c_{s,ave} \cdot \frac{4}{3}\pi R_s^3 = \left(c_{s,1} - c_{s,0}\right) \cdot \left[\frac{4}{3}\pi\left(r_0 + \Delta r_0\right)^3 - \frac{4}{3}\pi {r_0}^3\right] \\ &\text{2nd interface}: \Delta c_{s,ave} \cdot \frac{4}{3}\pi R_s^3 = \left(c_{s,2} - c_{s,1}\right) \cdot \left[\frac{4}{3}\pi\left(r_1 + \Delta r_1\right)^3 - \frac{4}{3}\pi {r_1}^3\right]\end{aligned} . \tag{84}$$

Consequently, the average concentration in NMC particles, the location of the interface in LFP particles, and the surface concentration on NMC particles are the states that are predicted by the EKF and enable to calculate the other three variables. The input, states, and output of the ROM are summarized as below,

$$\begin{aligned}x^{k+1} &= \begin{bmatrix} c_{s,\text{NMC}} \\ r_{0,\text{LFP}} \\ c_{s,surf,\text{NMC}} \end{bmatrix}^{k+1} = f\left(x^k, u^k\right) \\ u &= I \\ y &= V_t = h\left(x^{k+1}, u^{k+1}\right)\end{aligned} . \tag{85}$$

The Kalman gain can be calculated using **A** and **H** that are the Jacobian matrix of partial derivatives of *f* and *h* with respects to *x*,

$$A = \frac{\partial f}{\partial x} = \begin{bmatrix} 1 & 0 & 0 \\ 0 & 1 & 0 \\ 0 & 0 & 1 \end{bmatrix}$$
$$H = \frac{\partial h}{\partial x} = \begin{bmatrix} \frac{\partial V_t}{\partial c_{s,\mathrm{NMC}}} & \frac{\partial V_t}{\partial r_{0,\mathrm{LFP}}} & \frac{\partial V_t}{\partial c_{s,surf,\mathrm{NMC}}} \end{bmatrix}. \quad (86)$$

A is a 3×3 identity matrix, while **H** cannot be expressed explicitly with a function due to the coupled equations introduced above. So **H** is calculated by a difference method as an example for the first term in **H** below,

$$\frac{\partial V_t}{\partial c_{s,\mathrm{NMC}}} = \frac{V_t(c_s + \Delta c_s) - V_t(c_s)}{\Delta c_{s,\mathrm{NMC}}}$$
$$\text{for NMC particles: } \Delta c_s = \delta \quad (87)$$
$$\text{for LixC particles: } \Delta c_s = -\delta \frac{(AL\varepsilon_s)_{\mathrm{NMC}}}{(AL\varepsilon_s)_{\mathrm{LixC}}}.$$

When the Kalman gain for the three states are derived, the gains for the other variables can be calculated based on mass conservation.

$$\begin{bmatrix} \Delta c_{s,\mathrm{NMC}} \\ \Delta r_{0,\mathrm{LFP}} \\ \Delta c_{s,surf,\mathrm{NMC}} \end{bmatrix} = \begin{bmatrix} K_{\mathrm{NMC}} \\ K_{\mathrm{LFP}} \\ K_{\mathrm{surf}} \end{bmatrix} \cdot error$$
$$\left[\Delta c_{s,\mathrm{LixC}}\right] = -\begin{bmatrix} \frac{(AL\varepsilon_s)_{\mathrm{NMC}}}{(AL\varepsilon_s)_{\mathrm{LixC}}} & \frac{(AL\varepsilon_s)_{\mathrm{LFP}}}{(AL\varepsilon_s)_{\mathrm{LixC}}} \frac{(c_{s,1} - c_{s,0}) \cdot \left[(r_0 + \Delta r_0)^3 - r_0^3\right]}{R_s^3} \end{bmatrix} \begin{bmatrix} K_{\mathrm{NMC}} \\ K_{\mathrm{LFP}} \end{bmatrix} \cdot error \quad (88)$$
$$\Delta c_{s,surf,\mathrm{LixC}} = -\frac{(AL\varepsilon_s)_{\mathrm{NMC}}}{(AL\varepsilon_s)_{\mathrm{LixC}}} \cdot \Delta c_{s,surf,\mathrm{NMC}}$$

On one hand, a high gain can potentially lead to a numerical instability of the model. On the other hand, a low gain results in prediction of the states only by time update without measurement correction. If estimation error of terminal voltage is less than 30mV, then gain is set to be zero. In addition, the maximum gain is limited under consideration of the sign of the gain.

$$abs(K) \leq \text{constant}$$
$$\text{if } error < 30mV, \text{ then } K = 0 \tag{89}$$

4.5.2.2 Results and analysis

The proposed algorithm for SOC estimation using EKF based on ROM is compared with experimental data of SOC estimated using Coulomb counting method, when different charging and discharging current rates are applied as inputs. Initial SOC is accurately predicted from the OCV-SOC lookup table after a sufficient relaxation. For the comparison, a cell is discharged at 2C discharge and the load profile, terminal voltage, and SOC estimation are plotted as shown in Figure 64.

For a fully charged battery, the initial SOC is 100%. A 2C discharge current is applied to the battery until the terminal voltage reaches 2.5V, followed by a 1200s relaxation period, as shown in plot (a). The measured terminal voltage and the experimental SOC are plotted in (b) and (c) in solid line.

The same load profiles are applied to the ROM with and without EKF. At the two cases the initial SOC is set to 50%. The line with stars shows the results of the ROM with EKF and the dot line for ROM without EKF. Even 50% SOC error at the beginning EKF with ROM quickly catches up the experimental data of the terminal voltage as well as SOC, while only ROM without EKF is unable to reduce errors and never reaches the actual value. The errors for two cases are also plotted as shown in Figure 65. With correction of measurements of terminal voltage, the absolute SOC estimation error can always be kept less than 5% for the load profile.

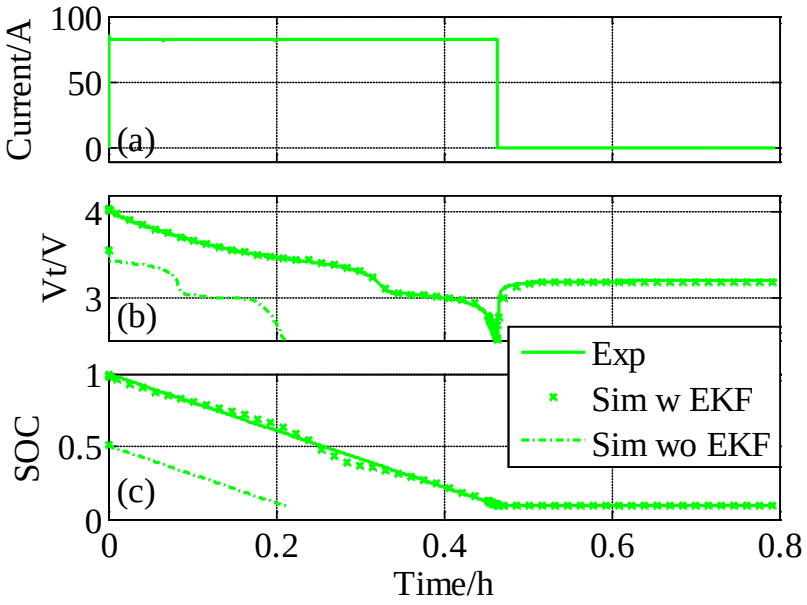

Figure 64. Comparison of terminal voltage and SOC at 2C discharging rate at 25°C. (a) load profile, (b) terminal voltage, (c) SOC estimation.

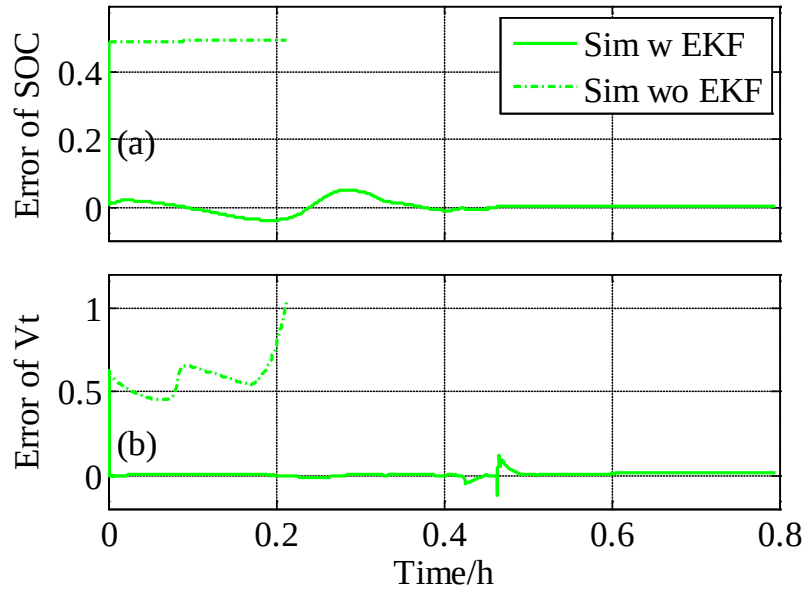

Figure 65. Errors of terminal voltage and SOC at 2C discharging rate at 25°C with and without EKF. (a) Error in SOC, (b) error in terminal voltage.

The results of ROM with EKF show improvement over the ROM without EKF, but there are still some errors, particularly in terminal voltage caused by the inaccuracy of the model. For reduction of the voltage errors, the gain has been made dependent upon the error. If the error is less than 30mV, then the gain is set to 0, so that the measurement correction from the terminal voltage can be inactive and only time update becomes active from the model.

The same load profile shown in (a) of Figure 64 is applied to the model, and the error of terminal voltage and SOC are plotted in (a) and (b) of Figure 66. The solid and the dot line show the errors of the EKF based ROM with and without limiting the Kalman gain, respectively. The two different gains make no difference in the response time to remove the initial SOC error. However, limitation of the gain prevents unnecessary amplification of errors, so that the accuracy of SOC estimation is improved. At around 0.2h, the error of terminal voltage is less than 30mV, so the gain is set to be zero and as a result no feedback takes effect. Then the SOC is calculated only based on the model itself and the error of SOC remains constant. If there is no limitation of the gain and the terminal voltage error is very small, the updates try to correct errors based on the measurement errors, so the absolute error can increase. Limiting the gain reduces the error caused by the inaccuracy of the model.

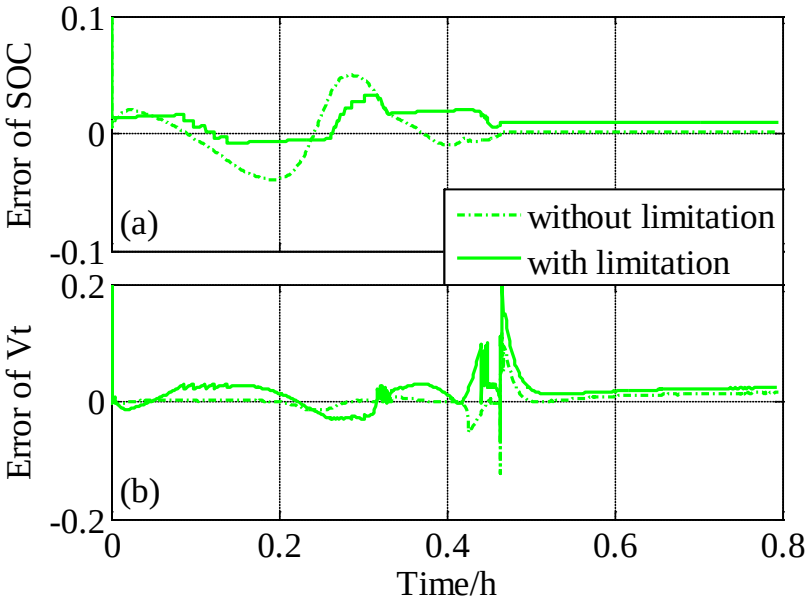

Figure 66. Error of terminal voltage and SOC by EKF with or without Kalman gain limitation at 2C discharging at 25°C. (a) error in SOC, (b) error in terminal voltage.

The EKF with gain limitation with the ROM are tested under the same testing profiles introduced in the previous chapter, including 1C, 2C, and 2.5C, during both discharging and charging. Errors in SOC and terminal voltage during discharging and charging are plotted in Figure 67 and Figure 68, respectively. The SOC estimation errors during both discharging and charging are reduced to less than 5% under the cycle. However, the errors of the terminal voltage during discharging are relatively high, particularly at the end of discharging, when the terminal voltage reaches 2.5V. . At the end of discharging, the terminal voltage drops rapidly, which cannot be caught up by the feedbacks. In addition, SOC becomes low, and the derivatives in **H** matrix becomes very large, which results in over responses of the model. However, the algorithm enables the errors to converge to a steady state after a transient response.

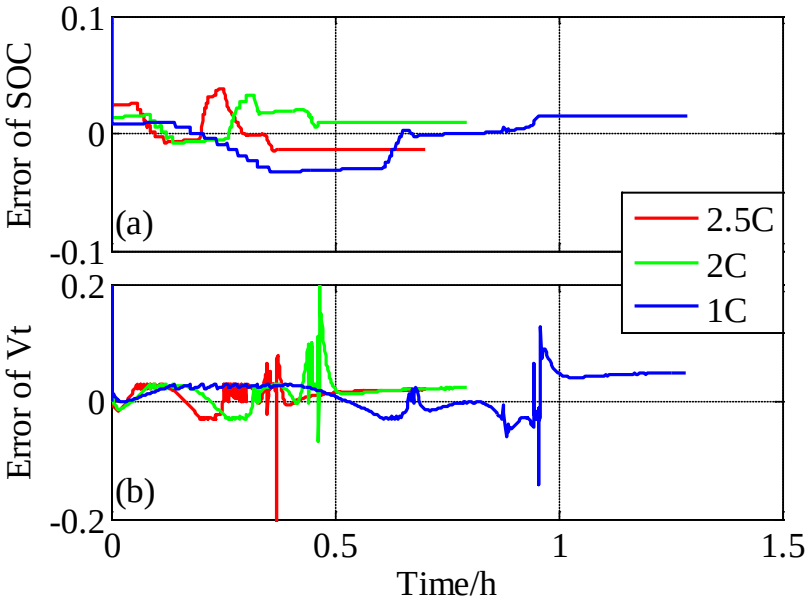

Figure 67. Error of terminal voltage and SOC by EKF with gain limitation at 1C, 2C, and 2.5C during discharging at 25°C. (a) error in SOC, (b) error in terminal voltage.

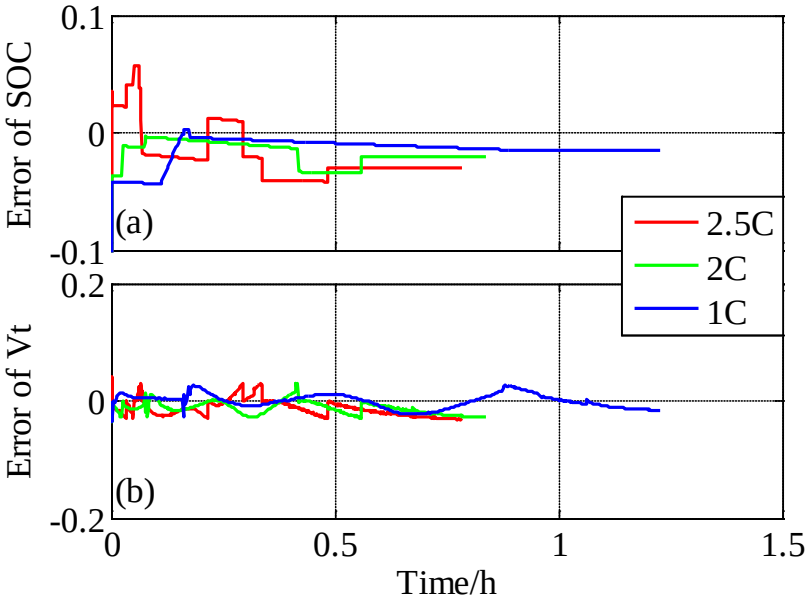

Figure 68. Error of terminal voltage and SOC by EKF with gain limitation at 1C, 2C, and 2.5C during discharging at 25°C. (a) error in SOC, (b) error in terminal voltage.

During charging, the error of terminal voltage is less than 50mV, and the error of SOC is less than 4%, because the model is more accurate during charging than discharging. Before the charge, the battery is discharged with 1C rate and rested for 1200s. The SOC of the battery is 7% and the ion concentration distribution reached a steady state. LFP particles haveα phase in the core and β phase in the shell. The interface between the two phases is located at r_0/R_s=0.67. When the charging process starts, the ion concentration and the interface location change with time. In order to test tracking performance of the algorithm, a SOC was set to 20%, where two phases in LFP particles coexist, but the interface is located at r_0/R_s=0.96, which is closer to the particle surface than the actual interface. When the algorithm is active, the location of this interface is moved to the actual value. Simulation results of error of SOC along with interface locations between two phases are plotted in Figure 69. The location of the first and the second interface shows the movement of the interface next to the surface, and the interface near to the core, respectively. Once the initial error is corrected with measurement update, the accuracy of ROM is improved, so the errors of terminal voltage and SOC decrease.

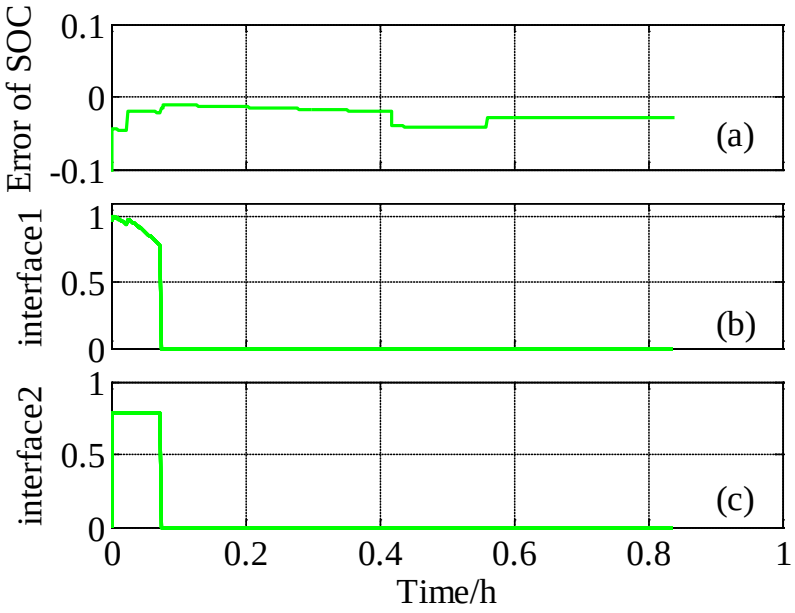

Figure 69. Simulation results of the interface location in LFP particles by EKF with gain limitation at 2C charging at 25°C; (a) error in SOC, (b) location of the first interface from the particle surface, (c) the location of the second interface from the particle surface.

A new estimation method for SOC is proposed that is based on the ROM and EKF. Accuracy is further improved by limiting the Kalman gains that otherwise continuously attempt to correct errors and produce unnecessary extra errors.

The designed method is experimentally tested at different load profiles and effects of model accuracy and typical initial SOC errors on performance of the method is analyzed. The responses of terminal voltage and SOC estimation using ROM, and ROM with EKF are compared with each other, where SOC is compared with Coulomb counting. EKF based ROM shows the best performance in accuracy. Errors caused by models are compensated by an extra feedback loop where the terminal voltage difference between the battery and the model is used to change the average and surface ion concentration of the ROM. The estimation error for SOC is around 4% that is less than that of classical methods. However, the accuracy of the proposed method depends

on model accuracy. So the accuracy of SOC estimation could be further improved with a more accurate battery model that considers degradation.

4.6 Summary

A reduced order electrochemical and thermal model for a high power pouch type cell with blended cathode of NMC and LFP is developed and validated against experimental data. The model is based on two separate sub-models for NMC and LFP cell that have been previously developed. Integration of the two models is successfully conducted considering current distribution, different equilibrium potentials, heat generation rate and blending ratio. The model is capable of predicting static and transient behaviors of the cell during both charging and discharging at various constant current rates and various ambient temperatures, which include terminal voltage and SOC in addition to other internal variables, such as current density, ion concentration in each active material, potentials of both electrode, even generation of new phase and moving of the interface between two phases in LFP material, and heat generation rate. These variables are essential for optimization of cell design and operation. Here are a summary of major findings,

1. NMC material can be better utilized by blending it with LFP material.
2. The analysis of SOC, ion concentration and current density in each cathode material shows that during both charging and discharging NMC materials play a dominant role in reaction at high SOC range, while LFP is dominant at low SOC range.
3. Mass ratio between NMC and LFP significantly affects terminal voltage and heat generation.
4. The SOC estimation error can be reduced to less than 4% with EKF based ROM.

Chapter 5 Conclusion

This work focuses on developing a model for a high power pouch type cell with blended cathode of NMC and LFP based on electrochemical and thermal principles. Since the structure and the ion diffusion mechanisms of the two cathodes are different, submodel for each material should be developed firstly and then coupled with each other. For implementation in BMS, higher calculation speed is required, so the order of the models needs to be reduced.

The research starts with model order reduction of a previously developed full order electrochemical model for LMO batteries. The performance of the ROM for LMO batteries shows promising results with respect to static and dynamic responses, where the terminal voltage and temperature is tested over both a single cycle and multiple cycles.

Then the ion diffusion mechanism of LFP chemistry is studied and a new reduced order mathematical model is developed. Particularly, the ion distribution in LFP particles are approximated by a shrinking core model that is described using diffusion equations and simplified using polynomial approximation. The model is capable of representing the three major characteristics of the battery determined by the two-phase transition taking place in LFP particles that include voltage plateau, hysteresis between charging and discharging, and path dependence.

Based on two separate sub-models for NMC and LFP cells that have been previously developed, a reduced order electrochemical and thermal model for a high power pouch type cell with blended cathode of NMC and LFP is developed and validated against experimental data. Integration of the two models are conducted considering current distribution, different equilibrium

potentials, heat generation rate and blending ratio. The model is capable of predicting static and transient behaviors of the cell during both charging and discharging at various constant current rates and various ambient temperatures, which include terminal voltage and SOC in addition to other internal variables, such as current density, ion concentration in each active material, potentials of both electrode, even generation of new phase and moving of the interface between two phases in LFP material, and heat generation rate. These variables are essential for optimization of cell design and operation.

The three ROMs for cells with single cathode of NMC or LFP, and blended cathode are separately validated against experimental data of terminal voltage and SOCs during galvanostatic charging and discharging process, and then is used to analyze the major characteristics of each cathode.

Major accomplishments and findings are summarized as follows;

- Validation and analysis of the ROM for NMC cells:
    - The computational time of the ROM takes less than 15% of the FOM, measured by a PC equipped with a dual core Intel Core I7 CPU 870 processor.
    - The terminal voltage is better predicted when effects of temperature on the coefficients have been considered. Particularly, consideration of the temperature dependence of the diffusion coefficient of solid particles and the resistance of the SEI layer increases the accuracy of the terminal voltage and temperature at various operating conditions.
    - Prediction of temperature becomes much more accurate after considering the heat of mixing term. The absolute error in the temperature prediction is less than 1.5°C.
- Validation and analysis of the ROM for LFP cells:

- The model can capture realistic behaviors of LFP cells that includes plateau, hysteresis and particularly path dependence that is otherwise not possible;
- Larger discharge capacity has been observed when α phase is present in the shell at the beginning, while the charge capacity is larger when β phase is present.
- The path dependence is a function of current rates and SOC range. The dependence becomes severe when current rates increase or SOC ranges from 30% to 70%;
- Performance is more affected by the cycling history during discharging than that during charging.

- Validation and analysis of the ROM for blended cells:
  - NMC material can be better utilized by blending it with LFP material.
  - The analysis of SOC, ion concentration and current density in each cathode material shows that during both charging and discharging NMC materials play a dominant role in reaction at high SOC range, while LFP is dominant at low SOC range.
  - Mass ratio between NMC and LFP significantly affects terminal voltage and heat generation.
  - The SOC estimation error can be reduced to less than 4% with EKF based ROM.

Future work will include development of a model for degradation and its integration into the model and prediction of capacity and power available.

References

[1] R. Koksbang, J. Barker, H. Shi, and M. Saidi, "Cathode materials for lithium rocking chair batteries," *Solid state ionics,* vol. 84, pp. 1-21, 1996.

[2] A. Ritchie and W. Howard, "Recent developments and likely advances in lithium-ion batteries," *Journal of Power Sources,* vol. 162, pp. 809-812, 2006.

[3] J. W. Fergus, "Recent developments in cathode materials for lithium ion batteries," *Journal of Power Sources,* vol. 195, pp. 939-954, 2010.

[4] B. Xu, D. Qian, Z. Wang, and Y. S. Meng, "Recent progress in cathode materials research for advanced lithium ion batteries," *Materials Science and Engineering: R: Reports,* vol. 73, pp. 51-65, 2012.

[5] S. B. Chikkannanavar, D. M. Bernardi, and L. Liu, "A review of blended cathode materials for use in Li-ion batteries," *Journal of Power Sources,* vol. 248, pp. 91-100, 2014.

[6] W.-J. Zhang, "Structure and performance of $LiFePO_4$ cathode materials: A review," *Journal of Power Sources,* vol. 196, pp. 2962-2970, 2011.

[7] N. Yabuuchi and T. Ohzuku, "Novel lithium insertion material of $LiCo_{1/3}Ni_{1/3}Mn_{1/3}O_2$ for advanced lithium-ion batteries," *Journal of Power Sources,* vol. 119, pp. 171-174, 2003.

[8] A. Hashem, A. Abdel-Ghany, A. Eid, J. Trottier, K. Zaghib, A. Mauger, *et al.*, "Study of the surface modification of $LiNi_{1/3}Co_{1/3}Mn_{1/3}O_2$ cathode material for lithium ion battery," *Journal of Power Sources,* vol. 196, pp. 8632-8637, 2011.

[9] H. Y. Tran, C. Täubert, M. Fleischhammer, P. Axmann, L. Küppers, and M. Wohlfahrt-Mehrens, "$LiMn_2O_4$ Spinel/$LiNi_{0.8}Co_{0.15}Al_{0.05}O_2$ Blends as Cathode Materials for Lithium-Ion Batteries," *Journal of The Electrochemical Society,* vol. 158, pp. A556-A561, 2011.

[10] P. Albertus, J. Christensen, and J. Newman, "Experiments on and Modeling of Positive Electrodes with Multiple Active Materials for Lithium-Ion Batteries," *Journal of The Electrochemical Society,* vol. 156, p. A606, 2009.

[11] T. Numata, C. Amemiya, T. Kumeuchi, M. Shirakata, and M. Yonezawa, "Advantages of blending $LiNi_{0.8}Co_{0.2}O_2$ into $Li_{1+x}Mn_{2-x}O_4$ cathodes," *Journal of Power Sources,* vol. 97-8, pp. 358-360, Jul 2001.

[12] A. Manthiram and W. Choi, "Suppression of Mn Dissolution in Spinel Cathodes by Trapping the Protons within Layered Oxide Cathodes," *Electrochemical and Solid-State Letters,* vol. 10, p. A228, 2007.

[13] K.-W. Nam, W.-S. Yoon, H. Shin, Y. C. KYUNG, S. Choi, and X.-Q. Yang, "In situ X-ray diffraction studies of mixed $LiMn_2O_4$-$LiNi_{1/3}Co_{1/3}Mn_{1/3}O_2$ composite cathode in Li-ion cells during charge-discharge cycling," *Journal of power sources,* vol. 192, pp. 652-659, 2009.

[14] K. S. Lee, S. T. Myung, D. W. Kim, and Y. K. Sun, "AlF_3-coated $LiCoO_2$ and $Li[Ni_{1/3}Co_{1/3}Mn_{1/3}]O_2$ blend composite cathode for lithium ion batteries," *Journal of Power Sources,* vol. 196, pp. 6974-6977, Aug 15 2011.

[15] N. Imachi, Y. Takano, H. Fujimoto, Y. Kida, and S. Fujitani, "Layered Cathode for Improving Safety of Li-Ion Batteries," *Journal of The Electrochemical Society,* vol. 154, p. A412, 2007.

[16] J. F. Whitacre, K. Zaghib, W. C. West, and B. V. Ratnakumar, "Dual active material composite cathode structures for Li-ion batteries," *Journal of Power Sources,* vol. 177, pp. 528-536, Mar 1 2008.

[17] S.-B. Kim, K. Lee, W. Choi, W.-S. Kim, I. Jang, H. Lim, *et al.*, "Preparation and cycle performance at high temperature for Li $[Ni_{0.5}Co_{0.2}Mn_{0.3}]O_2$ coated with $LiFePO_4$," *Journal of Solid State Electrochemistry,* vol. 14, pp. 919-922, 2010.

[18] K. G. Gallagher, S. H. Kang, S. U. Park, and S. Y. Han, "$xLi_2MnO_3(1-x)LiMO_2$ blended with $LiFePO_4$ to achieve high energy density and pulse power capability," *Journal of Power Sources,* vol. 196, pp. 9702-9707, Nov 15 2011.

[19] M. Xiao, S.-Y. Choe, and F. Rahman, "Static and dynamic analysis of Li-polymer battery using thermal electrochemical model," in *Innovative Technologies for an Efficient and Reliable Electricity Supply (CITRES), 2010 IEEE Conference on*, 2010, pp. 309-316.

[20] K. A. Smith, C. D. Rahn, and C.-Y. Wang, "Control oriented 1D electrochemical model of lithium ion battery," *Energy Conversion and Management,* vol. 48, pp. 2565-2578, 2007.

[21] H. He, R. Xiong, X. Zhang, F. Sun, and J. Fan, "State-of-charge estimation of the lithium-ion battery using an adaptive extended Kalman filter based on an improved Thevenin model," *Vehicular Technology, IEEE Transactions on,* vol. 60, pp. 1461-1469, 2011.

[22] K. A. Smith, C. D. Rahn, and C.-Y. Wang, "Model-based electrochemical estimation and constraint management for pulse operation of lithium ion batteries," *Control Systems Technology, IEEE Transactions on,* vol. 18, pp. 654-663, 2010.

[23] X. Li, M. Xiao, and S.-Y. Choe, "Reduced order model (ROM) of a pouch type lithium polymer battery based on electrochemical thermal principles for real time applications," *Electrochimica Acta,* vol. 97, pp. 66-78, 2013.

[24] S. Santhanagopalan and R. E. White, "Online estimation of the state of charge of a lithium ion cell," *Journal of power sources,* vol. 161, pp. 1346-1355, 2006.

[25] R. Klein, N. A. Chaturvedi, J. Christensen, J. Ahmed, R. Findeisen, and A. Kojic, "State estimation of a reduced electrochemical model of a lithium-ion battery," in *American Control Conference (ACC), 2010*, 2010, pp. 6618-6623.

[26] V. R. Subramanian, V. D. Diwakar, and D. Tapriyal, "Efficient macro-micro scale coupled modeling of batteries," *Journal of The Electrochemical Society,* vol. 152, pp. A2002-A2008, 2005.

[27] C. Speltino, D. Di Domenico, G. Fiengo, and A. Stefanopoulou, "Comparison of reduced order lithium-ion battery models for control applications," in *Decision and Control, 2009 held jointly with the 2009 28th Chinese Control Conference. CDC/CCC 2009. Proceedings of the 48th IEEE Conference on*, 2009, pp. 3276-3281.

[28] V. Pop, H. J. Bergveld, P. Regtien, J. O. het Veld, D. Danilov, and P. Notten, "Battery aging and its influence on the electromotive force," *Journal of the Electrochemical Society,* vol. 154, pp. A744-A750, 2007.

[29] G. L. Plett, "Extended Kalman filtering for battery management systems of LiPB-based HEV battery packs: Part 2. Modeling and identification," *Journal of power sources,* vol. 134, pp. 262-276, 2004.

[30] N. A. Chaturvedi, R. Klein, J. Christensen, J. Ahmed, and A. Kojic, "Modeling, estimation, and control challenges for lithium-ion batteries," in *American Control Conference (ACC), 2010*, 2010, pp. 1997-2002.

[31] I.-S. Kim, "The novel state of charge estimation method for lithium battery using sliding mode observer," *Journal of Power Sources*, vol. 163, pp. 584-590, 2006.

[32] A. J. Salkind, C. Fennie, P. Singh, T. Atwater, and D. E. Reisner, "Determination of state-of-charge and state-of-health of batteries by fuzzy logic methodology," *Journal of Power Sources*, vol. 80, pp. 293-300, 1999.

[33] S. Piller, M. Perrin, and A. Jossen, "Methods for state-of-charge determination and their applications," *Journal of power sources*, vol. 96, pp. 113-120, 2001.

[34] C. R. Pals and J. Newman, "Thermal modeling of the lithium/polymer battery II. Temperature profiles in a cell stack," *Journal of the Electrochemical Society*, vol. 142, pp. 3282-3288, 1995.

[35] M. Guo, G. Sikha, and R. E. White, "Single-particle model for a lithium-ion cell: Thermal behavior," *Journal of The Electrochemical Society*, vol. 158, pp. A122-A132, 2011.

[36] X. Li, M. Xiao, and S.-Y. Choe, "Reduced order of electrochemical model for a pouch type high power Li-polymer battery," in *Clean Electrical Power (ICCEP), 2011 International Conference on*, 2011, pp. 593-599.

[37] M. Xiao and S.-Y. Choe, "Dynamic modeling and analysis of a pouch type $LiMn_2O_4$/Carbon high power Li-polymer battery based on electrochemical-thermal principles," *Journal of Power Sources*, 2012.

[38] E. Wood, M. Alexander, and T. H. Bradley, "Investigation of battery end-of-life conditions for plug-in hybrid electric vehicles," *Journal of Power Sources*, vol. 196, pp. 5147-5154, 2011.

[39] A. K. Padhi, K. S. Nanjundaswamy, and J. B. Goodenough, "Phospho-olivines as positive-electrode materials for rechargeable lithium batteries," *Journal of the Electrochemical Society*, vol. 144, pp. 1188-1194, Apr 1997.

[40] A. Yamada, H. Koizumi, N. Sonoyama, and R. Kanno, "Phase change in Li_xFePO_4," *Electrochemical and Solid-State Letters*, vol. 8, pp. A409-A413, 2005.

[41] V. Srinivasan and J. Newman, "Discharge model for the lithium iron-phosphate electrode," *Journal of the Electrochemical Society*, vol. 151, pp. A1517-A1529, 2004.

[42] C. Wang, U. S. Kasavajjula, and P. E. Arce, "A discharge model for phase transformation electrodes: formulation, experimental validation, and analysis," *The Journal of Physical Chemistry C*, vol. 111, pp. 16656-16663, 2007.

[43] U. S. Kasavajjula, C. Wang, and P. E. Arce, "Discharge model for $LiFePO_4$ accounting for the solid solution range," *Journal of The Electrochemical Society*, vol. 155, pp. A866-A874, 2008.

[44] I. V. Thorat, T. Joshi, K. Zaghib, J. N. Harb, and D. R. Wheeler, "Understanding Rate-Limiting Mechanisms in LiFePO4 Cathodes for Li-Ion Batteries," *Journal of The Electrochemical Society*, vol. 158, p. A1185, 2011.

[45] M. Safari and C. Delacourt, "Mathematical Modeling of Lithium Iron Phosphate Electrode: Galvanostatic Charge/Discharge and Path Dependence," *Journal of the Electrochemical Society*, vol. 158, pp. A63-A73, 2011.

[46] V. Srinivasan and J. Newman, "Existence of path-dependence in the $LiFePO_4$ electrode," *Electrochemical and Solid State Letters*, vol. 9, pp. A110-A114, 2006.

[47] M. A. Roscher, J. Vetter, and D. U. Sauer, "Cathode material influence on the power capability and utilizable capacity of next generation lithium-ion batteries," *Journal of Power Sources,* vol. 195, pp. 3922-3927, 2010.
[48] M. Safari and C. Delacourt, "Mathematical Modeling of Lithium Iron Phosphate Electrode: Galvanostatic Charge/Discharge and Path Dependence," *Journal of The Electrochemical Society,* vol. 158, p. A63, 2011.
[49] W. Sigle, R. Amin, K. Weichert, P. A. van Aken, and J. Maier, "Delithiation study of $LiFePO_4$ crystals using electron energy-loss spectroscopy," *Electrochemical and Solid-State Letters,* vol. 12, pp. A151-A154, 2009.
[50] K. Weichert, W. Sigle, P. A. van Aken, J. Jamnik, C. B. Zhu, R. Amin, *et al.*, "Phase Boundary Propagation in Large $LiFePO_4$ Single Crystals on Delithiation," *Journal of the American Chemical Society,* vol. 134, pp. 2988-2992, Feb 15 2012.
[51] A. V. Churikov, A. V. Ivanishchev, I. A. Ivanishcheva, V. O. Sycheva, N. R. Khasanova, and E. V. Antipov, "Determination of lithium diffusion coefficient in $LiFePO_4$ electrode by galvanostatic and potentiostatic intermittent titration techniques," *Electrochimica Acta,* vol. 55, pp. 2939-2950, Mar 1 2010.
[52] J. Crank, *Free and moving boundary problems*: Clarendon Press Oxford, 1984.
[53] S. Jung, "Mathematical model of lithium-ion batteries with blended-electrode system," *Journal of Power Sources,* vol. 264, pp. 184-194, 2014.
[54] Y. Dai, L. Cai, and R. E. White, "Simulation and analysis of stress in a Li-ion battery with a blended $LiMn_2O_4$ and $LiNi_{0.8}Co_{0.15}Al_{0.05}O_2$ cathode," *Journal of power sources,* vol. 247, pp. 365-376, 2014.
[55] D. E. Stephenson, E. M. Hartman, J. N. Harb, and D. R. Wheeler, "Modeling of particle-particle interactions in porous cathodes for lithium-ion batteries," *Journal of the Electrochemical Society,* vol. 154, pp. A1146-A1155, 2007.
[56] S. Lee, J. Kim, J. Lee, and B. Cho, "State-of-charge and capacity estimation of lithium-ion battery using a new open-circuit voltage versus state-of-charge," *Journal of power sources,* vol. 185, pp. 1367-1373, 2008.
[57] S. Rodrigues, N. Munichandraiah, and A. Shukla, "AC impedance and state-of-charge analysis of a sealed lithium-ion rechargeable battery," *Journal of Solid State Electrochemistry,* vol. 3, pp. 397-405, 1999.
[58] J. F. Herbst, G. P. Meisner, and M. W. Verbrugge, "System and method to determine the state of charge of a battery using magnetostriction to detect magnetic response of battery material," ed: Google Patents, 2009.
[59] F. Sun, X. Hu, Y. Zou, and S. Li, "Adaptive unscented Kalman filtering for state of charge estimation of a lithium-ion battery for electric vehicles," *Energy,* vol. 36, pp. 3531-3540, 2011.
[60] I.-S. Kim, "Nonlinear state of charge estimator for hybrid electric vehicle battery," *Power Electronics, IEEE Transactions on,* vol. 23, pp. 2027-2034, 2008.
[61] M. Xiao and S.-Y. Choe, "Theoretical and experimental analysis of heat generations of a pouch type $LiMn_2O_4$/carbon high power Li-polymer battery," *Journal of Power Sources,* vol. 241, pp. 46-55, 2013.